



HAL
open science

Heat storage of PCM inside a transparent building brick : Experimental study and LBM simulation on GPU

Wei Gong

► To cite this version:

Wei Gong. Heat storage of PCM inside a transparent building brick : Experimental study and LBM simulation on GPU. Thermics [physics.class-ph]. INSA de Lyon, 2014. English. NNT : 2014ISAL0063 . tel-01149552

HAL Id: tel-01149552

<https://theses.hal.science/tel-01149552>

Submitted on 7 May 2015

HAL is a multi-disciplinary open access archive for the deposit and dissemination of scientific research documents, whether they are published or not. The documents may come from teaching and research institutions in France or abroad, or from public or private research centers.

L'archive ouverte pluridisciplinaire **HAL**, est destinée au dépôt et à la diffusion de documents scientifiques de niveau recherche, publiés ou non, émanant des établissements d'enseignement et de recherche français ou étrangers, des laboratoires publics ou privés.

N° d'ordre _____
Année 2014

Thèse

Heat storage of PCM inside a transparent building brick: experimental study and LBM simulation on GPU

Présentée devant

L'institut national des sciences appliquées de Lyon

Pour obtenir

Le grade de docteur

Formation doctorale

Energétique

École doctorale

École doctorale MEGA (Mécanique, Energétique, Génie Civil,
Acoustique)

Par

Wei GONG

Soutenue le 25 Juin 2014 devant la Commission d'examen

Jury MM.

G. FRAISSE	Professeur des universités (Université de Savoie)	Rapporteur
H. NAJI	Professeur des universités (Université d'Artois)	Rapporteur
K. JOHANNES	Maître de Conférences (UCBL Lyon 1)	
F. KUZNIK	Maître de Conférences, HDR (INSA de Lyon)	
J. VIRGONE	Professeur des universités (INSA de Lyon)	
P. H. BIWOLE	Maître de Conférences (Université de Nice Sophia-Antipolis)	

Laboratoire de recherche : Le Centre d'Energétique et de Thermique de Lyon (CETHIL UMR5008)

This page is left blank

INSA Direction de la Recherche - Ecoles Doctorales - Quinquennal 2011-2015

SIGLE	ECOLE DOCTORALE	NOM ET COORDONNEES DU RESPONSABLE
CHIMIE	CHIMIE DE LYON http://www.edchimie-lyon.fr Sec : Renée EL MELHEM Bat Blaise Pascal 3 ^e étage 04 72 43 80 46 Insa : R. GOURDON	M. Jean Marc LANCELIN Université de Lyon – Collège Doctoral Bât ESCPE 43 bd du 11 novembre 1918 69622 VILLEURBANNE Cedex Tél : 04.72.43 13 95 directeur@edchimie-lyon.fr
E.E.A.	ELECTRONIQUE, ELECTROTECHNIQUE, AUTOMATIQUE http://edeea.ec-lyon.fr Sec : M.C. HAVGOUDOUKIAN eea@ec-lyon.fr	M. Gérard SCORLETTI Ecole Centrale de Lyon 36 avenue Guy de Collongue 69134 ECULLY Tél : 04.72.18 60.97 Fax : 04 78 43 37 17 Gerard.scorletti@ec-lyon.fr
E2M2	EVOLUTION, ECOSYSTEME, MICROBIOLOGIE, MODELISATION http://e2m2.universite-lyon.fr Sec : Safia AIT CHALAL Bat Darwin - UCB Lyon 1 04.72.43.28.91 Insa : H. CHARLES	Mme Gudrun BORNETTE CNRS UMR 5023 LEHNA Université Claude Bernard Lyon 1 Bât Forel 43 bd du 11 novembre 1918 69622 VILLEURBANNE Cédex Tél : 06.07.53.89.13 e2m2@univ-lyon1.fr
EDISS	INTERDISCIPLINAIRE SCIENCES-SANTE http://www.ediss-lyon.fr Sec : Safia AIT CHALAL Hôpital Louis Pradel - Bron 04 72 68 49 09 Insa : M. LAGARDE Safia.ait-chalal@univ-lyon1.fr	Mme Emmanuelle CANET-SOULAS INSERM U1060, CarMeN lab, Univ. Lyon 1 Bâtiment IMBL 11 avenue Jean Capelle INSA de Lyon 696621 Villeurbanne Tél : 04.72.68.49.09 Fax :04 72 68 49 16 Emmanuelle.canet@univ-lyon1.fr
INFOMATHS	INFORMATIQUE ET MATHEMATIQUES http://infomaths.univ-lyon1.fr Sec :Renée EL MELHEM Bat Blaise Pascal 3 ^e étage infomaths@univ-lyon1.fr	Mme Sylvie CALABRETTO LIRIS – INSA de Lyon Bat Blaise Pascal 7 avenue Jean Capelle 69622 VILLEURBANNE Cedex Tél : 04.72. 43. 80. 46 Fax 04 72 43 16 87 Sylvie.calabretto@insa-lyon.fr
Matériaux	MATERIAUX DE LYON http://ed34.universite-lyon.fr Sec : M. LABOUNE PM : 71.70 –Fax : 87.12 Bat. Saint Exupéry Ed.materiaux@insa-lyon.fr	M. Jean-Yves BUFFIERE INSA de Lyon MATEIS Bâtiment Saint Exupéry 7 avenue Jean Capelle 69621 VILLEURBANNE Cedex Tél : 04.72.43 83 18 Fax 04 72 43 85 28 Jean-yves.buffiere@insa-lyon.fr
MEGA	MECANIQUE, ENERGETIQUE, GENIE CIVIL, ACOUSTIQUE http://mega.universite-lyon.fr Sec : M. LABOUNE PM : 71.70 –Fax : 87.12 Bat. Saint Exupéry mega@insa-lyon.fr	M. Philippe BOISSE INSA de Lyon Laboratoire LAMCOS Bâtiment Jacquard 25 bis avenue Jean Capelle 69621 VILLEURBANNE Cedex Tél :04.72 .43.71.70 Fax : 04 72 43 72 37 Philippe.boisse@insa-lyon.fr
ScSo	ScSo* http://recherche.univ-lyon2.fr/scso/ Sec : Viviane POLSINELLI Brigitte DUBOIS Insa : J.Y. TOUSSAINT	Mme Isabelle VON BUELTZINGLOEWEN Université Lyon 2 86 rue Pasteur 69365 LYON Cedex 07 Tél : 04.78.77.23.86 Fax : 04.37.28.04.48 viviane.polsinelli@univ-lyon2.fr

*ScSo : Histoire, Géographie, Aménagement, Urbanisme, Archéologie, Science politique, Sociologie, Anthropologie

This page is left blank

Everybody is a genius. But if you judge a fish by its ability to climb a tree, it will live its whole life believing that it is stupid.

ALBERT EINSTEIN

This page is left blank

Résumé

A présent, les bâtiments résidentiels et commerciaux sont en phase de devenir le secteur le plus consommateur d'énergie dans de nombreux pays, comme par exemple en France. Diverses recherches ont été menées de manière à réduire la consommation énergétiques des bâtiments et augmenter leur confort thermique. Parmi tous les différentes approches, la technologie du stockage de chaleur latent se distingue par une très bonne capacité à stocker la chaleur afin de réduire les écarts entre la disponibilité et la demande d'énergie.

Dans le cadre de l'un de nos projets, nous avons l'intention d'intégrer au design des murs des bâtiments un type de brique transparente remplie de matériaux à changement de phase (MCP). Les MCP à l'intérieur de la brique sont soumis à des changements de phase liquide-solide. Cette thèse s'attaque à la problématique du processus de fusion au sein de la brique.

Au cours de cette thèse, une méthode expérimentale non-intrusive a été développée afin d'améliorer les techniques expérimentales existantes. La vélocimétrie des images des particules (VIP) et la fluorescence induite par laser (FIL) ont été couplées pour étudier la convection naturelle et la distribution de la température. Puisqu'aucun thermocouple n'a été inséré au sein de la brique, le processus de la fusion a été considéré sans perturbation. Les résultats montrent que cette conception expérimentale a un avenir prometteur, même si elle reste à améliorer. Par la suite, nous présentons deux simulations numériques. Ces simulations se fondent sur la méthode de Boltzmann sur réseau à temps de relaxation multiple (LBM MRT), employée pour résoudre le champ de vitesse, et sur la méthode de différences finies, pour obtenir la distribution de la température. La méthode d'enthalpie a quant à elle été utilisée pour simuler le changement de phase. Les simulations en deux dimensions et trois dimensions ont toutes deux été réalisées avec succès. Point important, ces simulations numériques ont été développées en langage C pour tourner spécifiquement sur un processeur graphique (GPU), afin d'augmenter l'efficacité de la simulation en profitant de la capacité de calcul d'un GPU. Les résultats des simulations concordent bien avec les résultats de nos expériences et avec les résultats analytiques publiés.

Mots-clefs : changement de phase, fusion, convection naturelle, détermination de l'interface des phases, méthode enthalpique, matériaux à changement de phase (MCP), stockage de chaleur latent, méthode Boltzmann sur réseau, calculs avec haute performance, processeur graphique (GPU), économie d'énergie dans les bâtiments.

This page is left blank

Abstract

The domestic and commercial buildings are currently becoming the major sector that consumes the biggest share of the energy in many countries, for example in France. Various researches have been carried out in order to reduce the energy consumption and increase the thermal comfort of builds. Among all the possible approaches, the latent heat storage technology distinguishes itself because of its excellent heat storage ability which can be used to efficiently reduce the discrepancy between the energy consumption and supply.

In one of our project, we intend to integrate a type of transparent brick filled with phase change material (PCM) into the buildings' wall design. The PCM inside the brick undergoes the solid-liquid phase change. This dissertation addresses the important issues of the melting process inside the brick.

In this dissertation, a non-intrusive experimental method was proposed to improve the existing experiment technique. The particle image velocimetry (PIV) and the laser-induced fluorescence (LIF) were coupled to investigate the natural convection and the temperature distribution. Because there was no thermocouple installed inside the brick, the melting process was thus considered to be less impacted. The results showed that this experimental design has a promising future, yet still needs to be improved.

Two sets of efficient numerical simulations were also presented in this dissertation. The simulations were based on the thermal lattice Boltzmann method (TLBM), where the natural convection got solved by the LBM and the temperature equation was solved by the finite difference scheme. The enthalpy method was employed to simulate the phase change. Both the 2-dimensional and 3-dimensional configurations were successfully simulated. Moreover, the simulation programs were specifically developed - using the C language - to be run on the graphic processing unit (GPU), in order to increase the simulation efficiency. The simulation results demonstrated a good agreement with our experimental results and the published analytical results.

Keywords : phase change, melting, natural convection, phase interface determination, enthalpy method, phase change material (PCM), latent heat storage, lattice Boltzmann method, high performance computing, graphics processing unit (GPU), building energy saving

This page is left blank

Nomenclature

Symbol	Description	Unit/definition
General symbols		
e_α	LB velocity	
\mathbf{u}	macroscopic velocity	m/s
C_p	specific heat	J/(kg · °C)
k	conductivity	W/(m · °C)
l	liquid fraction	%
t	physical time	s
T	temperature	°C
H	height of the PCM container	
L	width of the PCM container or latent heat content	
LX, LY, LZ	the lattice dimension of calculation domain	
f_α	distribution function	
f_α^{eq}	Maxwell distribution function	
ω_α	weight coefficient of Maxwell distribution	
Greek letters		
α	thermal diffusivity	m ² /s
δx	discretized space	
δt	discretized time	
ν	viscosity	m ² /s
β	thermal expansion coefficient	K ⁻¹
λ	latent heat	J/kg
ρ	density	kg/m ³
ξ	molecule velocity	
τ	relaxation time of LBGK or dimensionless time (FoSte)	

Dimensionless numbers

Fo	Fourier number	$\frac{\alpha t}{H^2}$
Nu	Nusselt number	$\frac{hH}{k}$
Pr	Prandtl number	$\frac{\nu}{\alpha}$
Ra	Rayleigh number	$\frac{g\beta\Delta TH^3}{\nu\alpha}$
Ste	Stefan number	$\frac{c_p\Delta T}{L_h}$

Superscript and Subscript

*	dimensionless value
<i>LB</i>	lattice values
<i>x, y, z</i>	coordinates on x, y, z axes
<i>α</i>	index of discrete value in LBM
<i>w</i>	west wall
<i>e</i>	east wall
<i>s</i>	south wall or solid phase
<i>n</i>	north wall
<i>f</i>	front wall or melting
<i>b</i>	back wall
<i>l</i>	liquid phase
<i>init</i>	initial condition

List of Figures

1.1	Percentages of different energy types in the total energy consumed in 2012	5
1.2	Classification of energy storage [4]	7
1.3	The general classification of PCMs	13
1.4	Typical DSC measurement output curves [11]	16
1.5	Time lag ϕ and decrement factor f of the indoor temperature as against the outdoor temperature [12]	16
1.6	The indoor and outdoor temperature evolutions [13]	17
1.7	The heat capacities of some building materials before and after the incorporation of PCMs [17]	19
1.8	SEM image of PCM micro-capsules in gypsum plaster [19]	20
1.9	Shape-stabilized PCM	21
1.10	Direct mixing and laminated PCM board [30]	22
1.11	Schematic of electric floor heating system with shape-stabilized PCM plates [35]	23
1.12	Installation of ceiling panels in building interior as suspended ceiling [36].	24
1.13	Trombe wall	26
1.14	Crystallisation process of S27 (upper part of the window). The material solidifies in the shape of crystal needles which keep growing until they draw through the whole container (picture sequence up to down) [31].	27
1.15	Four-region model for scale analysis [54]	32
1.16	Transparent brick (filled with PCM)	37
2.1	Diagram of a modern PIV system	47
2.2	Polar distribution of the scattered light intensity of different particles sizes [92]	49
2.3	Single frame technologies [93]	51
2.4	Multiple frame technologies [93]	52

2.5	Interrogation area in the first frame and searching areas in the second frame	53
2.6	Diagram of combined LIF and PIV test	54
2.7	The spectrum characteristics of Rhodamine B [89]	56
2.8	Experimental equipments	58
2.9	The mixture of n-octadecane and Rhodamine B (in liquid phase)	60
2.10	Transparent brick (with n-octadecane inside)	61
2.11	The design dimensions of the brick (unit: mm)	61
2.12	The two vertical sides are replaced by two heat exchangers	62
2.13	The design dimensions of the aluminium plate (unit: mm)	62
2.14	Pass percentage of different wavelength of the filter	63
2.15	The lenses to expand the laser beam to a sheet	64
2.16	Boundary and initial conditions. $T_w = T_{init} = 27.8^\circ\text{C}$, $T_e = 35^\circ\text{C}$, under this configuration, the $Ra = 2.48 \times 10^8$	66
2.17	The four melting stages of the solid-liquid interface	67
2.18	The interface evolution at different heights	68
2.19	Melting velocity of the interface at different y	69
2.20	The melting interface.	69
2.21	Typical vector field	70
2.22	Contour of velocity at moment 1	71
2.23	Contour of velocity at moment 2	72
2.24	Average \overline{Nu} numbers of the hot wall	73
2.25	The contours of temperature at three different moment	74
3.1	Tow-body collision diagram	84
3.2	D2Q9 scheme	90
3.3	Experiment enclosure	93
3.4	CUDA Block of threads and grid of blocks	97
3.5	Memory structure of GPU	98
3.6	CUDA hardware	99
3.7	The propagation and temperature scheme	101
3.8	Data structure	101
3.9	Experiment configuration and diagram	103
3.10	Grid dependence	104
3.11	The evolution of melting interface with the dimensionless time: comparison between simulation and experiment. $Ra = 2.48 \times 10^8$, $Pr = 50$, $Ste = 0.072$	104
3.12	Average Nu number on the left vertical isothermal wall (T_h) during melting of n-octadecane. $Ra = 2.48 \times 10^8$, $Pr = 50$, $Ste = 0.072$	105
3.13	Temperature contours at four different τ . $Ra = 2.48 \times 10^8$, $Pr = 50$, $Ste = 0.072$	106

3.14	Streamlines at four different τ . $Ra = 2.48 \times 10^8$, $Pr = 50$, $Ste = 0.072$	107
3.15	Performance of implementation	108
4.1	The D3Q19 stencil	112
4.2	The algorithm for simulation	116
4.3	Halo temperature arrangement	118
4.4	Calculation domain	119
4.5	The dispositions of the cross-sections, lines and their indexes	119
4.6	The relative errors of Nusselt number. (when time $t = 1500s$, compared with the mean value and the Rayleigh number $Ra = 10^7$)	120
4.7	Isosurfaces of the velocity components when $Ra = 2.48 \times 10^8$ and $\tau = 0.00312$ (5000s)	122
4.8	Streamlines on the cross-sections: S1, S2 and S3. When $Ra = 2.48 \times 10^8$ and $\tau = 0.00312$ (5000s)	123
4.9	The velocity components on the lines L-S1-1, L-S1-2 and L-S1-3. When $Ra = 2.48 \times 10^8$ and $\tau = 0.00312$ (5000s)	125
4.10	The velocity components on the lines L-S2-1, L-S2-2 and L-S2-3. When $Ra = 2.48 \times 10^8$ and $\tau = 0.00312$ (5000s)	126
4.11	The velocity components on the lines L-S3-1, L-S3-2 and L-S3-3. When $Ra = 2.48 \times 10^8$ and $\tau = 0.00312$ (5000s)	127
4.12	The velocity components on the lines L-S4-1, L-S4-2 and L-S4-3. When $Ra = 2.48 \times 10^8$ and $\tau = 0.00312$ (5000s)	128
4.13	The velocity components on the line L5. When $Ra = 2.48 \times 10^8$ and $\tau = 0.00312$ (5000s)	129
4.14	The temperature isosurfaces in the 3-dimensional simulation. $Ra = 2.48 \times 10^8$ and $\tau = 0.00312$ (5000s)	130
4.15	The contours of temperature on the cross-sections: S1, S2 and S3. When $Ra = 2.48 \times 10^8$ and $\tau = 0.00312$ (5000s)	131
4.16	The Nu number temporal evolution. The $Ra = 2.48 \times 10^8$ and $\tau = 0.00312$ (5000s)	132
4.17	The solid-liquid interface at instant $\tau = 0.00312$ (5000s): 2-dimensional and 3-dimensional simulations. ($Ra = 2.48 \times 10^8$)	132
4.18	The melting process when $Ra = 2.48 \times 10^8$	133
4.19	The average Nu number of the heating wall at different Ra numbers	134
4.20	The average Nu number of the heat wall and the analytical results from [54] when $Ra = 10^6$	134
4.21	The average Nu number of the heat wall and the analytical results from [54] when $Ra = 10^7$	135
4.22	The average Nu number of the heat wall and the analytical results from [54] when $Ra = 10^8$	135

4.23	The melting process when $Ra = 10^6$	137
4.24	The melting process when $Ra = 10^7$	138
4.25	The melting process when $Ra = 10^8$	139

List of Tables

1.1	Major regions' energy consumption in the year 2012 (Million tonne of oil equivalent)	4
1.2	The energy consumed by different domains (France, 2008) [3]	5
1.3	A selection of PCMs	15
2.1	Typical tracer particles for liquid flows [92]	50
2.2	Possible error sources for LIF (extracted from [97,98])	57
2.3	Thermophysical properties of n-octadecane [69]	58
2.4	The specifications of Polyamide seeding particles	59
2.5	Specifications of Refrigerated Bath	60
2.6	Camera (model: Imager intense) specifications	64
2.7	laser specifications	64
2.8	Configuration for experiment setup under the laser light wavelength 532 nm and a desired pixel displacement of 16 pixels	66
2.9	Reference points for the evolution of interface (dimensionless form)	68
3.1	Thermophysical properties of n-octadecane used for simulation [69]	93
3.2	Specifications of the Tesla C2050	99
3.3	Experimental parameters	103
4.1	Specifications of Tesla C2075	115
4.2	Simulation cases	119
4.3	The values of Nusselt number at different mesh resolutions. When $Ra = 10^7, t = 1500s$	120
4.4	Band width of Nvidia Tesla C2075 GPU	140
4.5	Performance of simulation	140

Contents

Résumé (in french)	VII
Abstract	IX
List of figures	XVI
List of tables	XVII
Preface	1
Background	1
Organization of this thesis	2
1 General Introduction	3
1.1 Energy and climate	3
1.2 Energy storage	6
1.2.1 Classification and applications	7
1.2.1.1 Mechanical energy storage	7
1.2.1.2 Chemical energy storage	8
1.2.1.3 Biological storage	9
1.2.1.4 Magnetic storage	9
1.2.1.5 Thermal energy storage	10
1.3 Latent heat storage	11
1.3.1 Phase change materials	12
1.3.1.1 General requirements	12
1.3.1.2 Classification	13
1.3.1.3 Thermophysical properties	14
1.3.2 Application of LHS on buildings	15
1.3.2.1 PCM implantation	17
1.3.2.2 Different application scenarios	22
1.3.2.2.1 The active heat storage system	22
1.3.2.2.2 The passive heat storage system	24

1.3.2.3	Heat performance enhancement	28
1.3.3	Literature review on natural convection with phase change	30
1.3.3.1	Experimental and analytical study	30
1.3.3.2	Numerical study	34
1.3.3.2.1	Adaptive mesh	34
1.3.3.2.2	Fixed mesh	35
1.4	Proposition of this research	36
I	Experimental method	41
2	Experimental study	45
2.1	Introduction	45
2.2	Experimental design	46
2.2.1	Study of the natural convection flow: particle image velocimetry	46
2.2.1.1	Tracer particles	47
2.2.1.1.1	Particle density and size	48
2.2.1.1.2	Particles' seeding	49
2.2.1.2	Image recording	50
2.2.1.3	PIV processing procedures	50
2.2.1.3.1	Image preprocessing	51
2.2.1.3.2	PIV processing	52
2.2.1.3.3	Vectors post-processing	53
2.2.2	Study of the temperature distribution: laser-induced fluorescence	54
2.2.2.1	Theory of the LIF	54
2.2.2.2	Spectra characteristics	56
2.2.2.3	Error sources	57
2.3	Experimental setup	57
2.3.1	The PCM-Rhodamine mixture	58
2.3.2	Transparent brick and water pump heat exchanger	60
2.3.3	Heat flux meters and thermocouples	61
2.3.4	Image capture and analysis unit	63
2.3.4.1	Camera and filter	63
2.3.4.2	Laser	63
2.4	Experimental procedure	64
2.4.1	The LIF calibration	64
2.4.2	Experiment steps and configuration	65
2.5	Results	67
2.5.1	Melting process	67
2.5.2	Liquid-solid interface evolution	67

2.5.3	Velocity field	68
2.5.4	Heat transfer rate	73
2.5.5	Temperature contour	74
2.6	Conclusions and remarks	75
2.6.1	Conclusions	75
2.6.2	Remarks on the combination of the PIV and the LIF	76
II	Numerical method	77
3	Numerical simulation on 2D	81
3.1	Introduction	81
3.2	Lattice Boltzmann Method	82
3.2.1	Boltzmann equation	83
3.2.1.1	Collision invariant	86
3.2.1.2	Maxwell distribution	87
3.2.1.3	Boltzmann equation Bhatnagar-Gross-Krook (BGK) approximation	87
3.2.2	Lattice Boltzmann equation	88
3.2.2.1	LBGK	88
3.2.2.1.1	Discretization of time and space	88
3.2.2.1.2	Discretization of molecule velocity	89
3.2.2.2	LBE-MRT	90
3.3	Numerical modelling	92
3.3.1	Definition of the problem	92
3.3.2	Model construction	93
3.3.2.1	The governing equations	93
3.3.2.2	Energy equation	94
3.3.2.3	Problem solving	97
3.4	Nvidia GPU hardware and implementation	97
3.4.1	GPU with CUDA architecture	97
3.4.1.1	CUDA program pattern	97
3.4.1.2	Memory types	98
3.4.1.3	CUDA hardware	99
3.4.2	Implementation	100
3.4.2.1	Data and memory utilization	100
3.4.2.2	Boundary conditions and simulation procedure	101
3.5	Results and discussion	102
3.5.1	Model validation	102
3.5.1.1	Experiment configuration	102
3.5.1.2	Model validation	103
3.5.2	Simulation results	105

Preface

Background

WE can never emphasize more the crucial role played by energy in the sustainability of our human society nowadays than whenever before. This assertion attributes to two reasons. First, in the past decades, the biggest share of energy we used was from coal, natural gas and raw oil, known as fossil fuels. Notwithstanding until today we still count on them, the fact we must face is that these fossil fuels are going to an end. Second, the large utilization of traditional fossil energy has imposed huge impacts on our environment, such as notorious CO₂ emission as well as the other sulfides.

Consequently, more and more researchers around the world are engaging themselves in finding new ways to get clean renewable sustainable energy. Solar energy is undoubtedly one of the most attractive energy sources. It is available almost all the time, zero cost, no negative impacts on the environment. Basically, photoelectric and photothermal are two conversion methods to utilize solar energy. The main characteristic of solar energy is its time depending availability, which means only available in daytime and sunny hours. However, our needs for energy do not vary according to this. As a result, it needs an efficient heat storage way to collect the relatively abundant solar heat during the sunny daytime and use it later, for example, in the night.

Except for this significant application of heat storage technology from sustainable perspective, there exist plenty of other domains which also have something to do with heat storage technology in order to achieve their own purposes. Here illustrate two applications:

Electricity consumption varies between days and nights. The quotidian required electricity load for household changes based on the needs for maintaining the temperature inside a flat as well as cooking. This requirement exaggerates especially at those places with notable temperature fluc-

tuation between day and night, as well as at those with extreme hot or cold environment. By contract, during midnight the requirement for electricity becomes fable and the electricity price is also lower. The existence of this peak need for electricity asks for a better design of electricity generation plants and electrical distribution network, which absolutely will increase the cost of power plants. Besides, the end-users also need to decrease their expenses on electricity. Those two basic requirements invoke the latent thermal energy storage which is an excellent way to partially transfer peak-load to another time period. For example, if we just take the big cities around the world into account, this thermal energy storage implementation could shift 200 to 300 MW every ten years for each of them.

Another phenomenon arises recent years is the so-called cloud calculation in information domain. The fundamental infrastructure is located at lieu named *data centres* (most famous as Google, Facebook, Apple and Amazon). It has been announced that those data centres might be a huge black hole for energy especially for electricity. Beyond this, they all waste a great deal of energy in the form of waste heat mainly from the electronic devices. The heat storage technology can be used to store the waste heat then be took elsewhere and discharge this amount heat energy, such as heating up the flats.

Since the heat storage can be so versatile, there is no reason not to have a deeper understanding about it, such as its realization forms, material types, heat transfer peculiarities and sustainability *etc.*

Organization of this thesis

This thesis focuses on the latent heat storage, *i.e.* heat transfer process with solid-liquid phase change. In order to make this study self-contained, both experimental and numerical simulation are employed. Following a general introduction and bibliography study in chapter 1, chapter 2 discusses the experimental part, a new experimental design will be proposed; chapter 3 and chapter 4 depict the numerical simulation, the melting process was calculated by thermal LBM method in both two and three dimensions. The solver is designed to run on a graphic process unit (GPU) to gain higher efficiency. This thesis finishes with the general conclusion and outlook.

General Introduction

1.1 Energy and climate

The world's overall industrialization process and humans' increasing needs for better living conditions threaten the stability and reliability of the current energy structure. In addition to the conventional fossil fuels, known as coal, natural gas and crude oil, new energy sources have arisen, such as nuclear, biomass, wind or solar. What's more, those unconventional energy sources are becoming more and more significant in the consideration of their environment friendly traits and sustainability.

In 1999, the total amount of energy consumed all over the world was 1.09×10^{14} kWh (9.34×10^9 tonne of oil equivalent), of which different forms accounted for: petroleum 4.34×10^{13} kWh, natural gas 2.53×10^{13} kWh, coal 2.46×10^{13} kWh, nuclear 7.32×10^{12} kWh, other energy (including renewable energy, hydro, geothermal, solar energy and wind energy) 8.67×10^{12} kWh [1]. The world population in 1999 hit 6 billion, therefore the energy consumption per capita in 1999 was around 1.82×10^4 kWh (about 1.56 tonne of oil equivalent), As a comparison the energy for sustaining basic human body need is 1.4×10^4 kJ/year (about 3.33×10^{-4} tonne of oil equivalent).

In 2012, the world energy consumption was shown in table 1.1 [2]. The primary energy consumption reaches 12476.6 million tonne of oil equivalent, which is 33.6 % higher than that in 1999. At the same time, the renewable and hydro energy consumption rises 43.8 % from 1999 to 2012, that is to say faster than the total primary energy consumption growth rate. We can see from the Figure 1.1 that the major countries/regions in the world, the fossil fuels consistently account for more than 80 % of the total energy consumption, France being a slight exception with less than 55 %.

Table 1.1 – Major regions' energy consumption in the year 2012
(Million tonne of oil equivalent)

Regions	Type of energy source							
	Oil	Natural gas	Coal	Nuclear energy	Hydroelectricity	Renewable energy	Primary energy	Primary energy
France	80.9	42.5	11.4	96.3	13.2	5.4	245.4	245.4
Germany	111.5	75.2	79.2	22.5	4.8	26.0	311.7	311.7
The United Kingdom	68.5	78.3	39.1	15.9	1.2	8.4	203.6	203.6
China	483.7	143.8	1873.3	22.0	194.8	31.9	2735.2	2735.2
Japan	218.2	116.7	124.4	4.1	18.3	8.2	478.2	478.2
The United States	819.9	722.1	437.8	183.2	63.2	50.7	2208.8	2208.8
Europe Union	611.3	443.9	293.7	199.8	74.0	95.0	1673.4	1673.4
Total of the world	4130.5	3314.4	3730.1	560.4	831.1	237.4	12476.6	12476.6

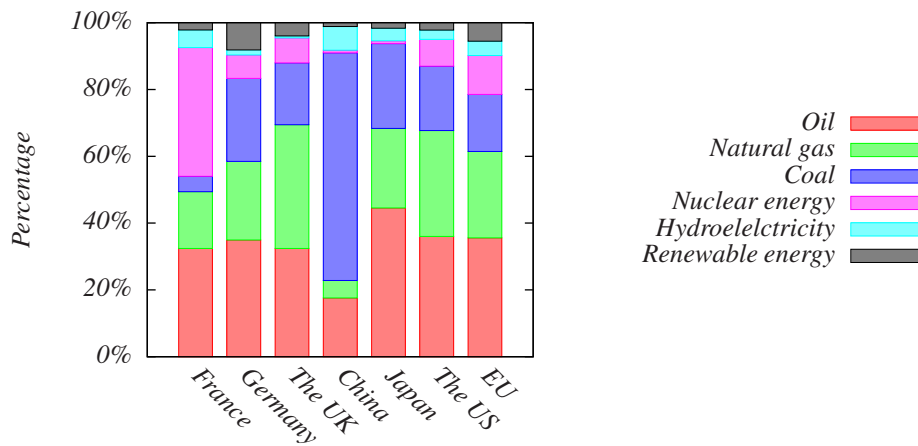


Figure 1.1 – Percentages of different energy types in the total energy consumed in 2012

The total energy is roughly consumed by three major sectors, domestic and commercial buildings, industries, and transportation. Since housings require more and more energy to satisfy people’s needs for thermal comfort, out of the the three means, domestic and commercial buildings are becoming one of the sector that consumes the most energy, especially in developed countries. For example, in 2008 the residential buildings consumed between 39.3% to 42.5% of the total energy consumed in France [3], and 34.17% in Unite States [1]. The detailed energy consumption shares in France are shown in table Table 1.2.

Table 1.2 – The energy consumed by different domains (France, 2008) [3]

Agriculture	Buildings	Industry (excluding metallurgy)	Metallurgy	Transportation	Others
2.9%	39.3%	16.6%	3.8%	28.0%	9.4%

As mentioned before, the traditional fossil fuels are still massively employed. Unfortunately causes severer environmental problems. The vast amount of carbon dioxide gas and other green house gasses released into the atmosphere, results in climate changing, unnatural heat waves and precipitations, sea level rising and the deterioration of ozone layer. What’s more, the fossil fuels may still last for a couple of decades, but this period

of time should not be taken for granted. Whether to preserve our planet or to insure a reliable energy supply, we must take some measures to solve this environmental and energy problem.

At present, the thermal energy storage technologies are widely proven as an effectively way to alleviate the dependency on convectional fossil fuels and as well as to increase the energy usage efficiency in the same time. In the next sections, we will give a detailed introduction about all the aspects of energy storage, focusing on thermal energy storage technologies, from the classification of different heat storage ways, phase change materials to their applications and so on.

1.2 Energy storage

The concept of energy storage has existed for long time, but the past recent years have seen an increasing attention being given to the subject. The principal purpose of energy storage is to enhance the energy utilizations' efficiency. It stores energy in one form or another at one time; so that the stored energy can be later withdrew for a particular need. As can be seen, this approach successfully separates the energy supply and the need. In reality, energy availability and demand rarely concur: solar energy is not available during the nights, wind energy is intermittent over the year. Besides, as the two examples mentioned above testified, it is in general more critical for renewable energy sources to decrease the discrepancy of availability and demand. The energy storage technologies thus are quite an essential topic in the research domain of the alternative energy.

Apart from the advantages aforementioned, energy storage has extra merits, such as [4]: reducing energy cost and consumption; reducing energy system initial and maintenance cost; reducing equipment size and increasing its operation flexibility; reducing green house gasses; and, last but not least, decreasing the usage of convectional fossil fuels.

The energy demand in either industrial or domestic sectors vary with time. The energy suppliers have then to meet this demand. Generally speaking, there are two ways to achieve this: either by devising a more flexible energy supply system which adjusts according to the energy demand, or by finding a method to absorb the peak demand. From the economic point of view, devising a more complex and adaptable system requires more investment and maintenance. Energy storage, on the contrary, requires less investment.

In addition to the potential applications in the energy supply-demand industry, energy storage also exhibits its versatility in other domains. For commercial and residential buildings, energy storage can be used as an alternative to air-conditioning, significantly reducing the electricity consumption and alleviating the imbalance between the need and demand.

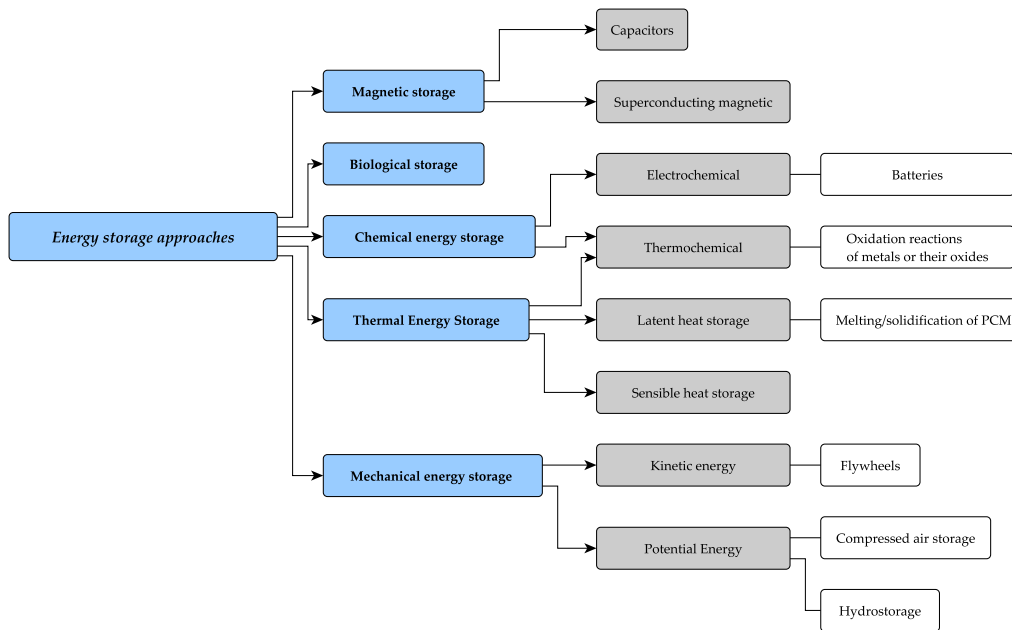


Figure 1.2 – Classification of energy storage [4]

At the same time, energy storage technologies also can help reducing the petroleum used for transportation as more and more cars and trucks will be driven by batteries in the future.

All in all, energy storage is a promising technology for solving our current problems regarding energy crisis, environmental deterioration. Its highly adaptable applications scenarios make it essential to upgrade the traditional fossil fuels utilization patterns; and as well to help developing highly efficient approaches to alternative energy sources. In next section, we summarize the classification and relevant applications of energy storage.

1.2.1 Classification and applications

The energy storage process is simply based on energy charging, distributing and discharging on the end-user side. Depending on different realization systems and mechanisms, the energy storage technologies spread themselves into several distinct categories. Figure 1.2 shows the classification of different energy storage approaches.

1.2.1.1 Mechanical energy storage

The fundamental principle is to store the energy in the form of mechanical energy. Generally it includes the potential energy and kinetic energy.

In some electricity generation plants, during the off-peak hours, the extra power can be used to pump up water to a high positioned reservoir. The electric energy is thus stored in the form of potential energy in the water. When there is a rush demand for electricity, the water is released and flows down through a turbine to lower position and accordingly generates electricity. This is a very simple application, but has been largely used in a good deal of cases. The drawbacks are: 1. that the power plants must be located where it is possible to pump up water; 2. that the energy storage has low energy conversion rate, causing a large amount of energy to dissipate during the conversion.

Another similar case is the compressed air storage technology. When compressed by a compressor, the air stores the energy with high pressure. Later, the compressed air can then release this part of energy by driving a gas turbine to generate electricity. To find the ideal containers to accommodate the compressed air is quite a critical work. Currently, the possible choices are natural or man-made caves under ground.

One of the cases that uses kinetic energy storage technology is the usage of flywheels, which store the energy in rotating flywheels made of either metals or other materials. The energy stored in flywheels is quantitatively small. For instance 1 Wh of equivalent energy is equal to the energy possessed by a flywheel with mass of 1.8 kg at rotating velocity of 600 rpm. The flywheels can be used to store energy for temporary use. The automobiles, especially those in public transportation encounter a plenty of acceleration and deceleration when close to each stop. Normally, the brakes are widely used to decelerate. In this situation, a large amount of energy is wasted in the form of heat. However, flywheel can be used to store the energy during the deceleration process, and then release the energy when the engines are fired for acceleration. This substitution can economize at least 50% of energy.

1.2.1.2 Chemical energy storage

The energy stored by chemical energy storage is obtained through reversible chemical reactions. The reactions used to store energy can be classified as thermochemical reactions and electrochemical reactions.

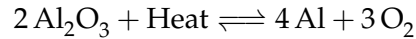
The thermochemical reactions which are suitable for energy storage are in general endothermic reactions. Those reactions must produce some types of output chemical products which are relatively physically stable and easily separable as well. This concept is shown as:



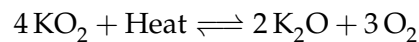
When one reaction starts from left to right, it absorbs thermal energy in and produces C and D. C and D should have relatively stable forms and

could be easily separated. Thermal energy is stored after the reaction finished. When the reaction starts in the opposite direction, the thermal energy stored will therefore be released, which accomplishes the whole energy storage cycle.

Oxidation reactions of metals or their oxides such as aluminum and potassium are good candidates [5]. Their reactions are expressed as:



and



All of them can store massive amount of energy of the magnitude of MJ/kg. The operation temperature is also relatively high, between 300 °C to 800 °C.

The applications of electrochemical reactions are well-known as batteries. The typical value of energy conversion rate of a battery is between 70-80%, which is higher than the one of mechanical energy conversion. Batteries are widely used in automotive industry, and have the potential to be implemented into the renewable energy system such as wind or photovoltaic electricity generation. Nowadays, the major problems about batteries development remain the high cost, relative short life cycles and low unit energy capacity and energy density of the batteries.

1.2.1.3 Biological storage

The energy also can be stored in a biological system. Until now, there are somewhat scarce results published about biological energy storage [6]. Its low conversion rate is most probably the main hindrance.

1.2.1.4 Magnetic storage

The magnetic storage technology is based on the superconducting phenomenon [7]. Metals which have superconducting ability can have a large electricity current circulating within them without big dissipation. This is a very promising way to store electricity and transport it, since a large amount of electricity power is lost during the long-distance transportation. The key to trigger the superconducting phenomenon is to maintain a temperature close to absolute zero, which requires complex system and maintenance. As a result, the high cost to implement large scale magnetic storage remains the main problem to be solved.

1.2.1.5 Thermal energy storage

In most situations, the energy is consumed in the form of energy flux, namely energy current. Thermal energy is the ultimate energy form that is widely used. Even for the electricity generation, heat is also used to generate high temperature and high pressure stream to drive the generator to produce electricity. As a result, storing thermal energy is a highly efficient and fundamental way to store energy. Thermal energy can be stored either by rising the substance's temperature or by changing the substances' phase. According to the two different ways, thermal energy storage includes sensible heat storage (SHS) and latent heat storage (LHS). In addition, some researchers judge thermochemical energy storage as the third way for thermal energy storage. However in this thesis, thermochemical energy storage is categorized into the chemical energy storage.

Sensible heat storage

Theoretically, the sensible heat storage is realized by increasing the materials' temperature. Its storage ability depends on the materials' specific heat capacities and temperature difference, see Eq. (1.1)

$$Q_{\text{sen}} = \int_{T_0}^{T_1} m C_p dT \quad (1.1)$$

Where the T_0, T_1 refer to the initial temperature and final temperature respectively. For same amount of mass (m) and same temperature difference ($\Delta T = T_1 - T_0$), the whole quantity of heat stored is influenced only by specific heat C_p . Normally, the specific heat capacity of different materials is quite small, for example, the C_p of water is $4.2 \text{ kJ/kg} \cdot \text{K}$ and rock's is $1.0 \text{ kJ/kg} \cdot \text{K}$, paraffin RT58/RT60's is even smaller, $0.9 \text{ kJ/kg} \cdot \text{K}$.

Rocks/sands and water are the most widely chosen storage media. Based on different operation temperature ranges, the heat stored has different exergy quality, so the sensible heat storage has different applications [8]. For high temperature storage, sensible heat storage can be used in many industrial activities, such as waste heat recovery in most power plants and metallurgical factories. Low temperature heat storage has more applications in domestic life, for example, solar heating, building heating and cooling, and air-conditioning. The advantage of sensible heat storage is its relative low cost and easy implementation. Besides in most cases, the materials used to store sensible heat have high heat conductivity. While its disadvantage is also prominent. Due to the low specific heat capacity of the materials, the sensible heat storage systems are always giant in size, as they encounter a large temperature fluctuation, and needs a better duration design.

Latent heat storage

As contrast, latent heat storage is based on the phase change heat. When phase change materials undergo melting, they absorb heat as fusion heat; when phase change materials become solid, they release the latent heat. The first advantage of latent heat storage is that, during phase change, the operation temperature has a narrow fluctuation, and sometimes the operation temperature is even fixed; another advantage is that latent heat of fusion of phase change materials is noticeable large. As a result, the latent heat storage system achieves more compact sizes than its sensible heat storage counterpart. However, its significant weakness is that most phase change materials have lower heat conductivity. As a result, extra heat transfer enhancement approaches need to be considered in order to get better heat performance. The detailed introduction and literature review about latent heat storage will appear in the following section (Sec. 1.3).

1.3 Latent heat storage

When taking latent heat storage into account, all the drawbacks of sensible heat storage convert to the advantages of latent heat storage. Phase change consists of solid-liquid phase change, liquid-gas phase change and gas-solid phase change, called evaporation or condensation, solidification or melting, sublimation or deposition respectively. Because of the existence of gas phase, gas-liquid phase change and gas-solid phase change undergo a considerable volume expansion, so they are not ideal ways for latent heat storage. As a result, when we talk about latent heat storage in this thesis, we are solely dealing with solidification and melting processes.

The materials used to store heat and at the same time encountering solidification and melting are called phase change materials (PCMs). From temperature T_0 lower than its melting temperature T_f to final temperature $T_1 > T_f$, the heat stored by PCMs can be formulated as follow:

$$Q_{\text{lat}} = Q_{\text{sen,l}} + m\lambda + Q_{\text{sen,s}} \quad (1.2)$$

where the subindex l, s signify liquid phase and solid phase; Q_{sen} and Q_{lat} are sensible heat and latent heat, respectively. λ is latent heat of fusion.

As we can see from the equation aforementioned, contrasted with sensible heat storage, the latent heat of PCM is generally very large, for instance, the latent heat of fusion of a typical PCM n-octadecane ($\text{C}_{18}\text{H}_{38}$) is 125 kJ/kg. To store Q kJ heat under temperature gradient $\Delta T = 10^\circ\text{C}$, for n-octadecane, the mass needed without melting is about 11 times more than in the process with melting. Thus, in order to store the same quantity of heat, latent heat storage requires lesser amount of material. Furthermore, many kinds of PCM's have a relatively negligible fusion temperature

fluctuation range, sometimes even isothermal. It means that heat transfer during the solidification and melting can progress under a high and stable temperature gradient, and consequently, maintains a high heat transfer rate.

In the next sections, we will talk about the main aspects of solid-liquid latent heat storage.

1.3.1 Phase change materials

1.3.1.1 General requirements

Phase change materials (PCMs) are considered as critical element in order to fulfil the latent heat storage process. The phase change materials' properties required for thermal energy storage vary according to application cases. However, there are a number of basic criteria that can be taken into consideration in order to select suitable substances as PCMs. Those criteria include thermal, physical, kinetic and chemical properties. One profound introduction about PCMs can be found in A. Abhat's article [9].

From the aspect of thermal properties, the candidates should have:

- ⇒ high heat conductivity, which ensures high thermal performance;
- ⇒ reasonable phase change temperature, which is compatible with the specific application;
- ⇒ high heat of fusion, which reduces the PCMs' volume when storing a given amount of heat.

From the viewpoint of kinetic properties, they should have excellent nucleation ability and rate. This is a very critical index to judge the PCM's supercooling effect during solidification. When the ambient temperature is lower than the fusion temperature, the PCM in the form of liquid will encounter solidification. The initial stage of solidification is attributed to nucleation. The nucleation generates small nucleus. Then the liquid PCM in the vicinity of nucleus starts to aggregate around those nucleus, and finally, liquid becomes solid. However, PCMs that possess weak nucleation ability would maintain liquid phase even when the ambient temperature is lower than the fusion temperature. This phenomenon is called supercooling which is not welcoming when selecting the suitable PCMs.

Furthermore, the favourable physical properties that the PCM candidates should have are [10]:

- ⇒ nice phase equilibrium;
- ⇒ high density;
- ⇒ feeble volume change;
- ⇒ low vapour pressure;

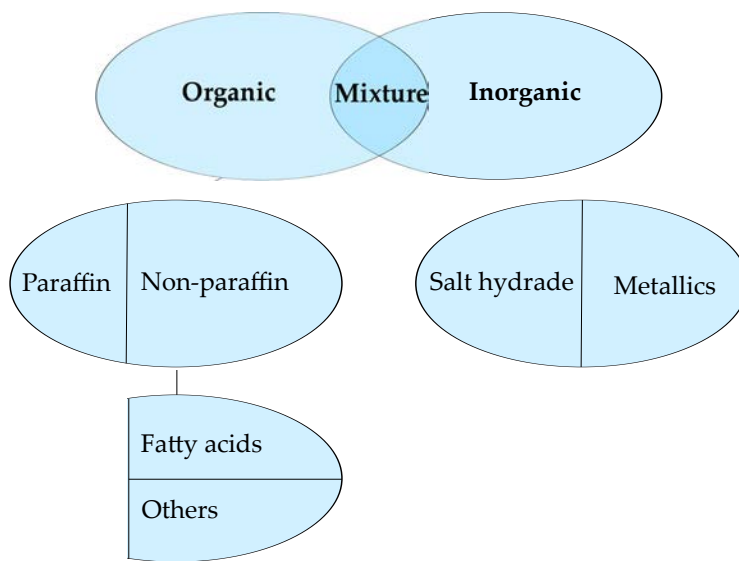


Figure 1.3 – The general classification of PCMs

and the favourable chemical properties are [10]:

- ⇒ long-term chemical stability;
- ⇒ absence of decay on the container materials;
- ⇒ absence of toxicity to humans;
- ⇒ not being combustible

Among those criteria, some need to be strictly observed, *e.g.* the chemical properties; and some are not extremely critical but can give better thermal performance if satisfied, *e.g.* thermophysical properties.

The next subsection will depict the classification of PCMs.

1.3.1.2 Classification

Basically, the PCMs can be categorized in three major groups [10]: organic, inorganic and their mixtures (Figure 1.3).

In the category of organic PCMs, they can be subdivided into paraffins and non-paraffins, the latter consisting of fatty acids and other non-paraffins. Paraffins include mainly n-alkane, as well as some p-alkane, naphthalene and aromatic. Among them the mostly utilized type as PCMs is n-alkanes. Paraffins as PCM usually have chemically stable properties in application temperature range, and are neither toxic nor corrosive; paraffins also have considerably large latent heat of fusion, which can reduce the geometric size of the containers. In addition, the melting process of paraffins is congruent, has a fast nucleation rate and a very rare supercooling phenomenon. The shortcomings are also prominent. The paraffins have

relatively small heat conductivities, and smaller latent heat of fusion than inorganic PCMs; they can also decay the plastic used as containers; and are somewhat inflammable. Except for paraffins in the group of organic, the fatty acids are very common non-paraffin PCMs. The fatty acids in general have similar properties to paraffins but have a relatively higher latent heat of fusion; they also cost more than paraffins and possess noticeable corrosive ability.

The group of inorganic PCMs is composed of salt hydrates for the most part. They are the combination of salts with water molecules. Salt hydrates have high latent heat of fusion, higher heat conductivity than paraffins, are less corrosive on plastic; and usually can be bought for a reasonably low price. The drawbacks of salt hydrates is that they have supercooling phenomena at the beginning of solidification, which can reduce the heat performance; in addition, their melting process is not congruent, which can prevent salt hydrates from solidification-fusion recycling.

Another type of inorganic PCMs are pure metallics with low fusion temperature, for instance gallium (Ga). The metallics have very distinct properties from the other PCMs. They have very high latent heat of fusion per unit mass and high density, as well as high heat conductivity and low specific heat capacity. Those properties give metallics different phase change phenomena which require more intense studies.

The third category, in a more strictly point of view, is derived from the other two categories. In this third group, the PCMs are mixtures of different organic and/or inorganic substances. One special case occurs when this mixture has a relatively unique lower melting temperature than any of their ingredients. Consequently, this type of mixtures is called eutectic system.

Some typical PCMs from the three different categories were shown in [Table 1.3](#).

1.3.1.3 Thermophysical properties

As in the previous section, the thermophysical properties of PCMs include heat conductivity, latent heat of fusion, specific heat capacity and temperature of fusion. In order to perform either experiments or numerical simulations of phase change, it is of great importance to precisely obtain the thermophysical properties. However, the relevant properties recorded in the published references inevitably include some imprecisions and from time to time even errors. Consequently, it is recommended to perform test to obtain the thermophysical properties before the analysis a PCM phase change system.

There is a couple of different methods that could be used to carry out this measurement. For instance, differential thermal analysis (DTA) and

Table 1.3 – A selection of PCMs

Inorganic	Organic	Eutectic
Water-ice	Paraffin RT60/RT58	Lauric-palmitic acid
MgCl ₂ · 4 H ₂ O	n-Octadecane	LiF–CaF ₂ (80.5:19.5)
MgCl ₂ · 6 H ₂ O	Acetic acid	ZnCl ₂ –KCL (0.319:0.681)
Mg(NO ₃) ₂ · 4 H ₂ O	Capric acid	Bi–Cd–In eutectic
Zn(NO ₃) ₂ · 4 H ₂ O	Eladic acid	Bi–Pb–In
NaOH · H ₂ O	Lauric acid	Bi–Pb–tin
Na ₂ CO ₄ · 10 H ₂ O	Polyethelene glycol	Bi–Pb
CaBr ₂ · 6 H ₂ O	Tristearin	
FeCl ₃ · 6 H ₂ O	Stearic acid	
FeCl ₃ · 2 H ₂ O	Phenol	
NA ₂ SIO ₃ · 4 H ₂ O	Cetyl alcohol	
Na ₂ PO ₄ · 12 H ₂ O	Oxalate	
Gallium		

differential scanning calorimetry (DSC). The DSC is largely employed. It has two different configurations: power compensation DSC and heat flux DSC. Generally, a DSC measures the difference in heat flow rate (common unit: mW= mJ/s) between a sample (PCM) and inert reference (usually Al₂O₃) as a function of time or temperature. The sample size of a DSC test is very small, depending on the properties of the sample. For PCM, this value is typically couple of milligram.

The *heat flow signal* ($\frac{dQ}{dt}$) measured by DSC is defined in Eq. 1.3, where $f(T, t)$ is the heat flow that is a function of time at an absolute temperature; $\frac{dT}{dt}$ is the heating rate and C is the sample heat capacity equal to "sample specific heat $C_p \times$ sample weight".

$$\frac{dQ}{dt} = C \frac{dT}{dt} + f(T, t) \quad (1.3)$$

The typical output of a heat flux DSC measurement is one/several heat flow (mW/g) curve(s) as a function of temperature (°C) at one/several heating rate (°C/min). From those curves, we can obtain latent heat of fusion (the area between the curve peak and the phase change temperature); the phase change temperature (the intersection between the tangent line of the biggest slope and the base line), and the specific heat. A typical DSC curve is illustrated in Figure 1.4.

1.3.2 Application of LHS on buildings

The principal motive behind the employment of PCMs during modern building design is that the PCMs are able to increase the heat efficiency of

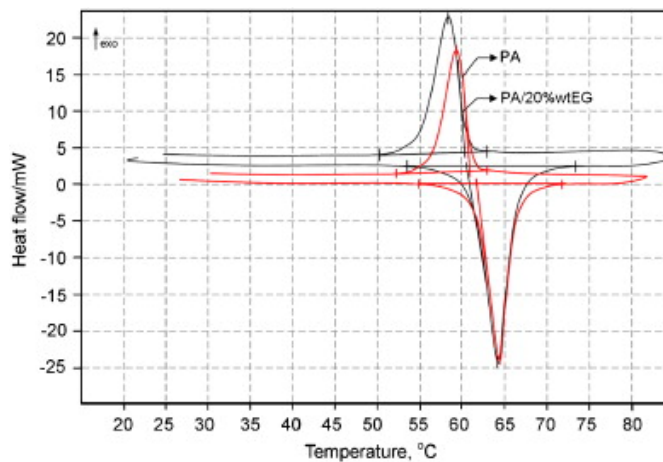
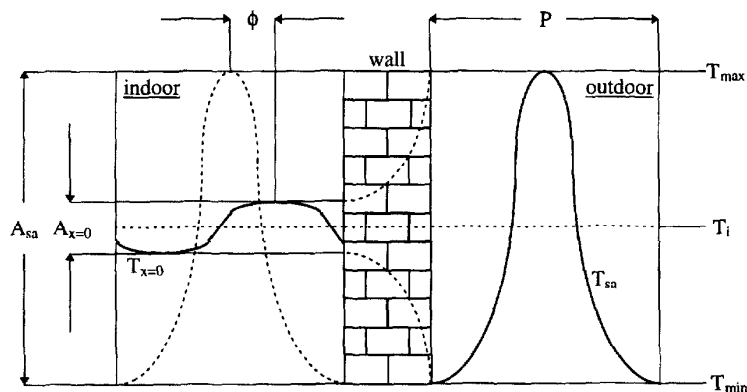


Figure 1.4 – Typical DSC measurement output curves [11]

Figure 1.5 – Time lag ϕ and decrement factor f of the indoor temperature as against the outdoor temperature [12]

modern buildings. One of the most important functions of buildings is to provide an amiable ambient temperature for us. This amiable temperature generally ranges from 18°C to 28°C . However, buildings' inside temperature is considerably impacted by the exterior circumstances, for instance, the outside temperature, the wind speed, the solar radiation *etc.* The relation between indoor and outdoor temperatures are shown in Figure 1.5, from this figure we can find that the inside temperature fluctuates with the outside ambient temperature but has "time lag ϕ " and "decrement factor f " [12].

On a larger scale of time than that in Figure 1.5, *e.g.* one year, the exterior and interior temperatures evolve as shown in Figure 1.6. When the indoor temperature passes beyond the amiable temperature range, the extra heat load must be added or removed either by air-conditioning or by

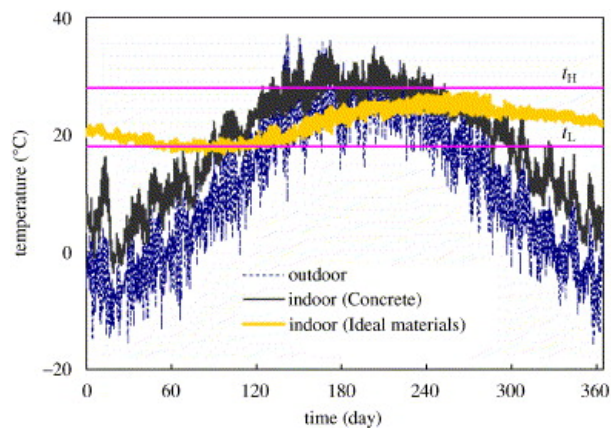


Figure 1.6 – The indoor and outdoor temperature evolutions [13]

heating system. Undoubtedly, the PCMs can be used to compensate this extra heat load, and as a result, to attenuate interior temperature fluctuation.

Furthermore, PCMs can also be used to economize expense by storing heat generated by electrical heating system during winter night and then release it in the daytime, since in many countries electricity price has an off-peak price discount. In addition, in summer, PCMs can be used to absorb the excessive solar radiation heat and maintain a bracing indoor ambience.

From the brief description above, it is clear that the PCMs have a fundamental role in optimization of buildings' heat performance. Therefore, in this section we are going to give an account of the main aspects of a viable application of LHS - by means of PCMs - on buildings. It covers:

- ⇒ the possible ways to realize the PCMs implantation into buildings, their advantages and disadvantages (sec. 1.3.2.1);
- ⇒ different application scenarios and their heat performances (sec. 1.3.2.2);
- ⇒ the attainable approaches to enhance heat performance (sec. 1.3.2.3);

1.3.2.1 PCM implantation

There exist many ways to implement the PCMs into buildings. One of the elaborate review articles on the subject of the PCMs implementation in building walls is given by Frédéric K. *et al.* [14]. However, we are going to classify these incorporation approaches from a different point of view.

PCMs without their physical forms In this approach of incorporation, PCMs lose their original physical forms and mix well with the building envelop construction materials such as cement, concrete, gypsum and so on. This method can be called direct method.

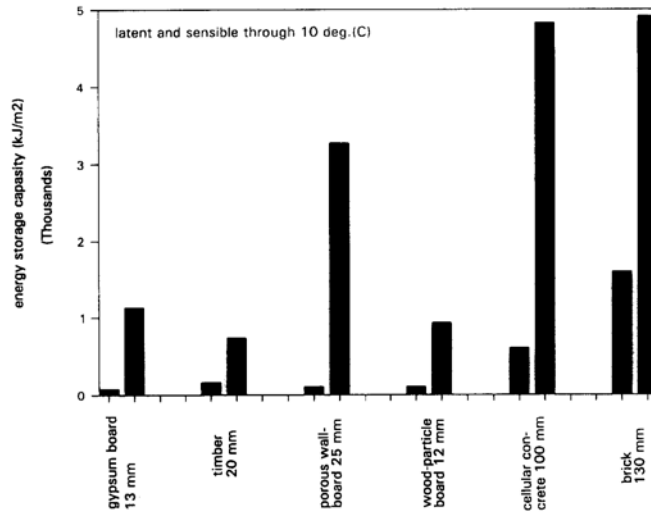
The simplest direct incorporation is to mix the PCMs in liquid phase or solid powder status with the natural porous materials during the fabrication process of building envelop, named as *direct mixing approach*. Feldman D. *et al.* made a laboratory scale gypsum board with 21%-22% of commercial butyl stearate. They announced that this new type of gypsum board had comparable physico-mechanical properties with the tradition gypsum board [15] but had ten-fold increase in capacity for storing and discharging of heat. This method of incorporation does not add extra procedure to the traditional building envelop fabrication process, and thus does not need additional facilities. Notwithstanding, the leakage is the major imperfection [16].

Another direct incorporation method is characterized by its immersion process. The idea is similar to the direct mixing approach, as the PCMs are stored inside the pores of building materials. However, the incorporation process is not integrated into the normal fabrication process. Instead, the traditional building materials are dealt with by being completely immersed into liquid PCMs and until they get saturated with PCMs. After this treatment, the PCMs can stay inside the porous materials. H. Kaasinen studied the absorption of different PCMs into the porous building materials [17], and found that the porous wall-board and gypsum board filled with PCMs had a considerable increment of heat capacity (Figure 1.7), and that different types of PCMs can give different heat capacity augmentations (Figure 1.7a, Figure 1.7b). Regrettably, without post-treatment of the building materials, such as coating, the leakage still exists.

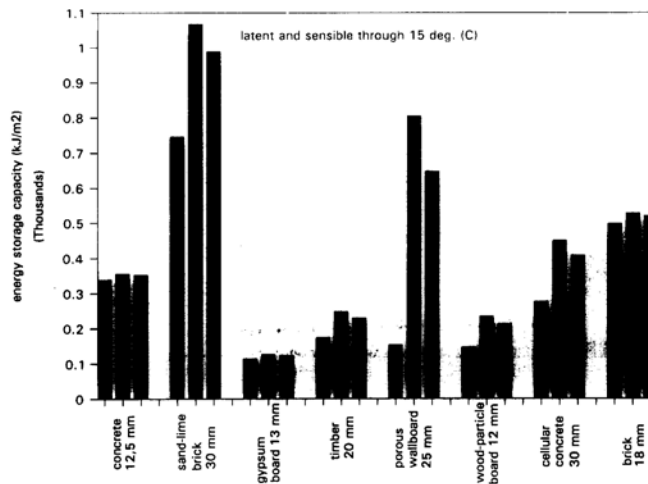
The common defections of the two methods are that the PCMs leak and that some PCMs have negative impacts on the mechanical characteristics of building materials [18, 19]. In order to get rid of this leakage trouble and the interaction between PCMs with building matrix materials, the micro-encapsulations of PCMs appear as an alternative.

With micro-encapsulation, the PCMs are encapsulated inside polymer capsules before incorporated into the building materials. Because of the enclosure of the capsule, the leakage disappears. Those micro-capsules are incorporated into the building materials with the same process as the direct mixing approach. From the SEM picture (Figure 1.8), we could see the micro-capsules scatter homogeneously within a gypsum board and have a diameter around several μm [19]. Besides, if made of the appropriate inert materials as the capsule, the micro-encapsulation does not interact with the building matrix materials. As a results, the micro-encapsulation PCM materials have not only the same advantages as direct mixing approach, for instant easy incorporation, but also its proper advantage, such as increased heat transfer rate [19].

The three basic parameters of micro-encapsulation PCM power are the mean diameter of the capsule, the thickness of the capsules' shell and the



(a) Carbonxylic acid as PCM



(b) Polyalcoholes acid as PCM

Figure 1.7 – The heat capacities of some building materials before and after the incorporation of PCMs [17]

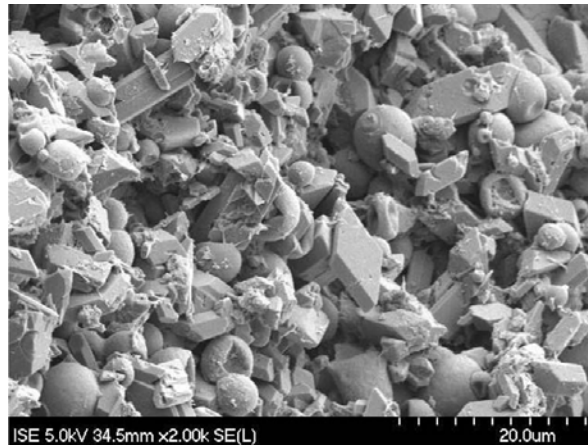


Figure 1.8 – SEM image of PCM micro-capsules in gypsum plaster [19]

mass ratio of PCM as against the total mass. All of them can exert impacts on the thermal performance and mechanical characteristics of micro-encapsulation PCM powder. Yamagishi Y. *et al.* [20] studied the thermal properties, rheological properties and the structural integrity of micro-encapsulation PCM powder. They evaluated the micro-encapsulation PCM powder with diameters ranging from 5 μm to 1000 μm ; and discovered that the structural stability of the micro-encapsulation PCM powder had a dependence on their diameters. In addition, the supercooling of micro-encapsulated PCM induced by the size was detected through differential scanning calorimetry (DSC). The supercooling is attributed to the lack of nucleating agent when the size of micro-encapsulated PCM decreases. By adding 10.0 wt% of 1-octadecanol as a nucleating agent, X.-X. Zhang announced that the degree of supercooling of micro-encapsulated n-octadecane decreased according to DSC experimental results [21].

In the past couple of years, apart from the previous direct incorporation methods, an innovative approach using shape-stabilized PCM has become a hot research topic [16, 22, 23]. A shape-stabilized PCM is a mixture of PCMs and supporting materials. The reported supporting materials are high-density polyethylene (HDPE) [24] and styrene-butadiene-styrene (SBS) [16]. The Figure 1.9 illustrates the shape-stabilized PCM and its micro structure.

A well-fabricated shape-stabilized PCM can incorporate PCMs with a mass proportion up to 80% and during the working cycles, there are no leaking cases are reported yet. As a matter of fact, due to the high mass proportion of PCM, shape-stabilized PCM's thermophysical properties are similar to the traditional PCMs. Consequently it inherits both the advantages and disadvantages of traditional PCMs, such as low heat conductivity. However, published research papers reported that a suitable additive

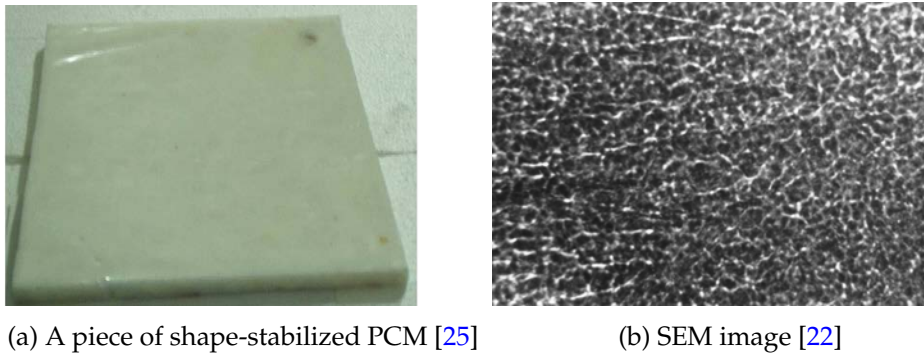


Figure 1.9 – Shape-stabilized PCM

can increase this heat conductivity [26].

PCMs with their physical forms In this approaches, the PCMs do not need to be mixed with neither building materials nor support materials. They are filled into containers of variable geometrical shapes. Those filled containers are after embedded into building envelop. The common shapes of those containers are rectangular and cylindrical. The containers' materials are, for example, PVC or metals.

Rectangular shape In general, this type of containers are used as a panel. Together with other types of panels, they could be employed to fabricate the building envelop, *e.g.* [27,28]. A. Carbonari *et al.* [29] numerically and experimentally tested this type building walls named as sandwich panels. They found this sandwich panels have a good heat performance and can also facilitate the fabrication of building envelop. Kim and Darkwa [30] evaluated another type of PCM multi-layer panels (Figure 1.10), and found that this panel could achieve 7% more phase change process and 27% more latent heat than the PCM board from the direct mixing approach. Weinslader [31] filled PCM in a double glazing and said this type of windows had promising characteristics. This double glazing has 0.4 of light transmittances and 30% less heat loss in south oriented facades.

Cylindrical shape The PCMs are filled inside a cylindrical container and then built inside the building envelops. Voelker *et al.* [32] filled PCM into six tubes (63 × 1000 mm) and put them under the ceiling of testing room. Their results show that in summer the indoor peak temperature decreased by at least 4 °C.

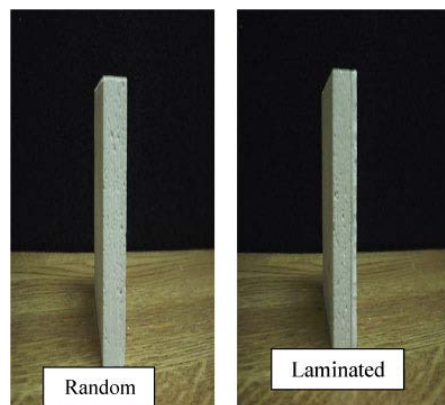


Figure 1.10 – Direct mixing and laminated PCM board [30]

1.3.2.2 Different application scenarios

No matter which type of incorporation and where the PCMs are integrated into building, their essential task is to charge and discharge energy in the form of latent heat. Depending whether the process of LHS is driven by electricity or not, the PCM applications on buildings are classified as the positive system and the negative system.

1.3.2.2.1 The active heat storage system In the active systems, the phase change latent heat storage is driven by electricity, including building heating and cooling. Active systems are suitable to and mainly used to economize expense on electricity, because the electricity consumption varies over day and night. In general, men consume less electricity during the night than the day. As a result, in most countries and regions, floating electricity pricing mechanisms are deployed, which means the electricity price adapts to this consumption variation, cheaper in the off-peak time period.

1.3.2.2.1.1 Electric heating floors One application scenario of the active system is floor heating in cold days. M. Amir [33] experimentally estimated the heat performance of two types of electric heat floors, one type being filled with water and another with n-octadecane. Two testing cases were carried out, where heat was stored in the form of sensible heat and latent heat. The results demonstrated that the concrete containing n-octadecane had less volumetric size, higher heat mass capacity and could attenuate the indoor temperature fluctuation more effectively than the concrete containing water. Farid and Chen [34] simulated the utilization of a underfloor PCM layer combined with an electrical heating unit. The main purpose was to evaluate the possible advantages of increasing the heat mass of the building floor. The simulation results showed that after 8 hours

preheated by electricity during the off-peak period, this 30 mm thick PCM layer could continuously discharge heat and maintain the room temperature for the entire coming daytime. The author also asserted that this type of underfloor application was also valid when applied to building walls or ceilings. Lin *et al.* [35] used the shape-stabilized PCM board in an under-floor heating system (Figure 1.11). The shape-stabilized PCM consisted of 75 wt · % paraffin as a dispersed PCM and 25 wt · % polyethylene as a supporting material (Figure 1.9a). The paraffin's phase transition temperature is 52 °C and its latent heat of fusion is about 200 kJ/kg. Three conclusions were drawn: 1. The system increased the indoor temperature without increasing the temperature difference; 2. The temperature of the PCM plates was kept at the phase transition temperature for a long period after the heaters stopped working. More than half of the total electric heat energy was shifted from the peak period to the off-peak period, which would provide significant economic benefits; 3. Small indoor temperature difference along vertical direction appeared because the under-floor heating could warm the indoor air uniformly. The heating system was comfortable and energy-efficient.

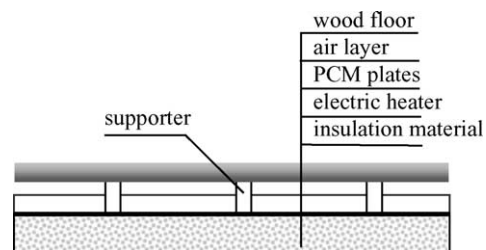


Figure 1.11 – Schematic of electric floor heating system with shape-stabilized PCM plates [35]

1.3.2.2.1.2 Air-conditioning ceiling On the contrary of electric heating system which is used in winter to store latent heat during electricity off-peak time and discharge it over daytime (*e.g.* Figure 1.12), air-conditioning ceilings are used mostly in regions where the climate temperature varies significantly between day and night. During the day, the solar radiation is stored inside of PCM incorporated in the ceiling in the form of latent heat; during the night, the PCM is cooled down by, for example, fresh air ventilation propelled by electricity driven fans or by compression refrigerators.

M. Koschenz *et al.* [36] described a thermally activated ceiling panel which included the compression refrigerators providing the necessary cooling energy. It was demonstrated, by numerical simulations and laboratory tests, that a 5 mm layer of micro-encapsulated PCM (25% by weight)

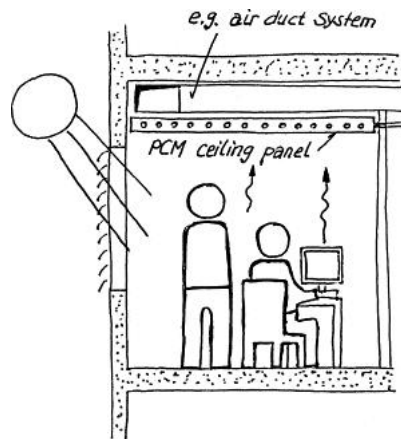


Figure 1.12 – Installation of ceiling panels in building interior as suspended ceiling [36].

and gypsum suffices to maintain a comfortable room temperature in standard office buildings. The system's features also make it ideal for use in lightweight structures, the incorporation of additional thermal mass offering an efficient means of moderating temperature amplitudes in this type of building. M. Jaworski [37] numerically and mathematically studied a form of PCM ceiling panel made of gypsum and micro-encapsulated PCM. Relevant experiments were performed to validate the numerical model. Results confirms that these ceiling panels effectively decrease the air temperature oscillation inside buildings.

1.3.2.2.2 The passive heat storage system The term *passive* means that, during the heat storage process, the heat or cold sources are not from artificial energy, *e.g.* electricity, but from the nature. Solar radiation is one of the sources of greatest importance. Low temperature air during the summer night also is an ideal source of coldness. In a passive system, there is no commercial energy involved, making this type of system more attractive than the other.

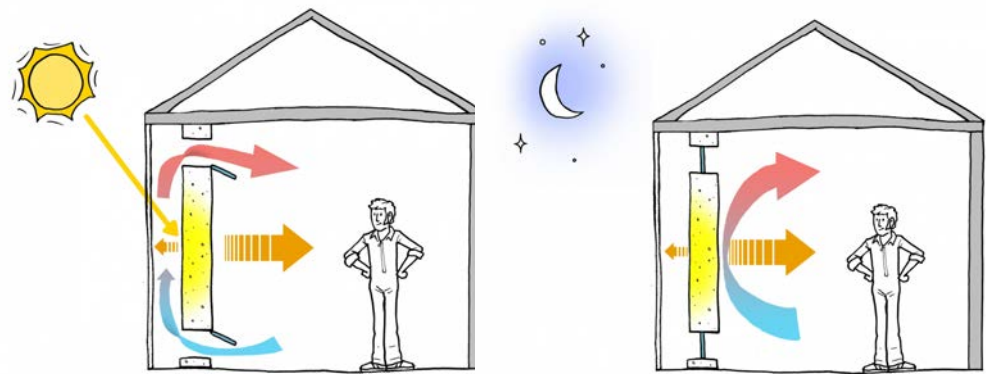
The roofs and walls, together with the windows, are the most important parts that can absorb directly the solar radiation. Many successful application cases published can be found.

1.3.2.2.2.1 PCM walls One of the most well-applied and well-known passive system applications is Trombe wall (Figure 1.13). It consists in a south-oriented masonry wall with a transparent glazing in front. The air can flow through between the masonry wall and glazing thanks to the natural convection. The glazing let the solar radiation pass through and be finally absorbed by the masonry wall (except for the reflection) during the

sunny days. When the wall temperature rises, it starts to emit heat to the inside of the room. The traditional Trombe wall absorbs heat in the form of sensible heat and discharges it by radiation. Due to their low specific heat capacity, the Trombe walls are considerably bulky in size. Because of this shortcoming, the researchers have begun to try utilizing PCM to enhance the heat performance of Trombe walls. Because of the high latent heat of fusion, the Trombe walls incorporated with PCM have small and reasonable size but high heat efficiency. Ghoneim *et al.* [38] numerically investigated the use of PCMs as a collector-storage wall, an improved version of Trombe wall. They concluded that using the PCMs may be a preferable alternative to the use of sensible storage in a traditional Trombe wall (masonry or water as material) on the basis of volume, heat mass. The authors also underlined the importance of appropriately selecting PCMs containers from the point of view of compatibility and durability. Gracia *et al.* [39] experimentally tested a ventilated facade with micro-encapsulated PCM in the air cavity (similar to the air gap between glazing and Trombe wall) of a house-like cubic with size $2.4\text{m} \times 2.4\text{m} \times 5.1\text{m}$. A reference experiment was performed in parallel. Results show that the thermal performance of the whole cubicle is improved by the use of this ventilated facade under free floating conditions. While the indoor temperature of the reference cubicle drops daily due to the outer temperature's oscillations, the use of the ventilated facade with PCM increases the temperature every day from 9°C to 18°C under severe winter conditions. Chandra *et al.* [40] numerically studied the time-dependent periodic heat transfer of a non-air-conditioned building having a south-facing wall of phase-changing component material (PCCM). Results show that a PCCM wall of small thickness is more desirable than an ordinary masonry concrete wall for providing efficient thermal energy storage and excellent thermal comfort in buildings.

Some published papers study the other types of wall boards than modified Trombe walls. Peippo *et al.* [41] used a numerical approach to find the optimum phase transition temperature and thickness of a PCM wall. Their results indicate that the optimum fusion temperature of PCM is about 1 to 3°C above the mean room temperature. According to this, in the typical climates of Helsinki, Finland and Madison, Wisconsin, the ideal candidate PCMs would be fatty acid and their mixtures. Their simulation results also show that the energy consumption of this PCM wall in the passive system reduces by between 5% and 20%, depending on the real climate. Feldman D. *et al.* [15] made a laboratory scale gypsum board with 21%-22% of commercial butyl stearate. They announced that this new type of PCM gypsum board had comparable physico-mechanical properties with the tradition gypsum board but had tenfold increase in capacity for storage and discharging of heat.

Athienitis *et al.* [42] studied the application of a gypsum wall board im-



(a) A vented Trombe wall heats air convectively as well as heating the space radiatively
 (b) Vents can be shut at night to keep the convection loop moving the right direction.

Figure 1.13 – Trombe wall ^a

a. Source: <http://sustainabilityworkshop.autodesk.com>

pregnated with a PCM. An explicit finite difference model was developed to simulate the transient heat transfer process in the walls. Experiments were also carried out. Reasonable agreement between the simulation's and the experiment's results was achieved. It was shown that the utilization of PCM gypsum board in a passive solar building may reduce the maximum room temperature by about 4 °C during the daytime and can reduce the heating load at night significantly.

Oliver [43] studied the thermal behaviour of a new construction material for building walls: gypsum board containing 45% by weight of phase change materials (PCMs) reinforced with additives. The thermal storage capacity of different construction materials with similar use and position in buildings has been evaluated and compared. The results show that a 1.5 cm thick board of gypsum with PCMs stores 5 times the thermal energy of a laminated gypsum board, and the same energy as a 12 cm thick brick wall within the comfort temperature range (20–30 °C).

1.3.2.2.2 PCM windows and shutters The building walls are in general light-opaque, we don't need them to be light transparent. However, not like the walls, windows must provide two functions in a building: nice isolation of heat and high light transmittance. Since many kinds of PCMs are highly transparent for visible part of solar radiation and at same time absorb the infrared, the two desired functions can be effectively achieved by double or triple glazing system with PCMs. In addition, this type of glazing system has also been applied to the Trombe walls system.

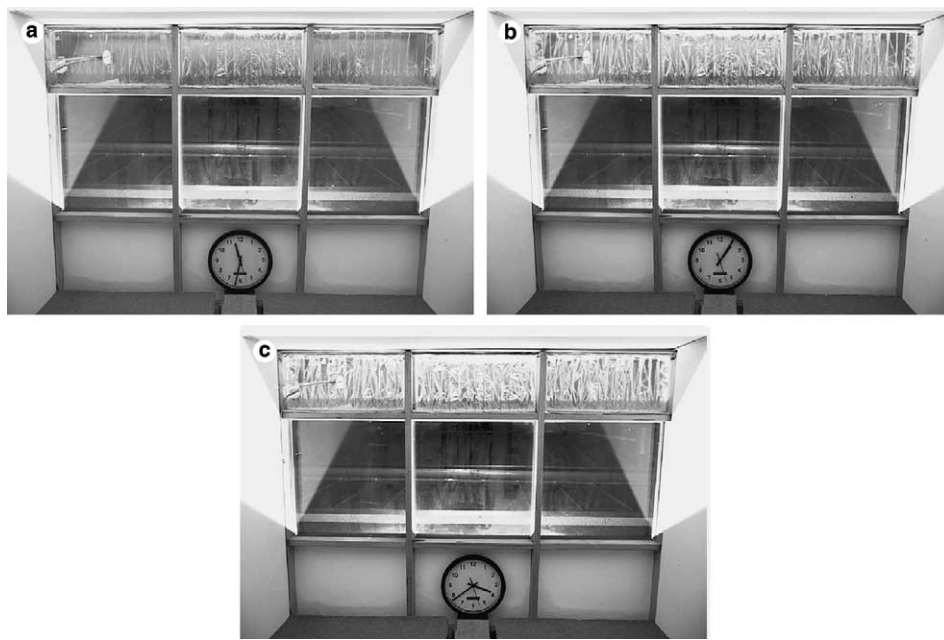


Figure 1.14 – Crystallisation process of S27 (upper part of the window). The material solidifies in the shape of crystal needles which keep growing until they draw through the whole container (picture sequence up to down) [31].

Weinlader *et al.* [31] carried out a set of experiments to evaluate a façade panel with double glazing and PCMs filled in between (Figure 1.14). Light transmittances in the range of 0.4 can be achieved. Compared to a double glazing without PCM, a façade panel with PCM shows about 30% less heat losses in south oriented façades. Solar heat gains are also reduced by about 50%.

In Goia *et al.*'s work [44], a prototype of a simple PCM glazing system was proposed and its behaviour was compared with that of a conventional reference double glazed unit. The thermal conditions of the indoor environment have been considerable improved by this PCM glazing system. In general, it has been observed that the higher the outdoor solar radiation, the greater the benefits. Apart from an improvement in thermal comfort conditions, the presence of a PCM in the façade could also positively influence visual comfort, as it may prevent glare.

Grynning *et al.* measured the performance of a commercially available window that integrates PCM using a large scale climate simulator. The glazing unit consists of a four-pane glazing with an integrated layer that dynamically controls the solar transmittance (prismatic glass) in the outer glazing cavity. The innermost cavity is filled with a PCM, contained in transparent plastic containers. It was found that even for temperatures similar to a warm day in Nordic climates, the potential latent heat storage

capacity of the PCM was fully activated. However, lower melting point temperatures for the PCM could be considered for cold climates in order for a better utilization of the latent heat storage potential.

Another part of buildings always combined with windows are the shutters. The shutters could be designed with PCM inside and placed outside of the windows. Esam M. Alawadhi [45] investigated a window shutter filled with PCM. This was a method for reducing the heat gain in buildings during the working hours. Results show that the melting temperature of PCM should be close to the upper temperature limit of windows during daytime. The quantity of PCM should be sufficient to absorb large quantity of heat during the daytime, and PCM should be prevented from complete melting during the working hours. Heat gain through windows can be reduced by 23.29% when P116 PCM shutters are used with thickness of 0.03 m.

1.3.2.2.3 PCM roofs and ceilings Huann-Ming Chou [46] experimentally and numerically studied a metal sheet roof utilizing phase change materials to fit its thermal performance with the desired thermal comfort in the indoor space. When 1 kg of PCM which had melting temperature of 46.3 °C and latent heat capacity of 90 kJ/kg was used to cover 48% of the roofing surface with ambient temperature 25 °C, the energy saving rate reached 52.7% compared with the rate of 43.1% of the normal insulated roof.

Jan Kosny [47] evaluated a type of roof made of roof-integrated PV laminates, air cavities, dense fiberglass insulations with reflective foil facing, and PCM heat sink. Field-test data were collected between November 2009 and October 2010, and demonstrated that, during winter, without the phase change contribution, the PV-PCM attic had a 30% reduction in roof-generated heating loads compared to a conventional shingle attic. On the other side, during the cooling season, the attic generated cooling loads from the PV-PCM attic were about 55% lower than the shingle attic. In addition, about 90% reductions of roof peak heat flux in daytime were observed with the PV-PCM roof.

1.3.2.3 Heat performance enhancement

As mentioned in previous sections, the major hindrance to achieve very high heat performance of PCMs is their low heat conductivity. In addition, Cabeza *et al.* [48] concluded that while unloading a latent heat storage, the solid-liquid interface moves away from the heat transfer surface and the heat flux decreases due to the increasing thermal resistance of the growing layer of the molten/solidified medium.

One approach is to modify the LHS system structure to get higher heat performance. Using fins, for instance, has been proven an effective way. Velraj *et al.* [49] investigated the different heat transfer enhancement methods for the latent heat thermal storage system. The heat transfer enhancements with fin configuration for storage tubes and with lessing rings in storage tanks are appreciable, and these two methods are highly suitable for solidification enhancements.

Another approach is to modify the PCM incorporation method into the building envelop. For example, the laminated PCM board (Figure 1.10) tested by Kim and Darkwa [30] has better heat performance than the direct incorporated PCM board.

The last but not the least approach is to increase the PCMs' own heat conductivity. This can be achieved by adding high heat conductivity additives. Ahmed Elgafy and Khalid Lafdi [50] used carbon nanofibers to enhance the thermal performance of a PCM during its phase change. The thermal properties of the modified PCM were enhanced significantly by dispersing carbon nanofibers into it.

In Cabeza *et al.*'s study [48], three enhancing methods were tested: stainless steel tubes, copper tubes and graphite matrix. Results show that the addition of stainless steel does not give much improvement, while copper and the graphite composite material gave an improvement of 120% and 250%, respectively in heating, and of 50% and 150%, respectively in cooling. The main conclusions are:

- ⇒ Addition of stainless steel pieces in the PCM does not increase the heat flux significantly.
- ⇒ Addition of copper pieces enhances heat transfer significantly, especially in the melting period (discharge of the store).
- ⇒ The use of graphite composite allows an even larger increase in heat transfer than with copper. The heat flux is about four times larger on heating and three times larger on cooling as compared to using pure ice.
- ⇒ With the addition of stainless steel pieces, the melting/freezing front does not show any change. This corresponds to the unchanged heat flux.
- ⇒ With the addition of copper pieces, the melting/freezing front is not regular but is strongly influenced by the metal pieces.
- ⇒ With the addition of the graphite matrix composite, the movement of the phase front cannot be seen, because the pores in it are too small. But it is reasonable that the phase front is also irregular.

1.3.3 Literature review on natural convection with phase change

Over the past 20 years, solid liquid phase change has been studied using either numerical or experimental methods. The phase change phenomenon is a very complex non-linear problem which couples three basic phenomenons: natural convection heat transfer in the liquid phase, heat conduction in the solid phase and moving liquid-solid interface.

1.3.3.1 Experimental and analytical study

Experiments are carried out to well understand physical phenomenon of the phase change and to validate the relevant numerical simulation results or the analytical results. In the publications, a large number of different kinds of PCMs with different enclosures are studied. The enclosures are often of rectangular or cylindrical shapes. The experimental results are very often formulated in the form of mathematical correlations.

M. Okada [51] analysed a two-dimensional melting in a rectangular enclosure by means of a finite difference method under the quasi-steady state assumption. A vertical wall between insulated top and bottom surfaces was heated so as to provide a step-wise temperature change. The PCM was initialised as liquid at the fusion temperature. The analytical results of the melting front and the temperature distribution along the centerline of the enclosure were compared with his own experimental results. He concluded correlations of the variation of dimensionless thermal energy stored as latent heat, and the average Nusselt number on the vertical wall with the dimensionless time (Eq. 1.4).

$$\overline{Nu}_w = \begin{cases} \frac{1}{\sqrt{2\tau}} & \text{when } \tau \leq \tau_t \\ \overline{Nu}_{wt} [1 + C(\tau - \tau_t)] & \text{when } \tau > \tau_t \end{cases} \quad (1.4)$$

where

$$\overline{Nu}_{wt} = \frac{1}{\sqrt{2\tau_t}} \quad (1.5)$$

and C is a coefficient and τ_t is transition time from conduction to convection. When the melting becomes stable, the average Nu is:

$$\overline{Nu}_{wt} = 0.234Ra^{0.266} \quad (10^4 \leq Ra \leq 5 \times 10^6) \quad (1.6)$$

Since there is no heat conduction in the solid phase, the dimensionless location of the melting front equals:

$$\frac{d\bar{F}}{d\tau} = \overline{Nu}_w \quad (1.7)$$

as a result, the correlation of \bar{F} is:

$$\bar{F} = \begin{cases} \sqrt{2\tau} & \text{when } \tau \leq \tau_t \\ \sqrt{2\tau_t} + \overline{Nu}_{wt}(\tau - \tau_t) \{1 + C(\tau - \tau_t)/2\} & \text{when } \tau > \tau_t \end{cases} \quad (1.8)$$

The main conclusions were:

1. The good agreement between the analytical and experimental results indicates that the present analytical method which uses the quasi-steady state assumption and the two-step variable transformation technique is viable.
2. In the quite early stage of melting, pure heat conduction dominates the melting process. After this early stage, the natural convection in the melted region dominates it.
3. In the period of the natural convection domain, the average Nusselt number on the vertical wall varies linearly with the dimensionless time but its variation is small. Therefore, the dimensionless thermal energy stored as latent heat varies almost linearly with the dimensionless time.
4. The average Nusselt number on the solid-liquid interface decreases with the dimensionless time as the surface area of the solid-liquid interface increases.
5. Both the average Nusselt number on the vertical wall and the dimensionless thermal energy stored as latent heat were expressed by simple relations with Rayleigh number and the dimensionless time.
6. Concerning the melting around a vertical cylinder, the Prandtl number does not affect the melting rate for $Pr > 7$ when the Rayleigh number is used.

Bénard C. *et al.* [52] provided another correlation to describe the melting fraction $F(t)$ in a rectangular enclosure based on the following hypotheses.

- ⇒ the PCM is newtonian, incompressible, and satisfies the Boussinesq approximation
- ⇒ the flow in the liquid cavity is two dimensional (end-wall effects are negligible)
- ⇒ the flow in the liquid cavity is laminar
- ⇒ the melting front is smooth
- ⇒ the convective flow is not strongly influenced by the movement of the melting front.
- ⇒ the density change upon melting has a negligible effect on the process
- ⇒ the quasi-stationary of the melting process

Before the solid-liquid interface contacts the enclosure wall, the correlation is in the following form:

$$F(\hat{t}, \hat{t}_0) = A(\hat{t} + \hat{t}_0) \quad (1.9)$$

where

$$\hat{t} = 0.33Ra^{1/4} \frac{\rho_L Ste}{\rho_s Pr} t \quad (1.10)$$

$$\hat{t}_0 = 1/0.66Ra^{1/4} \quad (1.11)$$

and A is the aspect ratio of the enclosure.

C.-J. Ho and R. Viskanta [53] performed an experiment with a different configuration to obtain the heat transfer data and the information on solid-liquid interface. The phase change occurred in a rectangular enclosure equipped with a heating wall in copper at the bottom and two conductive vertical aluminium walls. Based on the experimental data, a correlation is deduced by least square. The melting fraction V/V_0 is:

$$V/V_0 = 16.8\tau_1^{0.728} \quad (1.12)$$

where $\tau_1 = SteFo$ is the dimensionless time.

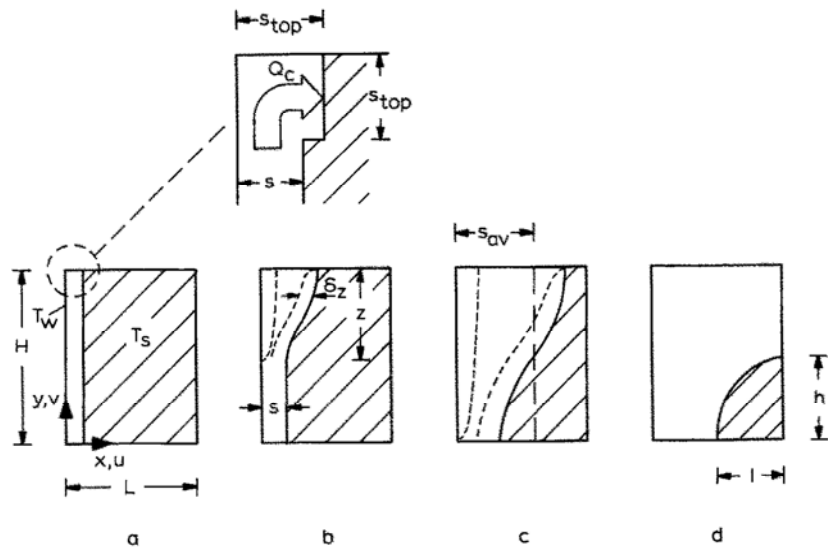


Figure 1.15 – Four-region model for scale analysis [54]

J. Peter and A. Bejan identified the most basic scales and regimes of the melting driven by natural convection in an enclosure heated from the sides [54]. The four-region model used for the scale analysis is shown in Figure 1.15. The initial temperature of solid PCM is equal to its melting

temperature¹. A numerical simulation was also carried out to validate the scaling analysis. The melting domain has square shape, and $0 \leq Ra \leq 10^8$, $Pr = 50$, the Ste is of the order 0.1. The simulation time is demonstrated in the dimensionless form $\theta = SteFo$. The correlation of heat transfer rate (Nu) and melting fraction (S_{av}) are:

$$Nu = (2\theta)^{-\frac{1}{2}} + \left[c_1 Ra^{\frac{1}{4}} - (2\theta)^{-\frac{1}{2}} \right] \left[1 + \left(c_2 Ra^{\frac{3}{4}} \theta^{\frac{3}{2}} \right)^n \right]^{\frac{1}{n}} \quad (1.13)$$

$$S_{av} = \left\{ \left[(2\theta)^{\frac{1}{2}} \right]^m + \left[c_1 Ra^{\frac{1}{4}} \theta \right]^m \right\}^{\frac{1}{m}} \quad (1.14)$$

where the coefficients $c_1 = 0.35$ $c_2 = 0.0175$ $n = -2$ and $m = 5$.

When the convection in the melting process dominates, it approaches pure convection in the same enclosure. According to the pure convection scaling law,

$$Nu = c_1 Ra^{\frac{1}{4}} \quad \text{when } Pr > 1 \quad (1.15)$$

A. Bejan *et al.* proposed another more general correlation of Nu , in order to consider the impact of Pr , which is compatible with an arbitrary Pr :

$$Nu = \frac{0.35 Ra^{\frac{1}{4}}}{\left[1 + \left(\frac{B}{Pr} \right)^{\frac{9}{16}} \right]^{\frac{4}{9}}} \quad (1.16)$$

with $B = 0.143$.

Apart from those pioneering attempts to better understand phase change, there also exists many other approaches. Bénard C. *et al.* [55] studied the effects of conduction in the solid phase when melting. The authors compared their numerical results with the experimental results and found relatively good agreements. Some hypotheses were verified as acceptable: for example that the melting in the rectangular enclosure is a quasi-stationary process, the natural convection in the liquid phase is supposed to be laminar *etc.*

Agyenim F. [56] studied the heat transfer enhancement methods and the optimized parameters of phase change heat transfer of PCM.

In the relatively recent research carried out by Shmueli H. [57], the melting of PCM in a cylindrical tube is numerically analysed and compared with the experimental results. They obtained the local melting fraction; flow vector map and heat transfer rates.

Compared to abundant researches on melting, publications about solidification of PCMs are quite rare. Kalaiselvam S. [58] analytically and experimentally studied the solidification and melting of PCM in an encapsulated cylinder. They found that the solid-liquid interface could be well

1. The degree of solid subcooling is zero

predicted by their analytical model when solidification occurred. The heat generation value had a threshold by which we can determine whether the solidification reached a steady state. They also found that the solidification and melting fraction were proportional to the Stefan number. Their experiments and analysis had 16.11% deviation.

Stritih U. [59] studied the solidification and melting of PCM encapsulated in a rectangular container with fins on the inner surfaces as enhancement method. A new correlation of Nu and Ra numbers during melting is introduced (Eq. 1.17). For solidification, heat conduction was found to be the dominant factor.

$$\text{Nu} = 8 \times 10^{-12} \text{Ra}^{1.0392} \quad (1.17)$$

As a result, applications of the heat transfer enhancement such as fins were more effective when solidifying than melting.

1.3.3.2 Numerical study

Precisely designed and performed experiments in most case are the most reliable approaches to understand the phase change. The numerical approaches are to a great extent indispensable to evaluate a phase change system and enable the researcher to optimize the system design, select the appropriate PCMs and thus reduce the overall system cost. However, to numerically simulate phase change has been considered as a challenging task. Phase transition of a material is described by a set of partial differential equations with time dependent boundary conditions. This type of phase change problems are generalized by Stephan. It is difficult to get analytical close solutions due to their non-linear nature and the moving boundary [60]. Because of the existence of two different phase -solid and liquid- and solid-liquid interface as well. Three different equations are needed. For the interface - which connects the solid phase and liquid phase - the Stephan condition is applied as follow:

$$\rho L_f \frac{dS}{dt} = k_s \left(\frac{\delta T_s}{\delta t} \right) - k_l \left(\frac{\delta T_l}{\delta t} \right) \quad (1.18)$$

where subscript s and l indicate solid and liquid phases respectively, T is temperature, k is heat conductivity, S is the interface location, and t is time.

1.3.3.2.1 Adaptive mesh In order to precisely trace the evolution of the phase change interface, a very fine meshing is mandatory. However, for most parts of the calculation domain - in the solid and liquid phases - augmenting the mesh density is a waste of computation time. Many researchers announce that the choice of the mesh size is a compromise between simulation accuracy and computation time. For example, in Hannoun's [61] report, the 200×200 -grid simulation up to time 2500 s required 2400 CPU hours,

111 runs (restarts), and 3 months of calculations on a Compaq Alpha (667 MHz, ev67) processor. It requires about 980 CPU hours to check the solution of the gallium melting of 32 s with 1120×800 grids.

Consequently, adaptive mesh was invented to help obtain precise interface locations and economize the computation CPU time. Two major methods are widely used. The first one is called local mesh refinement method, *i.e.* h -method and the second is called moving mesh method, *i.e.* r -method.

H -method is widely used by commercial applications. The major difficulty in its application is the maintenance of the data structure, which the r -method does not require. For detailed application cases, one can refer to the relevant published studies on h -method [62–65] and r -method [66–68].

The adaptive mesh method to simulate phase change has been proven a nice approach. Nevertheless, it is hard to solve the cases that have complex enclosures - after each time step, the coordinate of the calculation domain must be refreshed - and the governing equations are very complex. Furthermore, Bertrand *et al.* [69] also noticed that this adaptive mesh method could fail to simulate the cases where the transition from the liquid to solid is not a macroscopic surface.

1.3.3.2.2 Fixed mesh Because of its simplicity and mature algorithms, the fixed mesh method remains an excellent choice, especially when the detailed solid-liquid interface is less emphasised. Furthermore, thanks to the growth of modern PCs' computing potential, the fixed mesh method is becoming more and more attractive. Finer mesh simulations are no longer extremely time consuming as they once were.

On fixed mesh, the enthalpy method - being grounded in the weak solution of partial different equations - makes the simulation simpler. The interface Stefan condition is fulfilled internally. A mushy zone is generated in the vicinity of the interface to avoid the discontinuity of velocity between the two phases. This discontinuity is to blame for the numerical instability.

In the theory of the enthalpy method, the three sets of mathematical equations used to describe the different phases and interface have no distinctions anymore. They are unified under a single enthalpy equation (Eq. 1.19).

$$\frac{\partial \rho h}{\partial t} + \nabla(\rho h u) = \nabla \cdot (k \nabla T) \quad (1.19)$$

where enthalpy content h is the total enthalpy and is the function of temperature:

$$h = \int_{T_0}^{T_1} C_p dT + \lambda l(T) \quad (1.20)$$

where ρ is density and C_p is specific heat capacity, T is temperature, $l(T)$ is liquid fraction and λ is latent heat of fusion. The detailed enthalpy method is depicted in Chapter 3.

In the published papers, this enthalpy method has been applied to different phase change cases [70–76]. V. Voller and M. Cross [74] used an implicit finite difference scheme to solve the enthalpy formulation and obtain an accurate solution to phase change with a relative accuracy of 0.1%. Their algorithm is said to be able to simulate the solid-liquid phase change no matter whether the phase change occurs at a specific temperature or across a temperature range. They concluded the following advantages regarding their implementation of enthalpy method:

1. simple in concept and easy to program
2. no starting solution required
3. accurate tracking of the phase change boundary and temperature history at any point
4. easy coping with not-constant thermal properties
5. able to deal with problems involving any size phase change temperature range (including a single point) and body heating, simultaneously
6. easily extendable to multi-dimension problems

M. Costa *et al.* [77] tested the heat performances of a phase change latent heat storage system with and without fins by employing the enthalpy method with the fully implicit finite difference scheme.

Heat capacity method is the second numerical approach to simulate phase change. Its objective is to prevent the possible temperature oscillation of enthalpy method. In the heat capacity method, the latent heat effect is expressed as a finite temperature dependent specific heat which occurs over a temperature range [78]. P. Lamberg *et al.* [78] used both the enthalpy method and heat capacity method to simulate a PCM heat storage system. Those simulations were performed on FEMLAB. Experiments were also carried out to validate the numerical results. All the numerical predictions gave a good estimation of the melting and freezing processes, while the heat capacity method was more precise when compared to the experiments.

1.4 Proposition of this research

As explained, among all the possible methods to integrate the PCM into buildings, the transparent wall bricks filled with PCM can provide buildings with not only nice isolation capability and high thermal performance, but also with better lighting during the day. The transparent brick we used

to construct the Minibât in the CETHIL² has the configuration shown in Figure 1.16

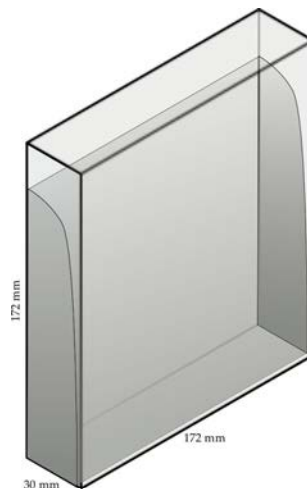


Figure 1.16 – Transparent brick (filled with PCM)

The fundamental physical phenomena occurring in the transparent PCM brick are melting and solidification. The melting and solidification are complex processes, because they possess a strong non-linear attribute. They are the blend of moving boundary, phase change and heat transfer, and in most cases, they also include the natural convection in the melted liquid phase. This natural convection could dramatically impact the heat transfer.

This dissertation is proposed grounded in the three purposes:

1. Improving the existing experimental approach

The widely chosen techniques to perform the experiments remain more or less the same. For instance, the thermocouples are largely employed to obtain the local discrete temperature information [52, 55, 79–82].

However, the natural convection in the brick during phase change is quite feeble. Even small factors could disturb it. As one of our goals is to understand the impact of natural convection on phase change, even this tiny disturbances introduced by the thermocouples are unacceptable.

Consequently, in our experiment (Chapter 2), we plan to employ a non-intrusive method to study the melting process inside the transparent brick. This chapter insists on providing us with the relevant results of melting, and on evaluating this experimental tactic.

2. Developing an efficient solver to perform the melting simulation

Although various numerical simulations have been performed through different methods. For example, the *h*-method and the *r*-method on the

2. Le Centre d'Énergétique et de Thermique de Lyon, CNRS UMR 5008

adaptive mesh; the enthalpy method and the heat capacity method on the fixed grid. They provide us to some extent quite nice results but undoubtedly suffer from unbearable long computation time and require a large amount of computer resources [61, 83, 84].

In this dissertation, we developed a solver which has higher efficiency than those published. We chose the thermal lattice Boltzmann method (TLBM) to perform the simulation: the LBM was used to solve the flow and the energy equation was used to solve the temperature distribution by finite difference scheme. Additionally, the enthalpy method was used to simulate the melting phase change. What's more, our numerical simulation was specifically designed and optimized to be executed on graphic processing unit (GPU).

3. Extending the solver to simulate the melting in the 3-dimensional condition

As for the melting in the rectangular transparent brick with two vertical isothermal sides and the adiabatic sides, the existing numerical simulations all assume that the melting is a 2-dimensional process. For this reason and maybe also that it would require a disproportionate augmentation of the demand for computational time and resources, no 3-dimensional results are actually available. However, when we increase the Ra number to a relative high value - such as $Ra > 10^8$ - this 2-dimensional assumption may not be true any more.

As a result, we extended our numerical simulation to simulate the 3-dimensional melting (Chapter 4) in order to discover the similarities and/or the differences between the 2-dimensional and the 3-dimensional simulations.

This page is left blank on purpose.

Part I

Experimental method

A scientific truth does not triumph by convincing its opponents and making them see the light, but rather because its opponents eventually die and a new generation grows up that is familiar with it.

MAX PLANCK

This page is left blank on purpose.

Chapter 2

Experimental study

This chapter presents the experiments carried out. We used a non-intrusive way to investigate the melting process inside the transparent brick: the particle image velocimetry (PIV) is used to study the natural convection in the melted liquid phase, and the laser-induced fluorescence (LIF) is used to obtain the temperature distribution. The chapter commences with the detailed explanations for the experimental apparatus (Sec. 2.3), including its configurations and the preliminary on the PIV and the LIF. After follows the experimental procedure (Sec. 2.4). The chapter then concludes with the results (Sec.2.5) and the conclusions (Sec. 2.6).

2.1 Introduction

From the literature review of the experiments on solidification and melting in section 1.3.3.1, we noticed that although many experimental researches about phase change have been published, the experimental methods still remained somewhat unchanged. Let us take the most important physical parameter - the temperature T - in heat transfer process as an example. Temperature information basically is sampled by thermocouples in modern experiment designs. The well fabricated and calibrated thermocouples can provide us with stable and precise measurements. However, in a phase change heat transfer process, there exist both heat transfer and natural convection flow, which means that implanting those thermocouples could definitely impact the real physical process.

As we know, image technologies such as the particle image velocimetry (PIV) and the laser-induced fluorescence (LIF) have become reliable non-intrusive and precise methods to investigate flow and heat transfer problems. As for the PIV, there are many application cases. For examples, Gandhi M. S. *et al.* [85] used the PIV to obtain the one and two-phase natural convection flow data, while Someya, S. *et al.* [86] used the PIV method

to inspect the natural convection of gas-liquid flow. However there are few experiments [87, 88] in which the PIV was chosen to analyse the flow during liquid-solid phase change. As for the LIF, by calibrating the photo pixel intensity, it can be used to obtain the condensation field or temperature field [89,90]. The PIV and the LIF are all non-intrusive methods, which guarantees no impacts on the flow.

Since the PIV and the LIF have such intrinsic advantages, in this experimental study, a combination of PIV and LIF was employed to inspect the liquid-solid phase change heat transfer process. The apparatus were carefully configured, because of the coexistence of solid and liquid at the same time and the low flow velocity of natural convection.

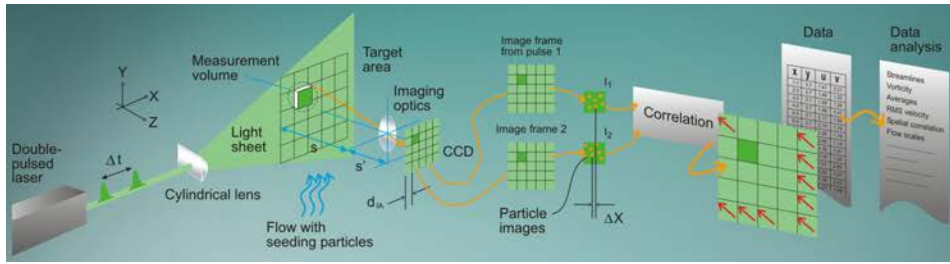
In this experimental study, the liquid-solid phase change heat transfer occurs within one transparent rectangular brick, two vertical surfaces maintaining at different but constant temperatures, referring to the temperature difference between the inside and the outside of the building; the upper and the front sides are kept uncovered to record the inner process by a camera; the bottom and the back sides were insulated and kept adiabatic. The experimental set-up will be described in section 2.3.

2.2 Experimental design

2.2.1 Study of the natural convection flow: particle image velocimetry

The particle image velocimetry (PIV) initially emerged in the early 20th century. It is an indirect and non-intrusive velocity measurement approach. The distinct characteristic of PIV is that it allows to record a large area of flow field and obtain the relevant velocity informations. This is different from the Doppler Global Velocimetry (DGV or called Planar Doppler Velocimetry) which is suitable for high speed flow and Molecular Tagging Velocimetry (MTV) which is to measure a single point in a flow field. The PIV has also a large spacial resolution but a relative small temporal resolution -due to the technological restrictions of high speed camera and high speed laser - whereas the MTV and DGV have very high temporal resolution.

The PIV is now widely used to obtain the large domain flow information. Raffel M. *et al.* [91] gave a thorough introduction about PIV. A typical modern PIV system is shown in Figure 2.1. In a PIV system, the flow of interest is mixed with small particles - known as tracer particles. For some liquids which already have particles as part of their component, there is no need for extra particles. An incident luminous light sheet goes through the flow region and thus lights up the particles in the flow. Usually, the light source is provided by a laser generator. The sheet of flow is illuminated at least twice between a short time intervals, this time interval is a very

Figure 2.1 – Diagram of a modern PIV system ^a

a. Source: <http://www.dantecdynamics.com>

critical parameter that is determined by the mean flow velocity and the pixel resolution of camera. At each time of illumination, the tracer particles within the lit up flow sheets scatter light and their images are recorded by a CCD or CMOS camera. It is assumed that, if the appropriate tracer particles have been chosen, the displacements of those tracer particles follow the actual flow homogeneously with a negligible lagging behind. This means that the flow status can be visualized by displacements of particles. The velocity vector is as simple as equation 2.1:

$$\mathbf{V} = \frac{\Delta \mathbf{X}}{\Delta t} \quad (2.1)$$

The $\Delta \mathbf{X}$ and Δt respectively are the particles displacements and time intervals between light illuminations.

Each of the captured images of tracer particles in a time sequence is divided into smaller "interrogation areas". For each interrogation area, a velocity vector can be derived by statical methods - such as auto-correlation and cross-correlation - by taking into considerations the time interval between two lighting-ups and the magnification of the images. After calculating each interrogation area, the entire flow velocity information is obtained.

To successfully perform a PIV experiment, there are several points needed to be considered.

2.2.1.1 Tracer particles

The entire PIV system is based on the images of tracer particles, which means No seeding particles, No velocity information; Bad seeding particles images, Bad velocity results. The essential considerations about the tracer particles are their ability to follow a flow field (fluid mechanical properties), their ability to scatter incident light (optical properties), their density and distribution in the flow field of interest. Those three aspects are controlled by the particles density and size and by the seeding method.

2.2.1.1.1 Particle density and size If a type of particles in the flow field cannot faithfully follow the actual flow, it cannot be a good candidate for the PIV experiments. Generally speaking, small particles follow the flow field better and have short response time than bigger particles. The principal impact introduced on particles' ability to follow the flow is from the gravitational force. For a spherical particle (density: ρ_p , diameter: d_p) depositing in a still viscous fluid (density: ρ) at a low Reynolds number, its depositing velocity (\mathbf{u}_g) caused by the gravitational force is described by Stokes' drag law,

$$\mathbf{u}_g = d_p^2 \frac{(\rho_p - \rho)}{18\mu} \mathbf{g} \quad (2.2)$$

where μ is the dynamic viscosity of fluid.

Thus, in a fluid with an accelerating rate (\mathbf{a}), the velocity lag (\mathbf{u}_s) of a particle is estimated by the Eq. 2.3.

$$\mathbf{u}_s = \mathbf{u}_p - \mathbf{u} = d_p^2 \frac{(\rho_p - \rho)}{18\mu} \mathbf{a} \quad (2.3)$$

where \mathbf{u}_p is the particle velocity and \mathbf{u} is the flow velocity. If the particle density is much bigger than the fluid density ($\rho_p \gg \rho$), the particle velocity has an exponential relation with fluid velocity as a function of time.

$$\mathbf{u}_p(t) = \mathbf{u} \left[1 - \exp\left(-\frac{t}{\tau_s}\right) \right] \quad (2.4)$$

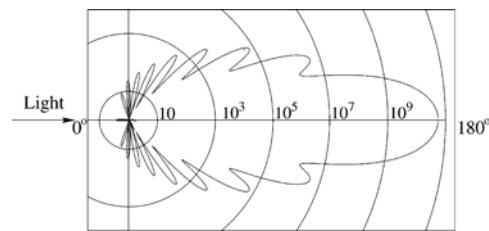
and the relaxation time (τ_s) is

$$\tau_s = d_p^2 \frac{\rho_p}{18\mu} \quad (2.5)$$

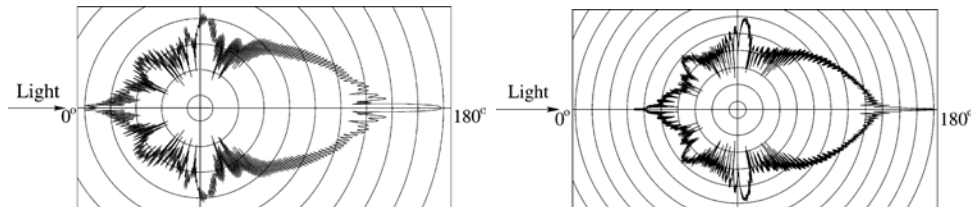
Although those equations are derived from a spherical particle in a low Reynolds flow and the flow acceleration rate is constant, for many practical cases, those equations are not as simple as Eq. 2.3 and Eq. 2.4. However, the relaxation time (τ_s) is still a practical parameter to assess the particles' ability to follow the fluid flow field.

From Eq. 2.3, we could notice that, in order to minimize the velocity discrepancy between the particle velocity and the flow velocity, the particle density should be close to that of the fluid. Fortunately, for liquid flow cases, it is not difficult to find the particles with approximate density. In our experiment, the PCM (n-octadecane) is a liquid with a density around 0.8 g/cm^3 .

Additionally, we can see from Eq. 2.3 that, decreasing the size of particles is also a way to minimize the velocity discrepancy. Smaller particles are more sensible to flow. However the size of the particles can impact their ability to scatter the light. Bigger particles have better ability to scatter light



(a) Light scattering by a 1 μm glass particle in water.



(b) Light scattering by a 10 μm glass particle in water. (c) Light scattering by a 30 μm glass particle in water.

Figure 2.2 – Polar distribution of the scattered light intensity of different particles sizes [92]

than smaller particles. This limits the possibility by forbidding the use of extreme particles. For a practical case, the particles size is a compromise of those two considerations.

The final images' quality (luminosity and contrast) largely depend on the tracer particles. In general, the light scattered by particles depends on the ratio of the reflective index of particles to that of the liquid, the particles' size, shape and orientation, as well as the incident light polarization and the observation angle [92]. In order to improve the images quality, it is more convenient and effective to properly choose the tracer particles than to increase the incident light intensity.

Figure 2.2 shows the typical polar distribution diagrams of the scattered light intensity of different particles sizes in water. They clearly show that particles of larger size scatter more incident light than smaller ones. In addition, the particles scatter light almost in every direction, which means the particles not only scatter the incident light but also the light from the other particles' reflections. One conclusion from these diagrams is that, apart from the method of increasing the size of particles, it is also possible to increase the scattering efficiency by increasing the particles' distribution density, despite the fact that this latter method is prone to increase the images noise.

2.2.1.1.2 Particles' seeding In our experiment, the flow of interest happens in liquid phase. Fortunately, the seeding of particles into liquid flow field

is quite straightforward. Seeding is done by adding the tracer particles into the PCM and mixing till the particles distribute homogeneously in the PCM liquid. In our study, we tried two different types of particles, one type is commercial particles and another type is the particles naturally introduced by the laser-induced fluorescence experiment. This will be depicted in the next section. Typical tracer particles for liquid media are listed in [Table 2.1](#).

Table 2.1 – Typical tracer particles for liquid flows [92]

Type	Material	Mean diameter (μm)
Solid	Polystyrene	10-100
	Aluminium flakes	2-7
	Hollow glass spheres	10-100
	Granules for synthetic coatings	10-500
Liquid	Different oils droplets	50-500
Gaseous	Oxygen bubbles	50-1000

2.2.1.2 Image recording

The images recording technologies have two different categories, which refer to the *single frame/multiple-exposures* technologies (see [Figure 2.3](#)) and *multiple-frame/single exposure* technologies (see [Figure 2.4](#)).

The single frame/multiple-exposures technologies record the particles images at different light flash on a same frame. This obviously has an ambiguous particle moving directions. This type of technologies was widely used in the photographic epoch, when the media to record images was the film. Since the ambiguity of the particles' displacement directions, some complimentary methods are necessary to solve this ambiguity, for instance, images shifting, pulse tagging or colour coding.

The multiple-frames/single exposure technologies however keep the temporal information of each image. This removes the directional ambiguity occurring in the single frame/multiple-exposures technologies. As the digital capture equipments -such as CCD/CMOS camera - are becoming more and more common and less expensive, the multiple-frames/single exposure is now the preferred choice for a PIV experiment.

2.2.1.3 PIV processing procedures

To extract the velocity information from the raw PIV particles images, three basic procedures are suggested: 1. Image signal enhancement, more specifically referring to image preprocessing, 2. PIV processing, 3. Vectors post-processing. The second set is the most important step and can not be

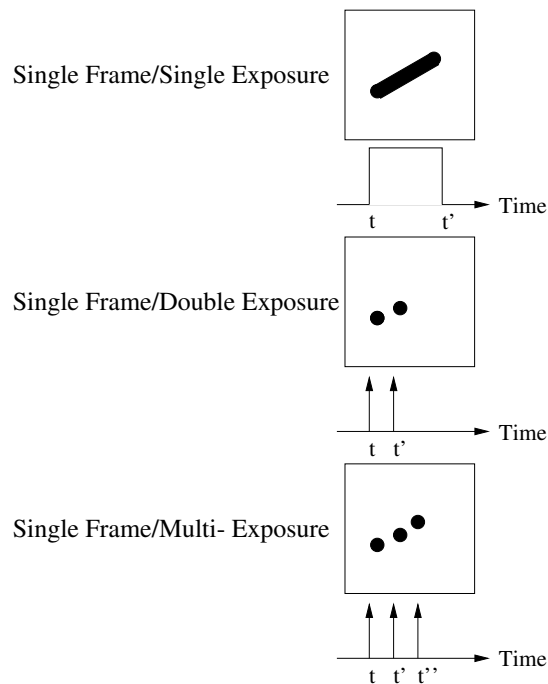


Figure 2.3 – Single frame technologies [93]

omitted, whereas the other two are optional according to the raw images' qualities even if strongly recommended.

2.2.1.3.1 Image preprocessing This step is not mandatory for a PIV implementation. Nevertheless, since for most realistic PIV experiments, the raw images usually do not have excellent qualities, in fact, many factors can exert influences. For example, the light sheet's non-uniformities and the variations of intensity of each light burst can cause the output images intensities to fluctuate. Besides, the irregular shapes and sizes of tracer particles provide a non-homogeneous scattering light. The out-of-plane movements of tracer particles can also cause these particles' information to get lost in the final output images. All of those potential influences on the output PIV images can be partially eliminated by image preprocessing. We must note however that the negative influence of image preprocessing is that it can change the images' pixel statical information and introduce a relatively high uncertainty.

⇒ **Background subtraction.** Background subtraction is the most important and effective step to pre-process a raw PIV image. Each image captured is a combination of the particle information with background noise. The particles information that we need is transient. Those particles do not stay in the same positions in temporal images sequences

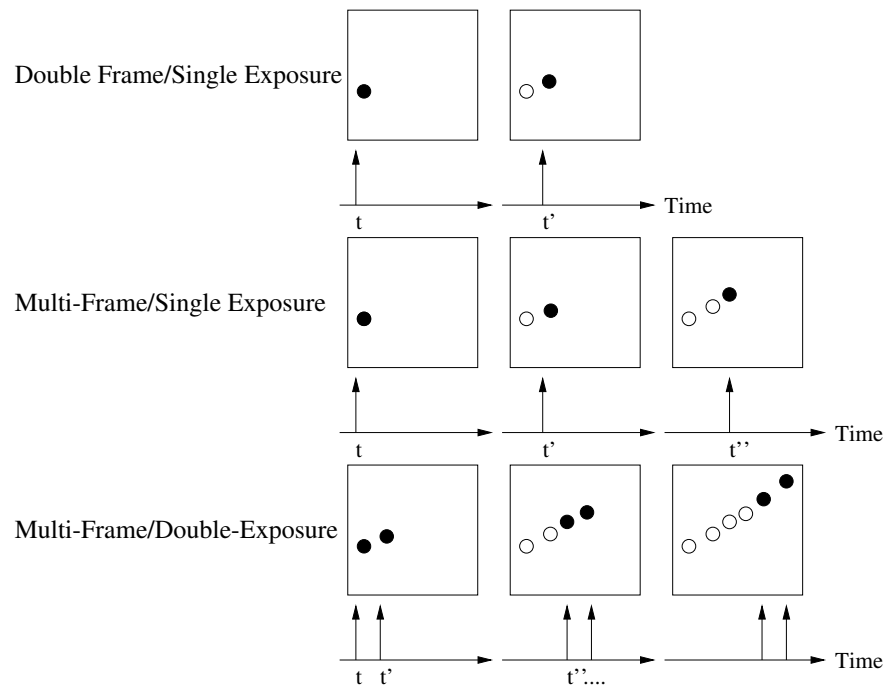


Figure 2.4 – Multiple frame technologies [93]

whereas the stationary objects in the flow field remain still and their images compose the background noise. As a result, subtracting this background can largely improve the image quality. To successfully obtain the background noise signal and remove it, we can take a photo of the flow with no tracer particles introduced, and use this photo as a reference. However, from time to time this particle-free image is quite impossible to obtain, whereas we can use a batch of images to calculate the average minimum intensity which can be used to subtract the background noise.

- ⇒ **Image binarization.** Since brighter particles can hide the information included in weaker particles, if some parts of the flow are considerably brighter than the others, the flow information in the dark part get lost, this step is employed to normalize the particles intensities.
- ⇒ **Intensity capping, dynamic histogram stretching and min/max filter.** All of them are use to do normalize the image contrast.

2.2.1.3.2 PIV processing For a preprocessed PIV image, to extract the velocity information from the particles usually needs statical methods, such as auto-correlation for single frame/multiple-exposure and cross-correlation for multiple-frame/single exposure. Because the state-of-the-art image recording technologies mostly use multiple-frame/single exposure approach, the

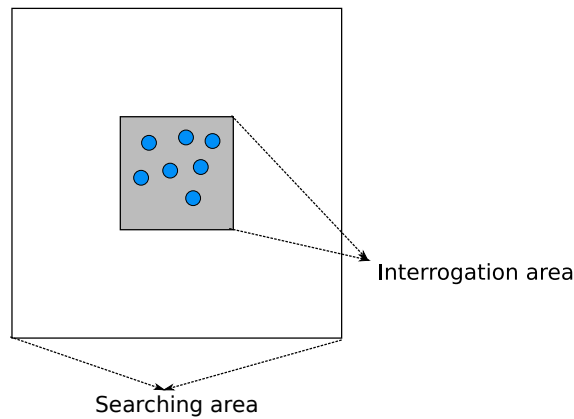


Figure 2.5 – Interrogation area in the first frame and searching areas in the second frame

cross-correlation will be illustrated in this section.

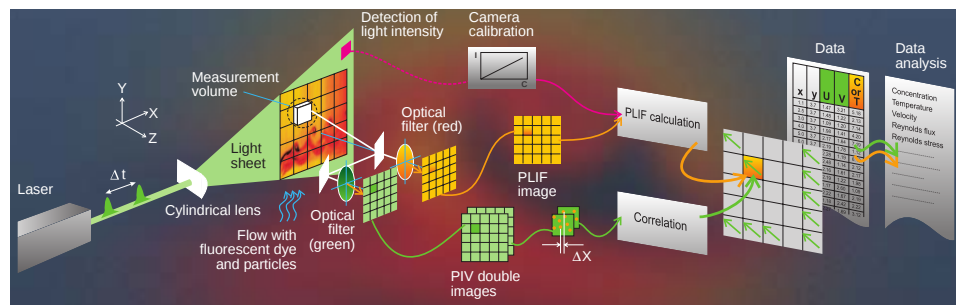
Before performing cross-correlation, two successive images (two single exposed frames) compose an image pair. Single particle' images look alike, so it is impossible to trace a single particle image to determine its displacement. Instead, the first image of the image pair is divided into many small regions known as *interrogation areas* and the second image of this image pair is divided into *searching areas* (see Figure 2.5). The cross-correlations are performed on those small interrogation areas one by one to get the velocity field.

The image intensity at position (x, y) is defined as $I_i(x, y)$, where $i = 1$ or 2 refers to the two frames used to do cross-correlation. The cross-correlation multiplies the image intensities in the interrogation areas and adds them together, as shown in Eq. 2.6. This sum R_{I_1, I_2} must have a peak value at position (x, y) . From this (x, y) value, we could obtain the mean displacement of the particles in the interrogation area.

$$R_{I_1, I_2}(\Delta x, \Delta y) = \sum_x \sum_y I_1(x, y) I_2(x + \Delta x, y + \Delta y) \quad (2.6)$$

2.2.1.3.3 Vectors post-processing After evaluating each interrogation area by doing cross-correlations, the final velocity vectors are derived. However, in this vector results, there are usually some vectors which are incorrect according to basic physical analysis. They are false vectors, and usually keeping those false vectors in the cross-correlation iterations can cause this error propagate to a considerably large scale, resulting in the failure of cross-correlation and the high uncertainty. Consequently, false vectors must be removed between each iteration and in the final output.

There are two ways to identify the false vectors:

Figure 2.6 – Diagram of combined LIF and PIV test^a

a. Source: <http://www.dantecdynamics.com/>

- ⇒ If expected flow velocity range is known, false vectors can be identified by comparing the standard deviations to the mean.
- ⇒ False vectors can also be purged away by comparing their values with those of their neighbours.

After removing the false vectors, we must use interpolation and data smoothing to fill those removed vectors and get a vector field with good quality.

2.2.2 Study of the temperature distribution: laser-induced fluorescence

As a non-intrusive method, the PIV has been successfully applied to various situations to obtain the information on the flow velocity since its invention. In contrast, the non-intrusive methods for temperature measurement are not as mature as the PIV. One of those methods is the laser-induced fluorescence (LIF) which is a relative new flow visualization approach to obtain the quantity of concentration and/or temperature. In our study, we are only concerned about the temperature measurement. A typical diagram of the LIF temperature test combined with the PIV is shown in Figure 2.6.

2.2.2.1 Theory of the LIF

Fluorescence induced by exciting light is a macro physical phenomenon linked to the energy transition on the atom and molecule level. The laser is commonly chosen as exciting light. For some special substances - called fluorescent substances - when incident laser goes through, the molecules and/or atoms will absorb the photon energy. This absorption causes the molecules' and/or atoms' energy to transit from the ground level to the excited level(s). The emission (fluorescence) occurs spontaneously and right

after the energy transition from the ground level to the excited level, resulting in the energy level falling back again to its initial ground level. Depending on the photon energy absorbed by fluorescent substances, the molecules and atoms can jump to different excited levels. For the sake of simplicity, we consider a two-level energy transition, from ground level 1 to excited level 2. The fluorescence intensity (I) is described in following Eq. 2.7 [94]:

$$I \propto A_{21} \cdot \nu_{21} \cdot l \cdot N_0^1 \cdot I_{\text{laser}} \cdot \frac{B_{12}}{A_{21} + Q_{21}} \quad (2.7)$$

where

- A_{21} and B_{12} are the Einstein coefficients for spontaneous emission and absorption, respectively.
- ν_{21} is the frequency of the emitted fluorescence photons,
- l is the measurement volume length,
- N_0^1 is the initial ground state population number density of the species probed,
- I_{laser} is the laser intensity,
- Q_{21} is the quenching rate.

The quenching rate Q_{21} is temperature, pressure and composition dependent. This is the physical basis on which the LIF temperature measurement is possible.

As for a specific application, the Eq. 2.7 is written in its appropriate form in order to embody the relevant physical characteristics. In the liquid temperature measurement, the fluorescence intensity is Eq. 2.8 [94, 95]:

$$I = I_0 \cdot C \cdot \phi(\lambda, T) \cdot \epsilon(\lambda, T) \quad (2.8)$$

where

- I_0 is the incident laser intensity,
- C is the concentration of the fluorescent substance in the liquid of interest,
- ϕ is the quantum efficiency or quantum yield, depending on the wavelength λ and temperature T ,
- ϵ is absorption coefficient, also a function of wavelength λ and temperature T

The wavelength λ and concentration C are both easy to maintain. Both ϕ and ϵ are the function of temperature, and because of

$$\frac{d}{dT}\epsilon \ll \frac{d}{dT}\phi \quad (2.9)$$

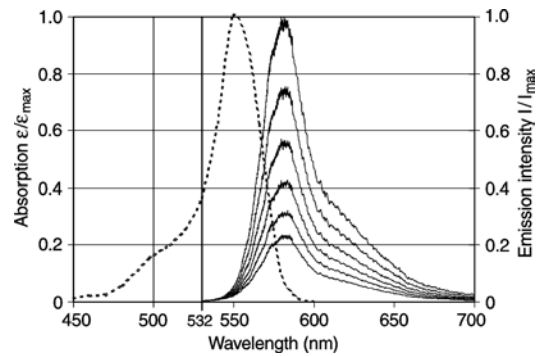


Fig. 1. Absorption (—) from López Arbeloa (1981) and emission (—) spectra of rhodamine B for 20, 30, 40, 50, 60 and 70°C

Figure 2.7 – The spectrum characteristics of Rhodamine B [89]

so the ϵ is judged temperature independent. Consequently, the fluorescence intensity I is simply a function of temperature T and incident laser intensity I_0 . The basic idea of LIF for temperature measurement is grounded in such relation: $I = I(T, I_0)$.

The incident laser intensity I_0 can be influenced by various factors, for example, the reflection inside the flow; the intensity decreasing when the laser goes through the fluid *etc.* This variation of the incident laser intensity can be reduced by well designing of the experiment's set up or by introducing a so-called two-color LIF method [96].

2.2.2.2 Spectra characteristics

Just as the tracer particles in the PIV, in order to perform the LIF measurement, an appropriate fluorescent dye must be introduced into the system. Furthermore, the fluorescence should have a different wavelength from that of the incident laser in order to successfully capture the emission fluorescence by camera without the impact from the incident laser light.

In our experiment, the Nd-YAG laser is used as the light source, because of its high single emission power and also because its output wavelength (532 nm) is approximate the optimum value of absorption of Rhodamine B. The Rhodamine B is used as fluorescent dye because of those reasons and because it has a nice temperature sensitivity ($dI/dT \cdot I^{-1} \approx 0.023\text{K}^{-1}$). The absorption and emission spectrum is shown in Figure 2.7. From Figure 2.7 we can see the optimum absorption wavelength is around 550 nm and the emission wavelength is shift from the absorption wavelength.

2.2.2.3 Error sources

Image processing Like the PIV tests, the images sampled for the LIF also need to be processed for the purpose of the errors reduction and the correlation. The background subtraction is always a straightforward and effective way to avoid the noise signal introduced by the background.

Error source The possible error sources are summarized in [Table 2.2](#).

Table 2.2 – Possible error sources for LIF (extracted from [97, 98])

Category	Source
Dye	Fluorescence from background dye
	Fluorescence sensitivity to pH and temperature
	Fluorescence saturation (strong excitation)
	Photo-bleaching
Excitation light	Spatial variation in light sheet (optics, etc.)
	Laser attenuation due to background dye
	Laser attenuation due to instantaneous dye
	Shot-to-shot laser power variation
Optics	Refraction through walls or interfaces
	Lens vignette
CCD camera	Pixel-to-pixel offsets (dark response)
	Pixel-to-pixel gain variations

One must realize that not all the error sources listed in [Table 2.2](#) could occur concurrently in a specific practical application. To some extent, those errors could be attenuated by better configuring the experimental apparatus or by mathematical treatments.

2.3 Experimental setup

The ensemble of apparatus consists of four different functional units. They are:

1. transparent brick filled with PCM;
2. heat exchangers driven by water pump;
3. heat flux and temperature signal receiving and processing unit;
4. images capture and analysis unit.

The main subject of interest is the transparent brick filled with the PCM undergoing melting/solidification. The heat water pumps are used to provide the isothermal temperatures. The heat flux and temperature sensors and their signal receiving and processing unit are used to get the heat flux

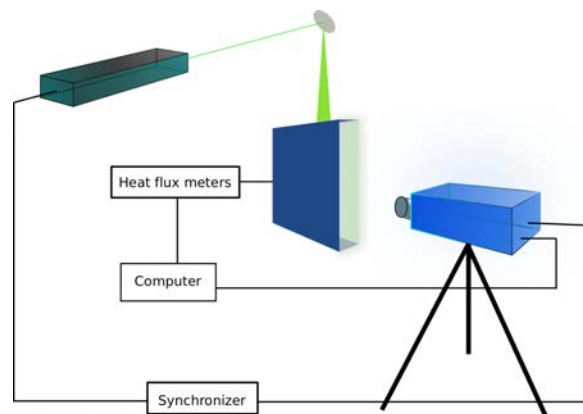


Figure 2.8 – Experimental equipments

and temperature information during the experimental procedure. Finally, the PIV and LIF information are retrieved from our images capture and analysis unit. A diagram is shown in Figure 2.8, please note that the heat pump is not illustrated.

2.3.1 The PCM-Rhodamine mixture

In this experimental study, n-octadecane with 99% purity is chosen as the PCM. First, it has a good transparent property that is very suitable when using photo technologies to inspect the inside flow phenomena. Second, its melting point is around 28°C , which is very close to the environmental temperature fluctuation range, and thereby very suitable for heat charge and discharge under normal environment. The properties of n-octadecane are shown in Table 2.3.

Table 2.3 – Thermophysical properties of n-octadecane [69]

Property	Value
Melting temperature T_f	$28.0[^{\circ}\text{C}]$
Latent heat λ	$1.25 \times 10^5[\text{J}/\text{kg}]$
Specific heat C_p	$1250[\text{J}/(\text{kg} \cdot ^{\circ}\text{C})]$
Thermal conductivity k	$0.2[\text{W}/(\text{m} \cdot \text{K})]$
Density ρ	$800[\text{kg}/\text{m}^3]$
Kinematic viscosity ν	$1 \times 10^{-5}[\text{m}^2/\text{s}]$
Thermal expansion coefficient β	$0.002[\text{K}^{-1}]$

As said in the first section, the tracer particles and fluorescent dye play the most critical roles in the PIV and the LIF experiments respectively. At the testing stage of our experiment, we tried to employ a commercial tracer particles for the PIV. They are Polyamid particles from Dantec company,

which the detailed specifications are shown in Table 2.4. This type of seeding particles is widely used for water flow since its density is close to that of water (1.03 g/cm^3 versus 1 g/cm^3).

Table 2.4 – The specifications of Polyamide seeding particles

	Polyamide seeding particles	Fluorescent polymer particles
Particles shape	non-spherical but round	spherical
Mean particle size	$20 \mu\text{m}$	$10 \mu\text{m}$
Size distribution	$5 - 35 \mu\text{m}$	$1 - 20 \mu\text{m}$
Density	1.03 g/cm^3	1.19 g/cm^3
Melting point	$175 \text{ }^\circ\text{C}$	$125 \text{ }^\circ\text{C}$
Refractive index	1.5	1.479
Material	Polyamide 12	Methyl methacrylate Labeled with Rhodium B

The fluorescent dye we used is Rhodamine B, because of its high sensitivity to temperature variations ($dI/dT \cdot I^{-1} \approx 0.023\text{K}^{-1}$).

Although it is reasonable to use the Polyamide seeding particles and Rhodamine B together, however, when the experiments are actually performed, some problems arose. First, the density of the n-octadecane we used as the PCM is much smaller than that of the Polyamide seeding particles with a density around 0.8 g/cm^3 . In addition, the natural convection is feeble and the melting process lasts several hours under the given temperature range, making the Polyamide seeding particles are prone to deposit. The worse situation is that there is almost no particles left in the flow at the end stage of the experiment. Second, the Polyamide seeding particles reflect the visible laser light, whose wavelength differs from the fluorescence of Rhodamine B. Consequently, two cameras are mandatory, which increases the complexity of the entire system. In order to solve these problems, we have prepared the PCM-Rhodamine B mixture in a different way, so that the Polyamide seeding particles can actually be excluded.

The procedure is as follows:

- ⇒ The pure n-octadecane is transparent. We fill liquid n-octadecane in a beaker and put it on a magnetic stirrer. This magnetic stirrer is equipped with a hot plate which can maintain a temperature higher than the melting point of n-octadecane to maintain it in liquid phase. Then Rhodamine B is added into the n-octadecane liquid by several doses until the n-octadecane is saturated. Continuing the mixing process for several hours makes sure the n-octadecane and Rhodamine B mixture reaches a stable state.
- ⇒ Once it has been done, one must keep this mixture still for several hours



Figure 2.9 – The mixture of n-octadecane and Rhodamine B (in liquid phase)

to let the big Rhodamine B particles deposit, and then filter this mixture by very fine filter papers in order to remove the big unsolved Rhodamine B granules. This process must be repeated until there is no visible big Rhodamine B granules remaining on the filter papers.

This pretreatment of n-octadecane is simple but very effective. Because after this pretreatment, the Rhodamine acts as both tracer particles for PIV and fluorescent dye for LIF. The final n-octadecane Rhodamine B mixture is shown in [Figure 2.9](#).

2.3.2 Transparent brick and water pump heat exchanger

The transparent brick here was made of Plexiglas and had the same dimensions as the one used in the CETHIL¹ to build the Minibât. It is filled with n-octadecane. The diagram and dimensions of the brick are shown in [Figure 2.10](#) and [Figure 2.11](#).

In order to apply the boundary temperatures, the two vertical side walls were replaced with two heat exchangers (see [Figure 2.12](#)), which use water as circulating heat liquid heated and pumped by two HAAKE Phoenix II P1-C50P Refrigerated Bath by Thermo Scientific (see [Table 2.5](#)).

Table 2.5 – Specifications of Refrigerated Bath

Bath volume	max. 8 L
Cooling capacity at 20 °C	850 W
Heater capacity 230 V	2 kW
Temperature accuracy	±0.01 °C
Working temperature range	−50 to 150 °C

We connected the baths to the heat exchangers using 8 three-way valves in order to control the heat exchanger temperature more efficiently. Four

1. Le Centre d'Énergétique et de Thermique de Lyon, CNRS UMR 5008

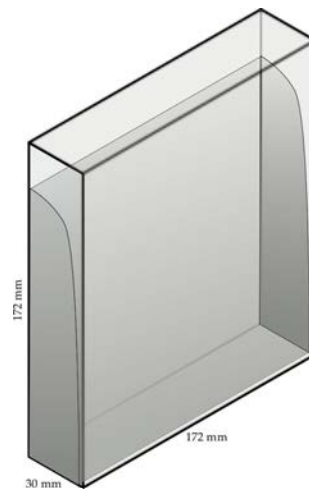


Figure 2.10 – Transparent brick (with n-octadecane inside)

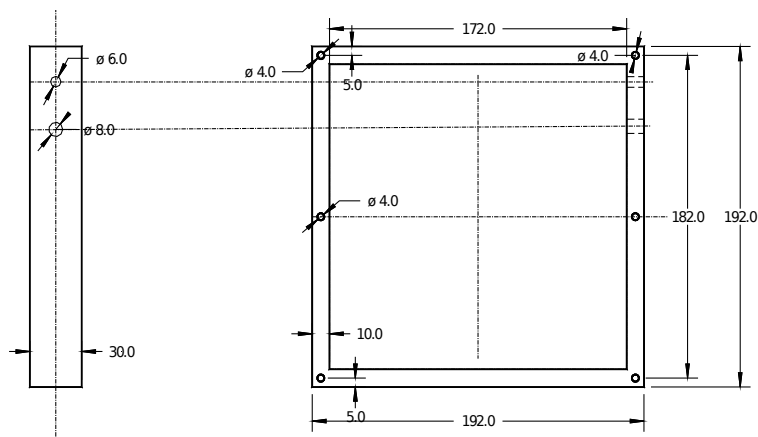


Figure 2.11 – The design dimensions of the brick (unit: mm)

K type thermocouples were fixed in the inlets and outlets of the water heat exchanger in order to monitor the temperature.

The inner surfaces which contact the n-octadecane are two aluminium plates embedded with thermocouples to monitor the temperatures applied. Their dimensions are shown in Figure 2.13.

In order to measure the heat flux through the heat exchanger to n-octadecane, the heat flux meters are integrated between the heat exchangers and the aluminium plates, forming a sandwich-like layers.

2.3.3 Heat flux meters and thermocouples

In this experiment, two heat flux meters were installed between the heat exchanger and aluminium plates. Several thermocouples were used

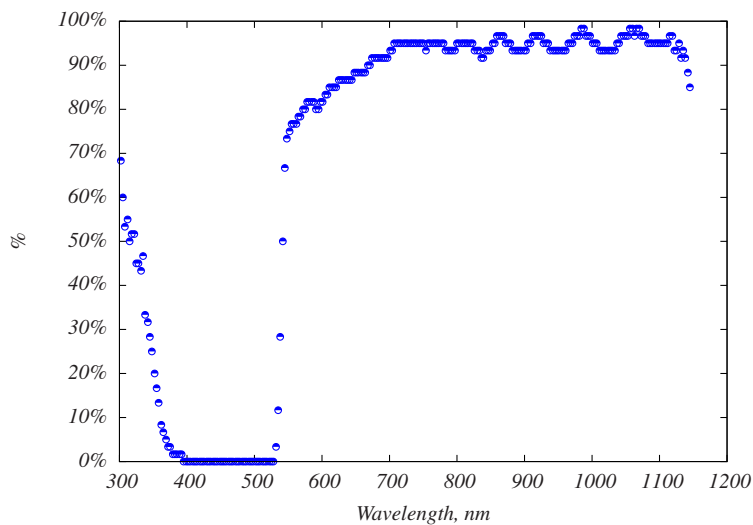


Figure 2.14 – Pass percentage of different wavelength of the filter

The thermocouples' positions on the aluminium plates is shown in [Figure 2.13](#). The thermocouples and heat flux meters were calibrated before being employed, and the signals were sampled and analysed automatically by Ni-DAQmx models and LabView with a time step of 1000 ms.

2.3.4 Image capture and analysis unit

2.3.4.1 Camera and filter

The pretreated n-octadecane and Rhodamine B mixture has two major advantages. First, since rhodamine B acts as both tracer particles and fluorescent dye, the fluorescence can be utilized for tracing the natural convection flow during the phase change and for identifying the temperature distribution. Second, only one camera was needed, because we could use a special yellow filter before camera lens, which blocked the light with wavelength smaller than 535 nm (see [Figure 2.14](#)), and hid the reflection of the laser light (wavelength 532 nm) inside the brick. As a result, the images quality was improved.

The camera used here is Imager intense from LaVision, equipped with a Nikon 50 mm fixed-focused lens with $1.8 \leq f \leq 22$. The specifications of the camera are shown in [Table 2.6](#).

2.3.4.2 Laser

A Nd-YAG laser is employed to provide the light source (see [Table 2.7](#)). The output laser is a beam that can not be used directly to illuminate the

Table 2.6 – Camera (model: Imager intense) specifications

resolution	1376 × 1040 pixel
frame rate	10 Hz
pixel size	6.45 × 6.45 μm
min. time interval	500 ns
digital output	12 bit
Distance (Lens and CCD-Chip)	46.5 mm

Table 2.7 – laser specifications

Max. output	400 mJ
Pulse duration	4 ns
Wavelength	532 nm

flow, so a series of optical lenses are used to obtain a laser sheet (see [Figure 2.15](#)).

2.4 Experimental procedure

2.4.1 The LIF calibration

After the pre-treatment of the n-octadecane and before the actual experiment, the LIF measurement must be calibrated. Due to the presence of liquid and solid, the incident laser power attenuates along the height of



Figure 2.15 – The lenses to expand the laser beam to a sheet

the brick, which caused the different intensities of fluorescence even under the same laser power. However, for simplicity, this attenuation of incident laser inside the brick was neglected. The fluorescence intensity is described in Eq. 2.8. During an experiment the concentration of Rhodamine B keeps constant, and the incident laser intensity varies within a negligible scale, so the fluorescence intensity only depends on temperature. The relation between the temperature and fluorescence intensity is calibrated through the following steps:

1. Filling in the brick with the pretreated n-octadecane mixture;
2. Maintaining the two heat exchangers at an identical stable temperature ($T_1 > T_f$) until the temperature of n-octadecane reaches the same value (normally this requires several hours);
3. measuring the fluorescence intensity;
4. increasing the temperature of the two heat exchangers to a new value (e.g. $T_2 = T_1 + 5^\circ\text{C}$) and repeating the steps 2 and 3;
5. repeating steps 2, 3 and 4 another three times to obtain the different fluorescence intensities at different temperatures (from T_1 to T_5).

The mathematical relation is then calculated automatically in the DaVis application from LaVision based on the temperatures and fluorescence intensities just measured. Be aware that if changing the PCM mixture or the laser output power, a new calibration needs to be performed again.

2.4.2 Experiment steps and configuration

The boundary condition and initial condition are shown in Figure 2.16. After calibrating the temperature-fluorescence, the measurement of melting is carried out as the following steps:

- ⇒ Filling the brick with n-octadecane with a free space of 22 mm height at the top of the brick in order to offer enough space for the PCM expansion;
- ⇒ Setting the heat exchangers temperatures to 27.8°C , slightly lower than its melting temperature. Under this temperature the PCM can become solid at a low speed, which can reduce the non-uniform crystal structures and the air stored in the PCM when solidifying. Both the crystal structures and the air bubbles can strongly deteriorate the image quality during the analysis of experimental images;
- ⇒ Adding a small amount of PCM to fill in the V shape that has formed on the upper part of the PCM when solidifying, in order to make the upper surface become flat again.

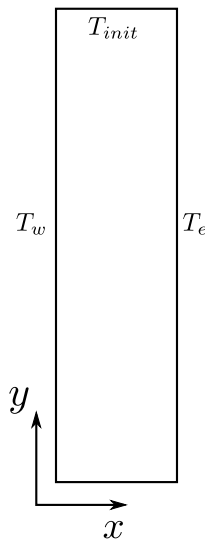


Figure 2.16 – Boundary and initial conditions. $T_w = T_{init} = 27.8^\circ\text{C}$, $T_e = 35^\circ\text{C}$, under this configuration, the $Ra = 2.48 \times 10^8$.

- ⇒ Maintaining the temperature for 12 hours, and checking the thermocouples to make sure that the entire PCM has a uniform temperature, and the heat flux meter gives a 0 value.
- ⇒ Rising one heat exchanger temperature to a set value - 35°C in this experiment -, initiating the temperature and heat flux sampling, and starting the camera and laser in order to capture the images.

The nature convection inside the brick is of order 10^{-3} to 10^{-4} m/s. The particles diameters are smaller than $125\ \mu\text{m}$. The lens focus is 50 mm. The camera resolution is 1376×1040 . After a simple calculation, the time between two frames should be around 353.7 ms. Detailed configuration is shown in [Table 2.8](#).

Table 2.8 – Configuration for experiment setup under the laser light wavelength 532 nm and a desired pixel displacement of 16 pixels

Working distance	816 mm
f# of lens	1.8
Focal depth	2.77 mm
Time intervals between two frames	353.7 ms

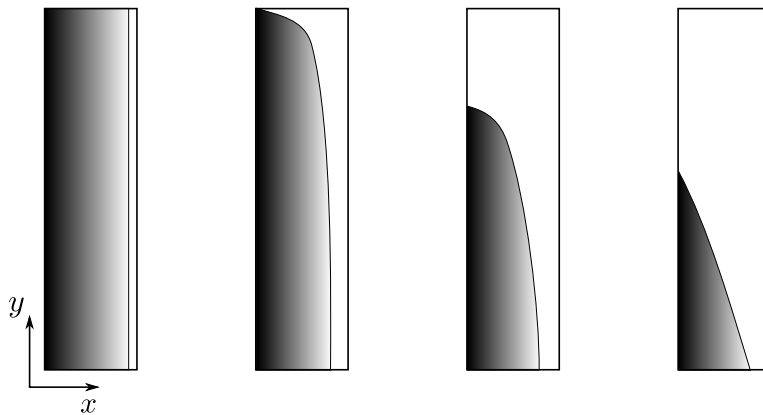


Figure 2.17 – The four melting stages of the solid-liquid interface

2.5 Results

2.5.1 Melting process²

The Ra number and Pr number in this experiment are 2.48×10^8 and 50 respectively. In this study, the entire melting process of the interface is identified as four stages (shown in Figure 2.17).

- ⇒ The first stage goes from the beginning of melting to the end of pure conduction. In this stage, the heat is transferred only by conduction. The cavity of liquid is very slim and the liquid-solid interface is parallel to the hot wall;
- ⇒ The second stage goes from the beginning of natural convection till the interface reaches the cold wall at the upper part;
- ⇒ The third stage happens when the interface changes its initial curve shape to the linear shape;
- ⇒ The last stage sees the shrinking of solid with a linear interface.

2.5.2 Liquid-solid interface evolution

Figure 2.18 shows the liquid solid interface evolution with time before it contacts the cold wall. Those curves are almost overlapped at the initial stage of melting and they are all almost linear but with different slopes. The PCM melts faster when y_i is bigger. The corresponding value of y_i is shown in Table 2.9. From the gradient, we could obtain the interface moving velocity of different positions along the interface (see Figure 2.19).

2. Click [here](#) to access a video of melting of this experiment

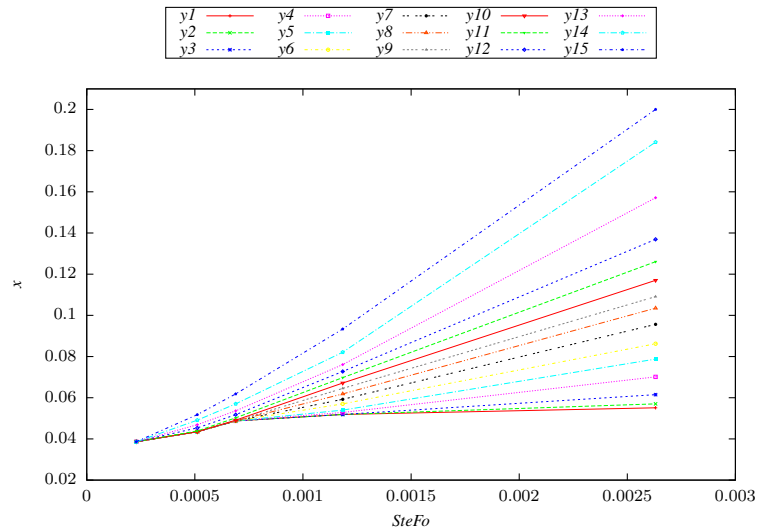


Figure 2.18 – The interface evolution at different heights

Table 2.9 – Reference points for the evolution of interface (dimensionless form)

y_1	y_2	y_3	y_4
0.0073	0.0570	0.1067	0.1564
y_5	y_6	y_7	y_8
0.2061	0.2558	0.3055	0.3552
y_9	y_{10}	y_{11}	y_{12}
0.4050	0.4547	0.5044	0.5541
y_{13}	y_{14}	y_{15}	
0.6037	0.6535	0.7032	

The melting velocities at each y are almost constant. However, at the higher part of the brick, due to the existence of natural convection, the PCM melts far faster than its the lower counterpart (more than 7 times faster). This curve has a maximum of curvature which is close to $y = 0.55$. The typical melting images are shown in [Figure 2.20](#).

2.5.3 Velocity field

During the melting process, the lower part of the melted flow cavity is very narrow. As a result, this narrow cavity is not bright enough to obtain the flow and temperature information by the PIV and LIF. Consequently, only the velocity fields of the upper part of the brick are demonstrated. A typical velocity field is shown in [Figure 2.21](#).

[Figure 2.22](#) and [Figure 2.23](#) show the velocity contours at two different

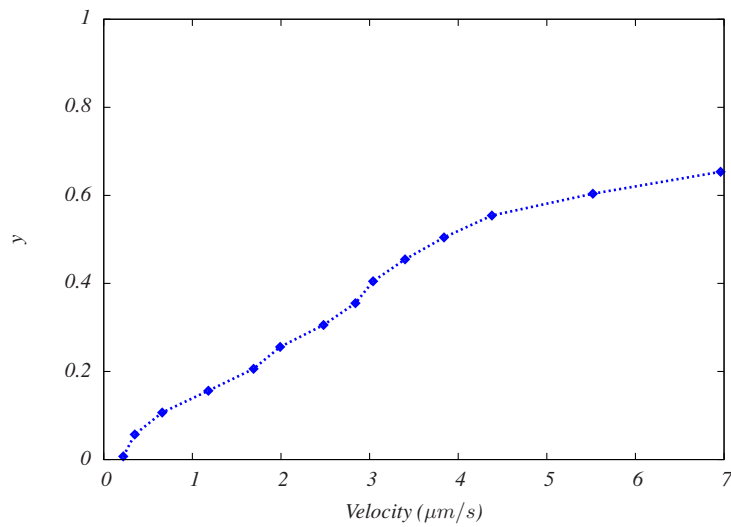


Figure 2.19 – Melting velocity of the interface at different γ

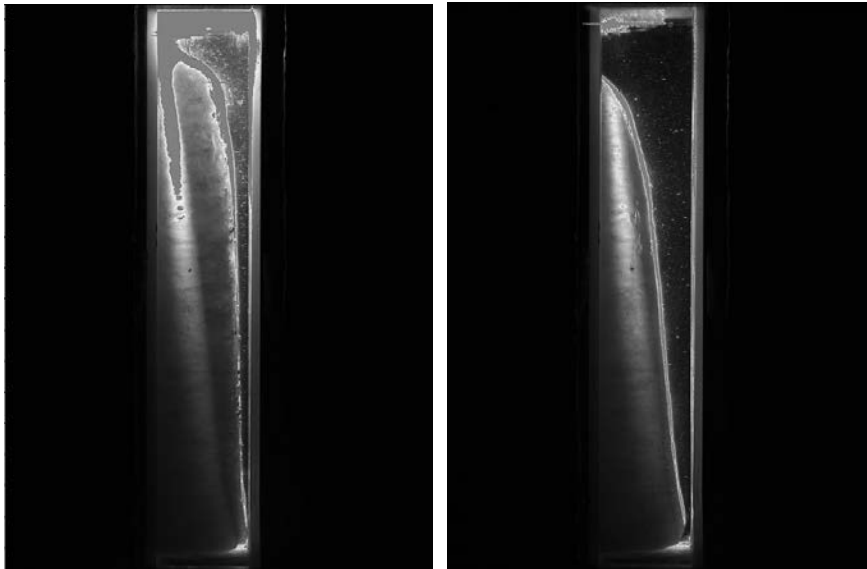


Figure 2.20 – The melting interface. ^a

^a. testing images of n-octadecane without fluorescence dye and tracer particles

melting moments.

At the beginning of melting, the available space for the flow is very small, and it has the same width as that of convection flow boundary layer. When the melted PCM is driven by natural convection from the bottom to the top of the cavity, this amount of liquid PCM transfers its sensible heat to the solid PCM and thus creates an indentation on the solid-liquid



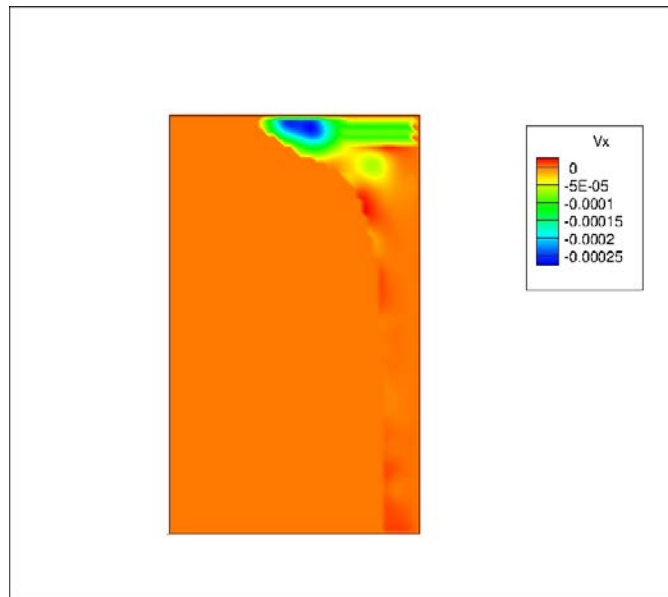
Figure 2.21 – Typical vector field

interface.

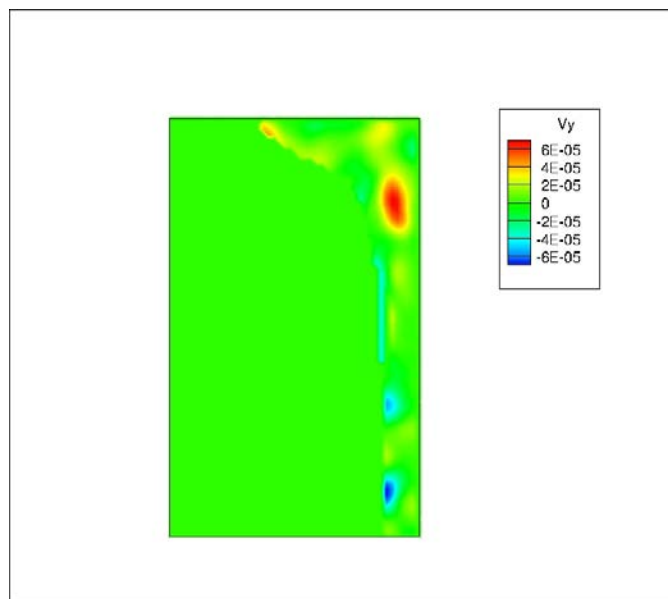
Subsequently, this amount of liquid PCM - together with the newly melted PCM - turns back and flows downwards. However, as soon as they are about to leave the indentation, they encounter the upward flow. Due to the suddenly narrowed cavity for flow, the downward flow is pushed back. This counter-direction flow helps to form a vortex in the vicinity of the lower part of the indentation. This phenomenon is illustrated by the contours of V_x and V_y in Figure 2.22, on which we can clearly notice a strong vortex.

As the melting progresses, the solid-liquid interface retreats. The nature convection in the liquid phase has then a gradually bigger cavity, which means that the vortex occurring at the beginning will disappear. From the Figure 2.23, although we can still see the vortex but it starts to fade. This might explain the phenomenon aforementioned that the solid-liquid interface maintains a curve shape and progressively becomes linear. We can also notice that the vortex always appears in the vicinity of the lower part of the indentation.

Due to the existence of the vortex, the liquid with higher temperature from the indentation cavity cannot move downwards thoroughly. This would attenuate the natural convection beneath, as a consequence, decelerate the melting speed of solid PCM located at the bottom of the cavity.

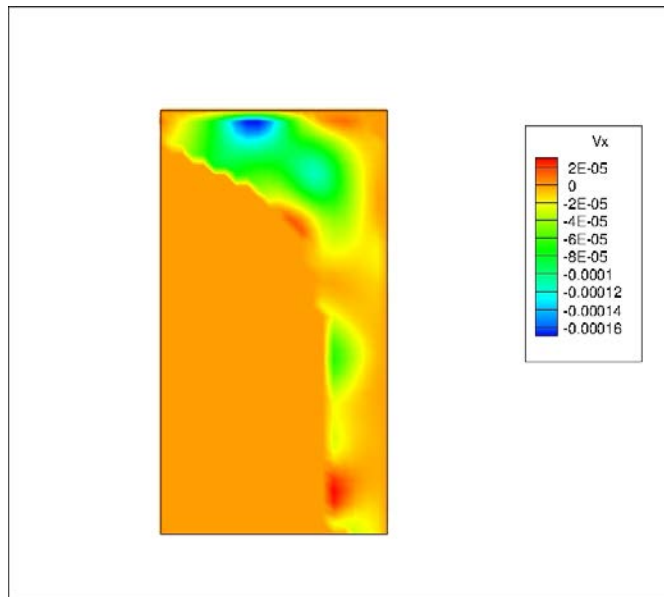


(a) V_x

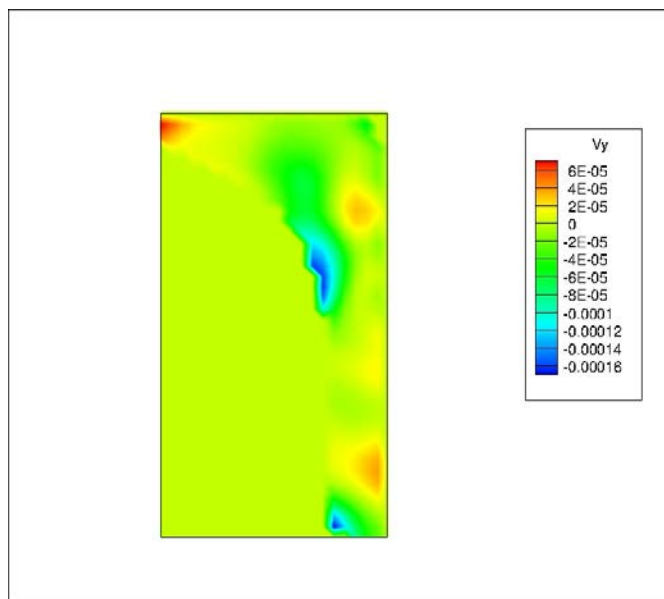


(b) V_y

Figure 2.22 – Contour of velocity at moment 1



(a) V_x



(b) V_y

Figure 2.23 – Contour of velocity at moment 2

2.5.4 Heat transfer rate

The average heat flux transferred through the vertical sides is sampled by heat flux meter (see Sec. 2.3.3). The heat transferred into the brick is denoted by Nusselt number (\overline{Nu}).

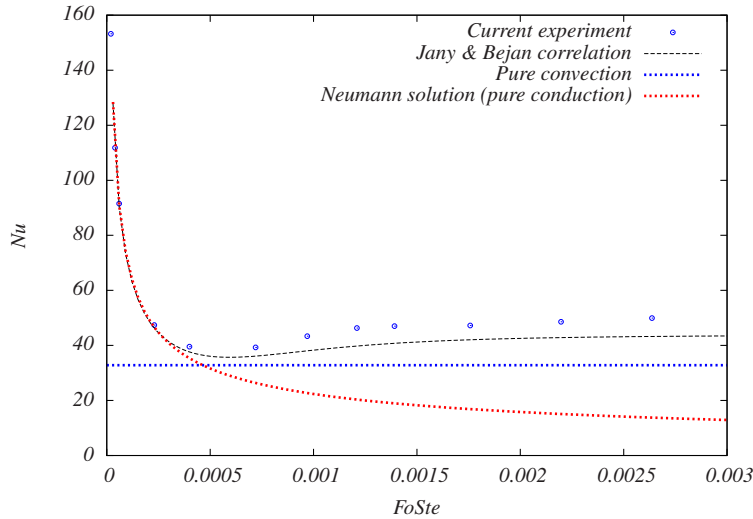


Figure 2.24 – Average \overline{Nu} numbers of the hot wall

Figure 2.24 shows the \overline{Nu} number evolution with dimensionless time ($Ste Fo$). In addition to the experimental results, the correlations of melting from Jany and Bejan [54], the pure conduction and pure convection curves are also presented.

The correlation of Jany and Bejan is:

$$\overline{Nu} = (2\theta)^{-\frac{1}{2}} + \left[c_1 Ra^{\frac{1}{4}} - (2\theta)^{-\frac{1}{2}} \right] \left[1 + \left(c_2 Ra^{\frac{3}{4}} \theta^{\frac{3}{2}} \right)^n \right]^{\frac{1}{n}} \quad (2.10)$$

where $c_1 = 0.35$ and $c_2 = 0.0175$, $\theta = Ste Fo$.

The pure conduction is calculated by:

$$\overline{Nu}_{\text{conduction}} = (2\theta)^{-0.5} \quad (2.11)$$

The pure convection \overline{Nu} evolution is calculated by the following equation [99]:

$$\overline{Nu} = 0.22 \left(\frac{Pr}{0.2 + Pr} Ra \right)^{0.28} \left(\frac{H}{L} \right)^{-\frac{1}{4}} \quad (2.12)$$

when

$$\left[\begin{array}{l} 2 \leq \frac{H}{L} \leq 10 \\ Pr \leq 10^5 \\ 10^3 \leq Ra \leq 10^{10} \end{array} \right]$$

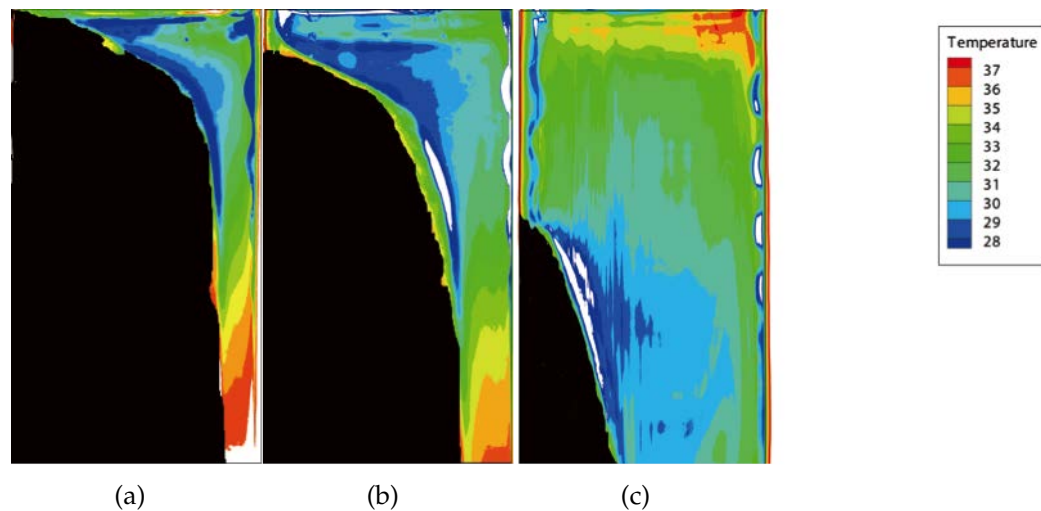


Figure 2.25 – The contours of temperature at three different moment

At the beginning, the melting is dominated by conduction. This transient heat conduction can be calculated by Eq. 2.11. The experimental results and those correlations go quite well with each other in Figure 2.24. With melting going on, the natural convection occurs and gradually prevails over conduction. We could estimate the starting time of convection from Figure 2.24 around $t = 0.000315$.

From Figure 2.24, we can also see that when melting enters a stable state, its heat transfer rate is slightly higher than pure convection. However, if comparing the experimental results with the pure conduction correlation, we can notice a very large difference. This means that the existence of natural convection strongly increases the heat transfer rate. The bigger the Ra number is, the stronger the natural convection is, resulting in a higher heat transfer rate.

2.5.5 Temperature contour

This section presents the LIF temperature measurement results. The temperature contours at three different moments are shown in Figure 2.25. The temperature stratification shows the impact of natural convection in the liquid phase. The hot liquid close to the heating wall moves to the top of the cavity and finally reaches the solid-liquid interface; the cold liquid close to the solid liquid interface falls down. At the beginning, the narrow cavity of the lower part has a very feeble convection, where the major heat transfer form is conduction, and the temperature gradient is high (see 2.25a).

Besides, as mentioned in section 2.5.3, because of the existence of the

vortex in the vicinity of the lower part of the indentation, the low-temperature liquid cannot completely move downwards. This results in the temperature in the vortex region being close to the melting temperature ($T_f = 28^\circ\text{C}$).

Furthermore, when the melting reaches the stable stage, the temperature contour stratifications on the top part of the liquid cavity has almost the same pattern of that of natural convection in a rectangular enclosure (see 2.25c).

2.6 Conclusions and remarks

The solid-liquid phase change is an essential physical process for the latent heat energy storage. In this experimental study, a rectangular transparent building brick was designed and used as the PCM container. The traditional experimental approaches largely depend on thermocouples to obtain the temperature information. In our experiment, no thermocouples were actually embedded into the brick, since even a small amount of thermocouples could influence the feeble convection during melting. Instead, two non-intrusive methods - Particle Image Velocimetry (PIV) and Laser-Induced Fluorescence (LIF) - were employed to obtain the velocity fields and temperature distributions during melting. Meanwhile, heat flux meters were used to obtain the mean heat flux through the heating wall.

2.6.1 Conclusions

The melting process of the interface in the transparent wall brick can be identified as four different stages. From the pure conduction to the coexistence of both conduction and convection, and then finally the convection dominating the heat transfer process. The strong convection at high Ra number dramatically characterises the melting process, not only by changing the solid-liquid interface but also by increasing the heat transfer rate (Nu).

The melted PCM liquid moves to the top due to convection and transfers the heat to the solid PCM there. However when this liquid part falls down, it meets the upwards flow, which forms a flow vortex in the vicinity to the lower part of the indentation on the solid-liquid interface. This attenuates the natural convection on the bottom of the melted liquid cavity. Consequently on the bottom part, the dominant heat transfer form is still conduction.

The temperature stratifications on the top cavity has the same pattern as that of pure convection in a rectangular enclosure as shown by the temperature contours. The PCM liquid in the lower cavity has a high temperature gradient.

Compared to the heat transfer rate of the pure conduction and the pure convection in a rectangular enclosure, the melting coupled with convection has a slightly higher heat transfer rate than pure convection and a much higher value than the pure conduction (approximately 3 times higher).

2.6.2 Remarks on the combination of the PIV and the LIF

The PIV as an experimental method has been well developed and applied to plenty of scenarios. However the LIF is still an immature way to obtain the temperature information of the flow. From the literature review, the LIF has a relatively high uncertainty for temperature measurement - approximately 1.5 °C- which could not be acceptable for a low temperature range application. As a matter of fact, many different factors can easily impact the LIF measurement accuracy (see [Table 2.2](#)).

If we focus on our experiment set-up, the combined employment of the LIF and the PIV poses some extra problems. As we know, for the PIV measurement, the duration of one laser burst should be short enough to capture the sharp particles' images. Nevertheless, for the LIF measurement, the fluorescence dye requires a long exposure to the laser in order to get excited. Those two requirements of the PIV and the LIF apparently are quite contradictory, which is why we used a high power output Nd-YAG laser to solve it.

However, doing this poses another problem. The laser power attenuation along the height is noticeable. Meanwhile, the existence of the solid-liquid interface can severely reflect the incident laser, which strongly increases the local light intensity. The worst consequence is that the camera CCD sensor got over exposed in those regions (the white parts in [Figure 2.25](#)).

Deploying particles coated with the fluorescence material might be a possible solution, although there are very few particles of this type available in the commercial market. Besides, their high density (comparing to n-octadecane) would cause other problems as previously mentioned.

All in all, the combination of the PIV and the LIF to experimentally study the phase change process introduces a new promising approach in order to better understand the solid-liquid phase change. Further improvements are necessary.

Part II

Numerical method

Failure is the condiment that gives success its flavour.
TRUMAN CAPOTE

This page is left blank on purpose.

Numerical simulation on 2D

3.1 Introduction

Heat storage technologies now are widely used as an effective means to manage the energy availability and decrease the temperature fluctuations in various practical applications, such as in the electronics industry [100], the automotive industry [101, 102] and building design [31, 45]. Compared to the sensible heat storage [103], the latent heat storage has a significant advantage as it uses less storage volume to achieve a specified amount of heat load. Furthermore, in general, latent heat storage process is a constant temperature process.

One of the most important physical phenomena of latent heat storage is the solid-liquid phase change, which is also a very critical process for many other applications such as in the metal casting industry. To better understand the solid-liquid phase change, we need to know the temperature distribution in both solid and liquid phases, the flow characteristics in liquid phase, the heat transfer characteristics and the transient interface location. However, the solid-liquid phase change phenomenon is a complex process which couples the natural convection in the liquid phase, the shifting of the solid-liquid boundary and a heat transfer process. Due to these reasons, the solid-liquid phase change is a strong non-linear process, difficult to analyse except for simple and ideal test cases.

The traditional way to simulate numerically the solid-liquid phase change by solving the Navier-Stokes equations is an effective method [55, 84]. The key aspect being the switching of the advection term on and off during the phase change. Notwithstanding, the obstacles one must overcome to locate the solid-liquid interface and to apply the boundary conditions still represent a complicated task.

In the past two decades the lattice Boltzmann method (LBM) matured as a promising approach for CFD due to its intrinsic parallelism and good

numerical stability along with favourable numerical dissipation properties [104]. All of those advantages make LBM a promising complementary approach to the direct solution of the Navier-Stokes (NS) equations. In relatively recent studies, some researchers have begun to choose LBM to simulate phase change [105–109].

In order to make the most of the inherent parallelism of LBM, numerous efforts have been devoted to harness the calculation power of graphic processing units (GPU) [110–113]. A GPU is characterised by its highly parallel, manycore structure, which is especially suited for data intensive calculations. Because more transistors are used to perform data operations, a GPU performs considerably more float-point operations per time unit and has a large memory bandwidth than a CPU counterpart [114]. Since GPUs were initially used to render graphics, using them for a general purpose calculation remains complex and prevents an easy implementation.

In this chapter, an approach is presented to numerically simulate the melting with natural convection. We developed a highly efficient solver, running on a graphic processing unit, for the liquid-solid melting phase change. The hybrid thermal lattice Boltzmann method is employed to simulate the natural convection in the liquid phase. For phase change, the enthalpy formulation is used. Because the total latent heat of each grid is the function of temperature and can embody the status of the material in the grids, it is used as the key parameter to locate the interface. The simulation program is optimized for parallel computing. Besides, experiments presented in chapter 2 are used to validate the present numerical simulation.

We will start with an introduction of the LBM. Afterwards we will talk about the thermal LBM for phase change simulation, what follows is about the GPUs – its hardware and coding pattern –, then the algorithm and its implementation. In the end, the results and remarks will be presented.

3.2 Lattice Boltzmann Method

For the macroscopic system, when the representative physical length scale (L) is far bigger than the molecule mean free path (λ), *i.e.*

$$\text{Kn} = \frac{\lambda}{L} \ll 1 \quad (3.1)$$

where Kn is Knudsen number, the fluid materials can be assumed as continuum. This continuous materials assumption is successfully applied to the fluid mechanics studies. Although Navier-Stokes equations has been widely used to describe the continuous flow, it is sometimes very hard to solve those N-S equations. In addition, for some flow system, it is impossible or very difficult to get its own control equations.

When the continuous material assumption is not applicable or the systems that can't be described by macroscopic equations, it is maybe more convenient to use molecular dynamics or mesoscopic gas kinetic theory to describe the fluid system.

On the one hand, initially, lattice Boltzmann method (LBM) was derived from lattice gas automata (LGA) in the 70s of 20th century. The latter is a simplified model of molecular dynamics.

On the other hand, LBM could also be considered as a special discrete form of the continuous Boltzmann equation (BE) [115,116], BE is the fundamental equation of mesoscopic gas kinetic theory. This concept helps LBM distinguish itself from LGA.

In this section, we will show how to get continuous Boltzmann equation from gas kinetic theory. Afterwards, we will introduce the Boltzmann equation -Bhatnagar-Gross-Krook model (BE-BGK), and LBGK model. In the end, LBE-multiple-relaxation-time model (LBE-MRT) will be depicted. One thing need to be mentioned is that the derivation from LGA to LBE is not included in this section, for someone who is interested in this topic, those references [117–120] could be helpful.

3.2.1 Boltzmann equation

Boltzmann equation is the fundamental equation in gas kinetic theory, it is used to describe the statistical behaviour of a non-equilibrium thermodynamic system. Instead of considering an individual molecule, Boltzmann equation cares about the probable status changes of very small groups of molecules. In order to get the Boltzmann equation, we have to accept three assumptions:

1. Collisions just happen between two particles;
2. Before collision, the two particles are uncorrelated;
3. External force exerts no impact on the local particle collision.

The density distribution (f) is a function of position $\mathbf{r}(x, y, z)$, molecule velocity $\boldsymbol{\zeta}(\zeta_x, \zeta_y, \zeta_z)$ and time t . $f(\mathbf{r}, \boldsymbol{\zeta}, t)d\mathbf{r}d\boldsymbol{\zeta}$ represents all the molecules with velocity between $\boldsymbol{\zeta}$ and $\boldsymbol{\zeta} + d\boldsymbol{\zeta}$ at moment t in the small volume $d\mathbf{r} = dx dy dz$.

We denote the external force as ma . Within time dt , there is no collisions between molecules. Because of the external force, the molecules change their positions from \mathbf{r} to $\mathbf{r} + d\mathbf{r}$ and their velocities from $\boldsymbol{\zeta}$ to $\boldsymbol{\zeta} + a\mathbf{t}$. Obviously, at instant $t + dt$, we have Eq. 3.2 to describe the molecules' states change.

$$f(\mathbf{r} + d\mathbf{r}, \boldsymbol{\zeta} + a\mathbf{t}, t + dt)d\mathbf{r}d\boldsymbol{\zeta} = f(\mathbf{r}, \boldsymbol{\zeta}, t)d\mathbf{r}d\boldsymbol{\zeta} \quad (3.2)$$

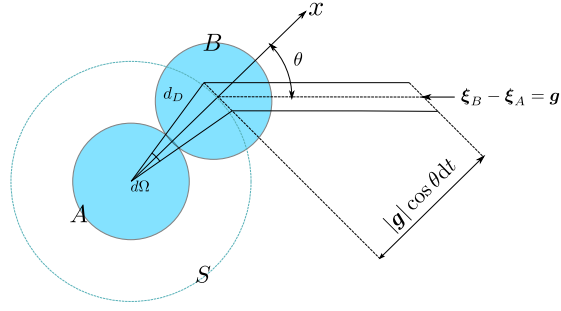


Figure 3.1 – Two-body collision diagram

Performing Taylor expansion on the left side of Eq. 3.2 and then let $dt \rightarrow 0$, we get

$$\frac{\partial f}{\partial t} + \boldsymbol{\zeta} \cdot \frac{\partial f}{\partial \mathbf{r}} + \mathbf{a} \cdot \frac{\partial f}{\partial \boldsymbol{\zeta}} = 0 \quad (3.3)$$

written in another form, *i.e.*

$$\left(\frac{\partial f}{\partial t} \right)_{\text{propagation}} = -\boldsymbol{\zeta} \cdot \frac{\partial f}{\partial \mathbf{r}} - \mathbf{a} \cdot \frac{\partial f}{\partial \boldsymbol{\zeta}} \quad (3.4)$$

where $\left(\frac{\partial f}{\partial t} \right)_{\text{propagation}}$ is the variation of $f(\mathbf{r}, \boldsymbol{\zeta}, t)$ caused by molecule movements. If we add the impact of molecule collision, Eq. 3.2 becomes as

$$\left(\frac{\partial f}{\partial t} \right) = \left(\frac{\partial f}{\partial t} \right)_{\text{propagation}} + \left(\frac{\partial f}{\partial t} \right)_{\text{collision}} \quad (3.5)$$

or

$$\frac{\partial f}{\partial t} + \boldsymbol{\zeta} \cdot \frac{\partial f}{\partial \mathbf{r}} + \mathbf{a} \cdot \frac{\partial f}{\partial \boldsymbol{\zeta}} = \left(\frac{\partial f}{\partial t} \right)_{\text{collision}} \quad (3.6)$$

In order to get the collision item $\left(\frac{\partial f}{\partial t} \right)_{\text{collision}}$ in Eq. 3.5, according to the *collision theory* in the gas kinetic theory, let consider a two-body collision, molecules are assumed to have constant motion and act as hard sphere when colliding. Besides, the collisions are assumed to be perfectly elastic, which is to say when two molecules collide, there is no change in the total translational kinetic energy.

Assuming all the molecules particles have the same mass m and same diameters d_D , an A molecule and a B molecule have velocities $\boldsymbol{\zeta}_A, \boldsymbol{\zeta}_B$ before collision and $\boldsymbol{\zeta}'_A, \boldsymbol{\zeta}'_B$ after collision (see Figure 3.1). They should satisfy the mass and momentum conservation:

$$m\boldsymbol{\zeta}_A + m\boldsymbol{\zeta}_B = m\boldsymbol{\zeta}'_A + m\boldsymbol{\zeta}'_B \quad (3.7)$$

$$\frac{1}{2}m\boldsymbol{\zeta}_A^2 + \frac{1}{2}m\boldsymbol{\zeta}_B^2 = \frac{1}{2}m\boldsymbol{\zeta}'_A^2 + \frac{1}{2}m\boldsymbol{\zeta}'_B^2 \quad (3.8)$$

If we use \mathbf{n} as the unit vector on x-axis, from Eq. 3.7 and Eq. 3.8, we can get

$$\begin{aligned} (\xi'_B - \xi'_A) \cdot \mathbf{n} &= -(\xi_B - \xi_A) \cdot \mathbf{n} \\ |\xi'_B - \xi'_A| &= |\xi_B - \xi_A| = |\mathbf{g}| \end{aligned} \quad (3.9)$$

where \mathbf{g} is the relative velocity of molecule A and molecule B. Eq. 3.9 shows that before and after collision, the relative velocity \mathbf{g} of molecule A and molecule B keeps constant and the velocity components on x-direction reverses. At the same time, the following relation is also valid:

$$d\xi'_A d\xi'_B = d\xi_A d\xi_B \quad (3.10)$$

Molecule A and molecule B will collide when the distance between their centres equals the sum of their radii. If molecule A with relative velocity $\xi_B - \xi_A = \mathbf{g}$ wants to collide molecule B at surface element dS , the centre of molecule A traces a straight line, this straight line must reside in a cylinder with a height of $|\mathbf{g}| \cos \theta dt$ and the bottom surface of $dS = d_D^2 d\Omega$. The volume of this cylinder is thus $d_D^2 |\mathbf{g}| \cos \theta d\Omega dt$. As a result, the total number of the molecules As that can collide with molecule B is calculated by

$$f(\mathbf{r}, \xi_B, t) d_D^2 |\mathbf{g}| \cos \theta d\Omega dt d\xi_B \quad (3.11)$$

Consequently, between time interval dt , the collision times at the surface dS of molecules within the velocity $d\xi_A$ and $d\xi_B$ is

$$f(\mathbf{r}, \xi_A, t) f(\mathbf{r}, \xi_B, t) d_D^2 |\mathbf{g}| \cos \theta d\Omega dt d\xi_B d\mathbf{r} d\xi_A \quad (3.12)$$

After collision, the previous molecules within $d\xi_A$ and $d\xi_B$ change their velocities to $d\xi'_A$ and $d\xi'_B$. This means the collision times equal to the molecules' decrease. Compute the integral of $d\xi_B$ and $d\Omega$ in Eq. 3.12, we thus get molecules' decrease due to the collisions within the time interval dt is

$$d\mathbf{r} d\xi_A dt \iint f(\mathbf{r}, \xi_A, t) f(\mathbf{r}, \xi_B, t) d_D^2 |\mathbf{g}| \cos \theta d\Omega d\xi_B \quad (3.13)$$

Likewise, due to the collisions, the molecules increase is

$$d\mathbf{r} d\xi'_A dt \iint f'(\mathbf{r}, \xi_A, t) f'(\mathbf{r}, \xi_B, t) d_D^2 |\mathbf{g}| \cos \theta d\Omega d\xi'_B \quad (3.14)$$

From Eq. 3.10, Eq. 3.15 becomes

$$d\mathbf{r} d\xi_A dt \iint f'(\mathbf{r}, \xi_A, t) f'(\mathbf{r}, \xi_B, t) d_D^2 |\mathbf{g}| \cos \theta d\Omega d\xi_B \quad (3.15)$$

so we can get the molecules' net change due to collision (general form)

$$\left(\frac{\partial f}{\partial t} \right)_{\text{collision}} = \iint (f' f'_A - f f_A) d_D^2 |\mathbf{g}| \cos \theta d\Omega d\xi_A \quad (3.16)$$

where the integrals on the right side are

$$\int d\Omega = \int_0^{2\pi} d\phi \int_0^{\pi/2} \sin\theta d\theta \quad (3.17)$$

$$\int d\boldsymbol{\xi}_A = \int \int \int_{-\infty}^{+\infty} d\xi_{Ax} d\xi_{Ay} d\xi_{Az}$$

$f_A = f(\mathbf{r}, \boldsymbol{\xi}_A, t)$ and $f = f(\mathbf{r}, \boldsymbol{\xi}_B, t)$.

Finally, we get the control equation of distribution function f , which is known as the **Boltzmann equation**:

$$\frac{\partial f}{\partial t} + \boldsymbol{\xi} \cdot \frac{\partial f}{\partial \mathbf{r}} + \mathbf{a} \cdot \frac{\partial f}{\partial \boldsymbol{\xi}} = \iint (f' f'_A - f f_A) d_{\mathbb{D}}^2 |\mathbf{g}| \cos\theta d\Omega d\boldsymbol{\xi}_A \quad (3.18)$$

The Boltzmann equation is a complex differential integral equation. Its right side is called collision term, which is usually denoted as $J(f)$. This collision term is the most difficult part to get solved. Many studies are carried out in order to simplify $J(f)$.

At last, by integrating the distribution function f with molecule velocities $\boldsymbol{\xi}$, we can get the the following macro quantities.

Density:

$$\rho = \int f d\boldsymbol{\xi} \quad (3.19)$$

Total momentum:

$$\rho \mathbf{u} = \int \boldsymbol{\xi} f d\boldsymbol{\xi} \quad (3.20)$$

and total energy:

$$\rho E = \rho e + \frac{1}{2} \rho u^2 = \int \frac{\xi^2}{2} f d\boldsymbol{\xi} \quad (3.21)$$

where e is internal energy of the unit volume.

3.2.1.1 Collision invariant

Collision term in Boltzmann equation has some characteristics, the important one is

$$\int J(f) \psi(\boldsymbol{\xi}) d\boldsymbol{\xi} = 0 \quad (3.22)$$

where $\psi = 1, \boldsymbol{\xi}, \xi^2/2$. $1, \boldsymbol{\xi}, \xi^2/2$ are known as basic collision invariants. As a matter of fact, when the molecules collide, their mass, momentum and energy keep constant:

$$1 + 1 = 1 + 1$$

$$m\boldsymbol{\xi}_A + m\boldsymbol{\xi}_B = m\boldsymbol{\xi}'_A + m\boldsymbol{\xi}'_B \quad (3.23)$$

$$\frac{1}{2} m\boldsymbol{\xi}_A^2 + \frac{1}{2} m\boldsymbol{\xi}_B^2 = \frac{1}{2} m\boldsymbol{\xi}'_A^2 + \frac{1}{2} m\boldsymbol{\xi}'_B^2$$

Furthermore, in general, the collision invariants satisfy the following relation:

$$\psi(\xi) + \psi(\xi_A) = \psi(\xi') + \psi(\xi'_A) \quad (3.24)$$

in addition, the linear combination of invariants is also an invariant:

$$\psi(\xi) = A + \mathbf{B} \cdot \xi + C\xi^2 \quad (3.25)$$

3.2.1.2 Maxwell distribution

The Maxwell distribution is an equilibrium distribution. As for equilibrium state, the collision term vanishes (see Eq. 3.16), which means

$$f' f'_A = f f_A \quad (3.26)$$

if we apply logarithm on both sides, it becomes

$$\ln f' + \ln f'_A = \ln f + \ln f_A \quad (3.27)$$

Under this restriction, distribution f make the collision term disappear, so this distribution f is called equilibrium distribution, known as Maxwell distribution and denoted as f^{eq} .

According to Eq. 3.25, f^{eq} can be expressed as:

$$\ln f^{eq} = A + \mathbf{B} \cdot \xi + C\xi^2 \quad (3.28)$$

Combining Eq. 3.19, Eq. 3.20, Eq. 3.21 and Eq. 3.28, we can get the **Maxwell distribution**

$$f^{eq} = \frac{\rho}{(2\pi RT)^{D/2}} \exp \left[-\frac{(\xi - u)^2}{2RT} \right] \quad (3.29)$$

3.2.1.3 Boltzmann equation Bhatnagar-Gross-Krook (BGK) approximation

In the continuous Boltzmann equation, the most complex term is the collision term J (right side of Eq. 3.18), which is a non-linear term. It is very difficult to get it solved. This demands to use a simplified collision form to substitute it. Those simplified collision terms omit the complex detail of the original collision term and just care about the the mean effects of collision process. One of those simplified collision models is proposed by Bhatnagar, Gross and Krook in 1954, called BGK approximation. It is also a so far the the most famous and well utilized simple collision model.

The BGK approximation utilizes a simple collision operator Ω_f to replace the J . Ω_f conserves the following two characteristics:

1. for those collision invariants, $\psi = m, m\xi, \frac{1}{2}m\xi^2$,

$$\int \psi \Omega_f d\xi = 0 \quad (3.30)$$

2. obeying the Boltzmann H theorem, which is

$$\int (1 + \ln f) \Omega_f d\boldsymbol{\xi} \leq 0 \quad (3.31)$$

In the BGK model, the final effect of the collision process is considered to lead the distribution to their equilibrium distributions f^{eq} (Maxwell distribution), and the changing rate is proportional to the subtraction of f and f^{eq} with a factor of ν ,

$$\Omega_f = \nu [f^{eq} - f] \quad (3.32)$$

where ν is not the function of molecule velocity $\boldsymbol{\xi}$.

If we introduce $\tau = \frac{1}{\nu}$, we finally get the **Boltzmann-BGK equation**:

$$\frac{\partial f}{\partial t} + \boldsymbol{\xi} \cdot \frac{\partial f}{\partial \mathbf{r}} + \mathbf{a} \cdot \frac{\partial f}{\partial \boldsymbol{\xi}} = -\frac{1}{\tau} (f - f^{eq}) \quad (3.33)$$

and the Maxwell distribution f^{eq} is

$$f^{eq} = \rho \frac{1}{(2\pi R_g T)^{D/2}} \exp \left[-\frac{(\boldsymbol{\xi} - \mathbf{u})^2}{2R_g T} \right] \quad (3.34)$$

where D is the dimension, e.g. for three dimensions, $D = 3$.

3.2.2 Lattice Boltzmann equation

Lattice Boltzmann equation is initially derived from LGA. Owing to the contributions of He and Luo, LBM is also considered as a specially discretized form of the Boltzmann equation [115, 116].

3.2.2.1 Lattice Boltzmann equation-BGK model (LBGK)

Lattice Boltzmann equation-BGK model (LBGK) is the discretized form of Boltzmann equation. The discretization consists of discretization on time, velocity and space.

3.2.2.1.1 Discretization of time and space The Boltzmann-BGK equation (Eq. 3.33) can be rewritten in the form of *ordinary differential equation*:

$$\frac{df}{dt} + \frac{1}{\tau} f = \frac{1}{\tau} f^{eq} \quad (3.35)$$

and material derivative

$$\frac{df}{dt} = \frac{\partial}{\partial t} + \boldsymbol{\xi} \cdot \nabla \quad (3.36)$$

is the time derivative along the characteristic line $\boldsymbol{\xi}$.

Eq. 3.35 can be integrated over a time step of δ_t :

$$\begin{aligned} f(\mathbf{r} + \boldsymbol{\zeta}\delta_t, \boldsymbol{\zeta}, t + \delta_t) &= \frac{1}{\tau} e^{-\delta_t/\tau} \int_0^{\delta_t} e^{t'/\tau} f^{eq}(\mathbf{r} + \boldsymbol{\zeta}t', \boldsymbol{\zeta}, t + t') dt' \\ &+ e^{-\delta_t/\tau} f(\mathbf{r}, \boldsymbol{\zeta}, t) \end{aligned} \quad (3.37)$$

Assuming that δ_t is small enough and f^{eq} is smooth enough locally,

$$\begin{aligned} f^{eq}(\mathbf{r} + \boldsymbol{\zeta}t', \boldsymbol{\zeta}, t + t') &= \left(1 - \frac{t'}{\delta_t}\right) f^{eq}(\mathbf{r}, \boldsymbol{\zeta}, t) \\ &+ \frac{t'}{\delta_t} f^{eq}(\mathbf{r} + \boldsymbol{\zeta}\delta_t, \boldsymbol{\zeta}, t + \delta_t) \\ &+ \mathcal{O}(\delta_t^2) \end{aligned} \quad (3.38)$$

Furthermore, do Taylor expansion of $e^{-\delta_t/\tau}$ according to δ_t and neglect the terms higher than $\mathcal{O}(\delta_t^2)$. Finally, the Eq. 3.37 becomes

$$f(\mathbf{r} + \boldsymbol{\zeta}\delta_t, \boldsymbol{\zeta}, t + \delta_t) - f(\mathbf{r}, \boldsymbol{\zeta}, t) = -\frac{1}{\tau} [f(\mathbf{r}, \boldsymbol{\zeta}, t) - f^{eq}(\mathbf{r}, \boldsymbol{\zeta}, t)] \quad (3.39)$$

The Eq. 3.39 is the evolution function of distribution f with discrete time.

3.2.2.1.2 Discretization of molecule velocity One microscopic molecule's movements is continuous and has very small impact on the macroscopic velocity. As a result, we simplify the microscopic molecules' velocity $\boldsymbol{\zeta}$ as a finite velocities space $\{\mathbf{e}_0, \mathbf{e}_1, \dots, \mathbf{e}_n\}$, the corresponding distribution functions are discretized as $\{f_0, f_1, \dots, f_n\}$. The time discretized Boltzmann (Eq. 3.39) in discretized velocities space has the following form:

$$f_\alpha(\mathbf{r} + \mathbf{e}_\alpha\delta_t, t + \delta_t) - f_\alpha(\mathbf{r}, t) = -\frac{1}{\tau} [f_\alpha(\mathbf{r}, t) - f_\alpha^{eq}(\mathbf{r}, t)] \quad (3.40)$$

where $\alpha = 0, 1, \dots, n$.

Eq. 3.40 is lattice Boltzmann equation with BGK collision term (LBGK). In addition, the local equilibrium distribution f_α^{eq} is

$$f_\alpha^{eq} = \rho\omega_\alpha \left[1 + \frac{\mathbf{e}_\alpha \cdot \mathbf{u}}{R_g T} + \frac{(\mathbf{e}_\alpha \cdot \mathbf{u})^2}{R_g^2 T^2} - \frac{u^2}{2R_g T} \right] + \mathcal{O}(u^3) \quad (3.41)$$

where the weight coefficient ω_α equals to

$$\omega_\alpha = (2\pi R_g T)^{-\frac{D}{2}} \exp \left[-\frac{e_\alpha^2}{2R_g T} \right] \quad (3.42)$$

3.2.2.2 Lattice Boltzmann equation with multiple relaxation time model (LBE-MRT)

In the LBGK model, each physical value evolves towards its equilibrium state with the same relaxation time τ , which means the LBGK model has a unchangeable unit Prandtl number and thus the transports of momentum and heat are non-adjustable. This restriction makes the LBGK model less flexible as for a CFD method. To address this problem, Chen et. al proposed a method to make the Prandtl number adjustable within a range (from 0.59 to 3.3) when the small temperature difference limit satisfied [121].

D’Humières proposed an another collision model with multiple-relaxation-time (MRT). In the MRT model, the discrete velocities (e_α) are identical as in the LBGK model, whereas the different moments – relating to macroscopic physical values – have different relaxation times. The MRT model is mathematically more complex than LBGK, however it is proved to possess better numerical stability [122].

In the current simulation, we choose the D2Q9 discrete velocity mode (two dimensions, nine predefined propagation directions, see Figure 3.2). The e_α are given as:

$$e_\alpha = \begin{cases} (0, 0) & \alpha = 0 \\ e (\cos [(\alpha - 1)\pi/2], \sin [(\alpha - 1)\pi/2]) & \alpha = 1 - 4 \\ e (\cos [(2\alpha - 9)\pi/4], \sin [(2\alpha - 9)\pi/4]) & \alpha = 5 - 8 \end{cases} \quad (3.43)$$

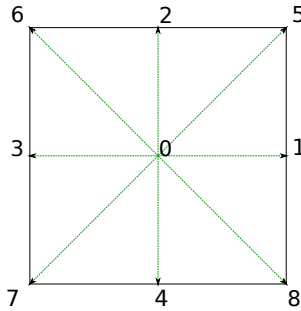


Figure 3.2 – D2Q9 scheme

The updating rule of the MRT-LBM is given by Eq. 3.44 [122], the vector $|f_\alpha\rangle$ is mapped to a moment vector space by a well-designed linear transformation (Eq. 3.45 and Eq. 3.46). Within the D2Q9 stencil, the moment vector $|m_\alpha\rangle$ is described by Eq. 3.45 [104], where ρ is the density, e is related to energy, ϵ is a fourth order moment related to energy square, j_x, j_y are momentums in x and y directions respectively, q_x, q_y are related to the energy flux in x, y directions, and p_{xx}, p_{xy} are higher order terms related to the

stress tensor. In the MRT model, the collision process actually takes place in moment space; after collision, the moments are mapped back to distribution functions; and then the propagation is performed within particle density space.

$$|f_\alpha(\mathbf{x} + \mathbf{e}_\alpha \delta t, t + \delta t)\rangle - |f_\alpha(\mathbf{x}, t)\rangle = -\mathbf{M}^{-1} \cdot \mathbf{S} \cdot [|m_\alpha(\mathbf{x}, t)\rangle - |m_\alpha^{eq}(\mathbf{x}, t)\rangle] \quad (3.44)$$

$$|m_\alpha\rangle = \mathbf{M} |f_\alpha\rangle = (\rho, e, \epsilon, j_x, q_x, j_y, q_y, p_{xx}, p_{xy})^\top \quad (3.45)$$

$$\mathbf{M} = \begin{pmatrix} 1 & 1 & 1 & 1 & 1 & 1 & 1 & 1 & 1 \\ -4 & -1 & -1 & -1 & -1 & 2 & 2 & 2 & 2 \\ 4 & 2 & 2 & 2 & 2 & 1 & 1 & 1 & 1 \\ 0 & 1 & 0 & -1 & 0 & 1 & -1 & -1 & 1 \\ 0 & -2 & 0 & 2 & 0 & 1 & -1 & -1 & 1 \\ 0 & 0 & 1 & 0 & -1 & 1 & 1 & -1 & -1 \\ 0 & 0 & -2 & 0 & 2 & 1 & 1 & -1 & -1 \\ 0 & 1 & -1 & 1 & -1 & 0 & 0 & 0 & 0 \\ 0 & 0 & 0 & 0 & 0 & 1 & -1 & 1 & -1 \end{pmatrix} \quad (3.46)$$

In Eq. 3.44, $|m_\alpha^{eq}\rangle$ are the equilibrium quantities. For the conserved quantities, $m_0^{eq} = \rho^{eq} = \rho$, $m_3^{eq} = j_x^{eq} = j_x$ and $m_5^{eq} = j_y^{eq} = j_y$; and for the other non-conserved values, equilibrium states are calculated by Eq. 3.47 [122]:

$$\begin{aligned} m_1^{eq} &= e^{eq} = -2\rho + 3(j_x^2 + j_y^2) & m_2^{eq} &= \epsilon^{(eq)} = \rho - 3(j_x^2 + j_y^2) \\ m_4^{eq} &= q_x^{(eq)} = -j_x & m_6^{eq} &= q_y^{(eq)} = -j_y \\ m_7^{eq} &= p_{xx}^{(eq)} = \frac{1}{3}(j_x^2 - j_y^2) & m_8^{eq} &= p_{xy}^{(eq)} = \frac{1}{3}j_x j_y \end{aligned} \quad (3.47)$$

The sound speed in lattice units is $c_s = 1/\sqrt{3}$.

In Eq. 3.44, \mathbf{S} is the collision matrix, which is a diagonal square matrix:

$$\begin{aligned} \mathbf{S} &= \text{diag}(s_\rho, s_e, s_\epsilon, s_{j_x}, s_{q_x}, s_{j_y}, s_{q_y}, s_{p_{xx}}, s_{p_{xy}}) \\ &= \text{diag}(0, s_2, s_3, 1, s_5, 1, s_7, s_8, s_9) \end{aligned} \quad (3.48)$$

each diagonal element of \mathbf{S} is one relaxation factor for different moments. According to the reference [104], s_8 and s_2 are controlled by the shear viscosity ν

$$s_8 = \frac{2}{6\nu + 1} \quad (3.49)$$

and by the bulk viscosity ζ

$$s_2 = \frac{2}{12\zeta + 1} \quad (3.50)$$

furthermore,

$$s_5 = s_7 = \frac{8(2 - s_8)}{(8 - s_8)} \text{ and } s_9 = s_8 \quad (3.51)$$

In addition, as long as they are within the interval (0,2) [104], s_2 and s_3 can be chosen arbitrarily to enhance the stability of the simulation.

Finally, the collision matrix S we used for the simulation is

$$S = \text{diag} \left(0, 1.64, 1.54, 1, \frac{8(2 - s_8)}{(8 - s_8)}, 1, \frac{8(2 - s_8)}{(8 - s_8)}, s_8, s_8 \right) \quad (3.52)$$

The LBE can be numerically very stable when solving isothermal flow. However, as solving thermal-hydrodynamics problems, the thermal LBE (TLBE) models are more vulnerable to numerical instabilities. These instabilities are attributed to a spurious algebraic coupling between the shear and energy modes of the linearised evolution operator. This spurious algebraic coupling is rooted in the basic features of LBE. As a result, in order to improve the numerical robustness, Lallemand and Luo proposed a hybrid thermal lattice Boltzmann equation (HTLBE) and proved that it has better numerical stability than the other energy-conserving Boltzmann models [123]. In the HTLBE model, the mass and momentum conservations are solved by MRT-LBE and the temperature by finite differences [124]. Through the Chapman-Enskog analysis, we can successfully recover the macroscopic conservation equations (Eq. 3.53, Eq. 3.54) from this HTLBE. In the current simulation, as a result, the HTLBE model is employed.

3.3 Numerical modelling

3.3.1 Definition of the problem

Phase change materials (PCMs) are used to store or release energy. This process is related to the melting/solidification. In this study, n-octadecane is chosen as PCM of interest; its thermophysical properties used for simulation are presented in Table 3.1. One important property of the n-octadecane is its high Prandtl number. A rectangular container whose dimensions are 30 mm(L) \times 172 mm(H) \times 172 mm(D) filled with n-octadecane -with a height of 152 mm- is heated up from the two vertical sides, the other sides are supposed adiabatic (Figure 3.3 and Figure 3.9). During melting process, the early stage is governed by conduction. Gradually with liquid fraction increasing, the convection develops and then dominates the heat transfer. In the not-yet-melted solid phase, conduction is still the main heat transfer form. The natural convection in the liquid phase causes the upper part of the PCM to melt faster than the bottom part, and, eventually modifies the shape of the solid-liquid interface. In this work, the Rayleigh

number Ra is of the order of 10^8 . As a result, the convection plays an important role during the heat transfer. In the next section (Sec. 3.3.2), we will present the numerical model construction and then in Sec. 3.4 the detailed implementation on GPU.



Figure 3.3 – Experiment enclosure

Table 3.1 – Thermophysical properties of n-octadecane used for simulation [69]

Property	Value
Melting temperature T_f	28.0[°C]
Latent heat λ	1.25×10^5 [J/kg]
Specific heat C_p	1250[J/(kg · °C)]
Thermal conductivity k	0.2[W/(m · K)]
Density ρ	800[kg/m ³]
Kinematic viscosity ν	1×10^{-5} [m ² /s]
Thermal expansion coefficient β	0.002[K ⁻¹]
Thermal diffusivity α	2×10^{-7} [m ² /s]

3.3.2 Model construction

3.3.2.1 The governing equations

For the entire melting process, we assume that the liquid is Newtonian and incompressible, and assume that both the solid and the liquid phases have the same heat capacity. According to Voller *et. al* [75], the governing equations that describe melting phase change are in the following forms:

Continuity equation:

$$\frac{\partial \rho}{\partial t} + \nabla \cdot (\rho \mathbf{u}) = 0 \quad (3.53)$$

Momentum conservation:

$$\frac{\partial (\rho \mathbf{u})}{\partial t} + \nabla \cdot (\rho \mathbf{u} \mathbf{u}) = -\nabla p + \nabla \cdot (\mu \nabla \mathbf{u}) + \mathbf{S}_1 + \mathbf{S}_2 \quad (3.54)$$

Energy conservation:

$$\frac{\partial (\rho C_p T)}{\partial t} + \nabla \cdot (\rho C_p T \mathbf{u}) = \nabla \cdot (k \nabla T) + S_3 \quad (3.55)$$

Where μ is the dynamic viscosity, C_p , k , \mathbf{u} are heat capacity, heat conductivity and macroscopic velocity. \mathbf{S}_1 , \mathbf{S}_2 and S_3 are source terms due to the presence of phase change coupled by natural convection.

In the governing equations, because of the aforementioned existence of phase change, the critical point to be determined during the simulation is whether the advection terms will appear or not. In order to achieve this requirement, Brent *et al.* [71] devises the source terms \mathbf{S}_1 in momentum equation to have a form such as: $\mathbf{S}_1 = A \mathbf{u}$. Moreover, the second source term S_2 is introduced by buoyancy, which is $S_2 = \rho g \beta (T - T_r)$ and T_r is a reference temperature. The momentum equation is then rewritten as:

$$\rho \frac{\partial \mathbf{u}}{\partial t} + \rho (\mathbf{u} \cdot \nabla) \mathbf{u} = -\nabla \cdot p + \mu \nabla^2 \mathbf{u} + A \mathbf{u} + \rho g \beta (T - T_r) \quad (3.56)$$

A can be described by two forms: Carman-Kozeny form or simplified linear form (Eq. 3.57). The symbol l is the liquid fraction, ϵ and C are two simulation dependent constants, the former is used to avoid the division by zero and the latter to describe the morphology of the porous solid-liquid interface [71]. By using this definition of A , the term $A \mathbf{u}$ varies gradually between 0 and a relatively high value according to the liquid fraction in a cell. As a consequence (depending on the magnitude of constant C), $A \mathbf{u}$ dominates the other terms in the momentum equation. From a physical point of view, this process depicts the velocity evolution during the phase change.

$$A = \begin{cases} -C \frac{(1-l)^2}{(l^3 + \epsilon)} & \text{Carman-Kozeny form} \\ -C(1-l) & \text{simplified linear form} \end{cases} \quad (3.57)$$

As for the source term S_3 in the energy equation, we will analysis it in section 3.3.2.2. In the current simulation, the continuity equation and momentum equation will be solved by lattice Boltzmann method and the energy equation by finite differences.

3.3.2.2 Energy equation

Phase change

During melting, the heat is stored in the form of latent heat of fusion. Therefore, the total energy h is the sum of sensible heat and latent heat

as given in Eq. 3.58. We assume that the heat capacity of liquid and solid phases are equal, denoted by C_p . L refers to the latent heat content.

$$h = C_p T + L \quad (3.58)$$

with $L = l \cdot \lambda$, and l is the liquid fraction.

The energy equation in the form of total energy (h) is given by:

$$\frac{\partial \rho h}{\partial t} + \nabla(\rho h \mathbf{u}) = \nabla \cdot (k \nabla T) \quad (3.59)$$

The thermal conductivity k is treated as constant during the melting. As Boussinesq approximation is assumed, the density temperature dependence is only taken into account in the buoyancy force term.

After mathematical operations on Eq. 3.58 and Eq. 3.59, the energy equation becomes:

$$\frac{\partial T}{\partial t} + \nabla(\mathbf{u} \cdot T) = \alpha \nabla^2 T - S_3 \quad (3.60)$$

where S_3 is:

$$S_3 = \frac{\partial(L/C_p)}{\partial t} + \nabla\left(\frac{\mathbf{u} \cdot L}{C_p}\right) \quad (3.61)$$

S_3 comprises the effect of latent heat change. As stated before, the material during melting phase change absorbs the heat and stores it as latent heat of fusion in a narrow range of temperature. This can be considered as a heat sink as described by Eq. 3.61.

In the solid and liquid phase, the term $\nabla\left(\frac{\mathbf{u} \cdot L}{C_p}\right)$ is equal to 0, while along the liquid-solid interface, this term is not 0 but sufficiently small to be neglected.

In order to keep the units consistent with LBM, the energy equation must be transformed to dimensionless form, by choosing the following reference quantities and dimensionless numbers:

$$u_{ref} = \alpha \sqrt{Ra} / H, \quad T_{ref} = \Delta T = T_h - T_f, \quad H_{ref} = H$$

$$Ra = \frac{g \beta \Delta T H^3}{\nu \alpha}, \quad Pr = \frac{\nu}{\alpha}, \quad Ste = \frac{C_p \cdot (T_h - T_c)}{\lambda},$$

then the dimensionless form of the energy equation is

$$\frac{\partial T^*}{\partial t^*} + \nabla^*(\mathbf{u}^* \cdot T^*) = Ra^{-\frac{1}{2}} \nabla^{*2} T^* - S_3^* \quad (3.62)$$

with the source term S_3^* :

$$S_3^* = \frac{1}{\rho \cdot Ste} \frac{\partial l}{\partial t^*} \quad (3.63)$$

where t^* is the dimensionless time, and the liquid fraction l is defined as

$$l = \begin{cases} 1, & T^* \geq T_f^* + \frac{1}{Ste} \\ (T^* - T_f^*) \cdot Ste, & T_f^* < T^* < T_f^* + \frac{1}{Ste} \\ 0, & T^* \leq T_f^* \end{cases} \quad (3.64)$$

Consequently, the temperature at time step n is used to update liquid fraction l , in order to get the source term S_3^* in Eq. 3.62, then using value S_3^* to calculate the temperature in time step $n + 1$ and so on.

Discretization

For coupling with LBM, the energy equation furthermore needs to be discretized. During this step, the reference length and time are selected as the lattice size δx and time step δt . Because the lattices are in the form of a square, so $\delta y = \delta x$. Based on those two reference values, the computation domain has a height in lattice unit $N_y = 1/\delta x$ and the maximum time steps to achieve the prescribed melting process is $t^*/\delta t$.

The energy equation in lattice units is:

$$\frac{\partial T_{lb}}{\partial t_{lb}} + \nabla(\mathbf{u}_{lb} \cdot T_{lb}) = \frac{\delta t}{\delta^2 x} Ra^{-\frac{1}{2}} \nabla^2 \cdot T_{lb} - \frac{1}{\rho \cdot Ste} \frac{\partial l}{\partial t_{lb}} \quad (3.65)$$

where the subscript lb means the lattice units, and $T_{lb} = T^*$, $\rho = 1$.

The finite difference method is used to discretize the diffusion and advection terms. As suggested by Lallemand and Luo [104], for a D2Q9 simulation, the nine point finite-difference operators are used to get the gradients and Laplacian:

$$\begin{aligned} \partial_x T_{lb} |_{(i,j)} = & T_{lb}(i+1, j) - T_{lb}(i-1, j) - \frac{1}{4} [T_{lb}(i+1, j+1) \\ & - T_{lb}(i-1, j+1) + T_{lb}(i+1, j-1) - T_{lb}(i-1, j-1)] \end{aligned} \quad (3.66)$$

$$\begin{aligned} \partial_y T_{lb} |_{(i,j)} = & T_{lb}(i, j+1) - T_{lb}(i, j-1) - \frac{1}{4} [T_{lb}(i+1, j+1) \\ & - T_{lb}(i+1, j-1) + T_{lb}(i-1, j+1) - T_{lb}(i-1, j-1)] \end{aligned} \quad (3.67)$$

$$\begin{aligned} \nabla^2 T_{lb} |_{(i,j)} = & 2[T_{lb}(i+1, j) + T_{lb}(i-1, j) + T_{lb}(i, j+1) + T_{lb}(i, j-1)] \\ & - \frac{1}{2} [T_{lb}(i+1, j+1) + T_{lb}(i-1, j+1) + T_{lb}(i-1, j-1) + T_{lb}(i+1, j-1)] \\ & - 6T_{lb}(i, j). \end{aligned} \quad (3.68)$$

3.3.2.3 Problem solving

The melting in each lattice goes through three stages: 1. pure solid phase; 2. melting stage; 3. pure liquid phase. In the pure liquid stage, there exists the natural convection. The temperature equation and the LBE must be coupled by adding buoyancy force $F = \sqrt{g\beta\Delta T}l_b$ to the momentum along y direction (j_y). In the solid phase stage, there is no flow, so the calculation of LBE must stop. As a result, the simulation has to do three steps successively during each time step: checking the liquid fraction of each lattice; calculating the temperature; deciding whether calculating the velocity field or not according to the liquid fraction of each lattice.

3.4 Nvidia GPU hardware and implementation

This section addresses two topics. The first part gives a concise introduction to the Nvidia CUDA technology. The second one presents the implementation of the algorithm.

3.4.1 GPU with CUDA architecture

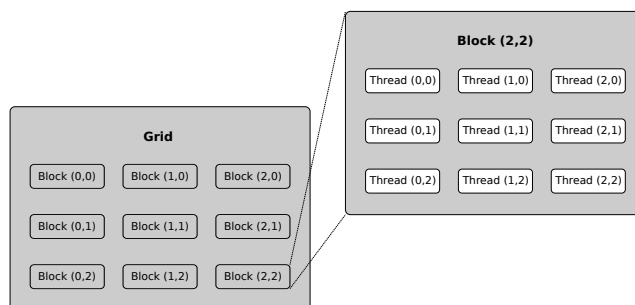


Figure 3.4 – CUDA Block of threads and grid of blocks

3.4.1.1 CUDA program pattern

A modern GPU is characterized by its parallel computing ability, its high data throughput as well as its programmable features. However it was difficult to perform general purpose computations on a GPU before the release of the Nvidia's CUDA technology. The CUDA is a general purpose parallel computing technology, which comes with a set of development tools such as high level language compilers. In this paper, The CUDA C is employed.

The code written using CUDA C is of two types:

- Host code, which consists of functions running on the CPU;

- Device code, which includes: 1. functions (known as *kernel*) invoked by host functions and 2. device functions invoked by kernels and other device functions. Device code is executed on the GPU.

Kernels are launched and executed in parallel by designating an execution pattern through a set of *threads*. The threads are bundled in the form of *thread blocks*. Blocks with equal size are organized into *grids*, see Figure 3.4. Threads and blocks are indexed with two built-in up to 3-dimensions variables: `threadIdx` and `blockIdx`.

3.4.1.2 Memory types

Depending on the accessibility to the memory by kernels, the total memory space on the GPU is categorized by registers, shared memory, constant memory, texture memory and global memory, see Figure 3.5. Global memory can be accessed by each thread during the runtime of the kernel. Global memory is quantitatively abundant but has the slowest access speed. Therefore, avoiding unnecessary global memory readings and writings should be kept in mind when programming. Registers are used to store local variables. They are not addressable and programmers need to pay attention to prevent them from spilling. Shared memory is used to store the local variables which are declared as shared. It is addressable and as fast as register.

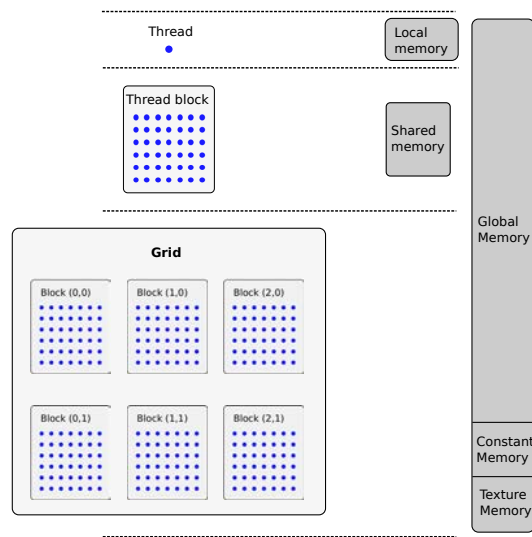


Figure 3.5 – Memory structure of GPU

In addition, there are two types of read-only memory that can be accessed by all the threads during the execution of a kernel, one of which being constant memory. The constant memory space is included and addressed in device memory. However, this memory is cached.

3.4.1.3 CUDA hardware

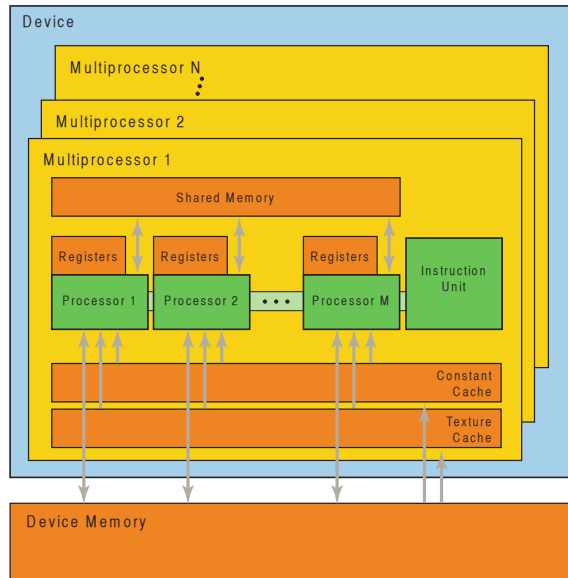


Figure 3.6 – CUDA hardware

The execution resources of a CUDA enabled GPU are organized into Streaming Multiprocessors (SMs). Each GPU equipped with CUDA technology has a number of SMs, for example, Tesla C2050 Nvidia GPU has 14 SMs. Each SM has its own register, shared memory, constant cache, as well as several CUDA cores¹, see Figure 3.6. The SM processes the threads within a block by groups of 32, called *warps*. In this study, we use a Tesla C2050 Nvidia GPU. Its technical specifications are shown in Table 3.2.

Table 3.2 – Specifications of the Tesla C2050

CUDA Capability	2.0
Number of SMs	14
Number of CUDA core per SM	32
Constant memory	65536 bytes
Shared memory per block	49152 bytes
Registers available per block	32768
Global memory	3072 MB
Maximum number of threads per SM	1536
Maximum number of threads per block	1024
Maximum dimension of a block	1024 × 1024 × 64
Maximum dimension of a grid	65535 × 65535 × 65535

1. used to be called Streaming Processors (SPs)

3.4.2 Implementation

Figure 3.7 shows the diagram of nodes. The blue frame embodies the physical boundary. The nodes enclosed by the blue frame are the calculation domain.

The lattices' topology in the computation domain must be mapped to the threads of the execution grid on the GPU [125]. This fulfills the requirement of thread-level parallelism of CUDA GPU [114]. For our 2-dimensional simulation ($LX \times LY$), a one dimensional block of size LX and one dimensional grid of size LY are chosen. We set LX being the major dimension and being a multiple of the warp size, which can provide us a sufficient threads occupancy rate, a coalescence of global memory access and an easy index to the nodes [126].

3.4.2.1 Data and memory utilization

The global memory is accessed via 32, 64, or 128 byte aligned memory transactions. The warp coalesces the threads memory accesses into one or more memory transactions according to the word size accessed by a single thread and the distribution of the memory addresses. In addition, for the GPU with capacity 2.0, the global memory is cached in L1 and L2 by default². The memory is accessed via 128 byte transactions if cached in both L1 and L2; and is accessed via 32 byte transactions if just cached in L2. As a result, a scattered memory addresses distribution across the threads will result in many unused data transactions and less cache hits, which can significantly impact the memory throughput. In this simulation, for each node, nine velocities, one liquid fraction and one temperature value need to be stored in the global memory, which represents eleven single-precision floating-point variables per node. We use a single memory block partitioned into three parts in order to store the distributions array, the temperature array and the liquid fraction array (see Figure 3.8).

The energy equation is solved by finite differences. Because the data stored in the shared memory automatically broadcast themselves to all the threads in a block, in order to decrease the global memory transactions, we use the shared memory to store the temperatures.

In the LBM implementation, the propagation step also requires the neighbor's relevant distributions information, but all those information are local to each thread, thus just need to be stored in registers. As described in reference [126], we also utilize in-place propagation scheme to perform propagation in this simulation (see circle point in Figure 3.7).

For the phase change, the liquid fraction information is also stored in

2. For GPU with capacity 3.x, the global memory accesses are cached on L2 and for capacity 3.5 and higher, can also be cached in the read-only data cache

registers. In the liquid phase, the LBM collision and propagation are fully performed, and in energy equation, the advection term is valid. In the solid phase, the LBM collision and propagation are disabled, and distributions swap with their opposite counterparts. The macro velocities are set to zero and thus the advection term in energy equation disappears.

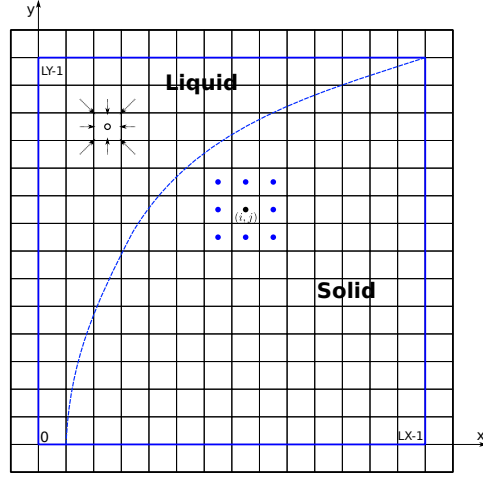


Figure 3.7 – The propagation and temperature scheme



Figure 3.8 – Data structure

3.4.2.2 Boundary conditions and simulation procedure

On the physical walls (blue frame in Figure 3.7), for the LBM, we choose the halfway bounce back scheme. The temperature boundary conditions are applied on the physical walls, which are between two lattices. The boundary condition of the bottom side is:

$$T_{i,-1} = \frac{21T_{i,0} + 3T_{i,1} - T_{i,2}}{23} \quad (3.69)$$

and of the left vertical wall is :

$$T_{-1,j} = \frac{8T_h - 6T_{0,j} + T_{1,j}}{3} \quad (3.70)$$

Besides, the $T_{i,Ly}$ and $T_{Lx,j}$ can be calculated in the same way.

The melting process simulation obeys the following procedure:

1. Initialize model,

2. Execute the propagation, and transfer the current lattice's temperature and its neighbors' temperatures to shared memory,
3. Apply boundary conditions,
4. Compute the liquid fraction and define the node status: liquid or solid,
5. **if the node status is liquid:**
 - Compute the moments of the MRT model, add half of the buoyancy force ($0.5\sqrt{g\beta\Delta T_{lb}}$) to momentum component on y direction \dot{j}_y ;
 - Collide;
 - Add the second half of the buoyancy force to the momentum component \dot{j}_y ,
 - Compute temperature using the discretized energy equation with advection term,
- else:**
 - Swap distributions f_α on their proper opposite directions,
 - Compute the temperature using the discretized energy equation without advection term,
6. Map moment space to discrete velocity space,
7. Update each node for the next iteration.

3.5 Results and discussion

This section addresses the model validation (Sec. 3.5.1), the results of heat transfer and natural convection during melting (Sec. 3.5.2) as well as the performance of this parallel implementation (Sec. 3.5.3).

3.5.1 Model validation

3.5.1.1 Experiment configuration

Experimental data are used for the model validation. The detail about the experiment is addressed in Chapter 2, here we just summarize it.

The experiment was performed on a transparent building brick filled with n-octadecane (see Figure 3.3 and 3.9a). The diagram of the experiment equipment is shown in 3.9b. A CCD camera and a laser beam were connected by a synchronizer to capture images of the melting process. No thermocouple was embedded in the cavity in order to avoid impacting the natural convection flow in the liquid phase. Instead, we chose to use two

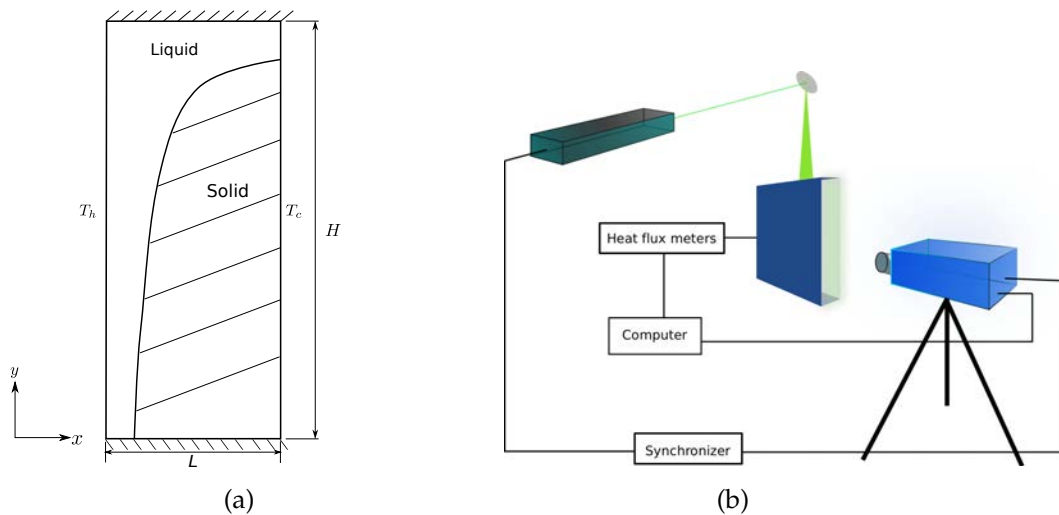


Figure 3.9 – Experiment configuration and diagram

heat flux meters on the heating sides of this enclosure, thus guaranteeing the reliability of average Nu number evolution along the walls. The other sides apart from the top and the front were well isolated using asbestos and thereby considered as adiabatic. Both captured images and heat flux data were registered by a computer controlled by the LaVision and the Labview respectively. Experimental parameters are listed in [Table 3.3](#).

Table 3.3 – Experimental parameters

T_h [°C]	T_c [°C]	H [m]	L [m]
35.0	27.8	0.152	0.03

3.5.1.2 Model validation

The convergence test was performed under different mesh resolutions. [Figure 3.10](#) displays the relative differences of Nu number between the simulation and the analysis [54] at time $\tau = 0.00312$ (5000 s). All the simulations were carried out with a fixed viscosity of 0.01 and the Mach number equal to 0.1. A satisfactory quadratic convergence in space is achieved by the model.

In [Figure 3.11](#), melting interface positions are shown at five different instants. Both experimental data and simulation results are displayed. The conversion between the physical time and the dimensionless time ($\tau = FoSte$) is expressed by $t = (H^2 \cdot FoSte / \alpha)$. The simulation curves are in good agreement with the experimental points. At the onset of melting, n-octadecane is solid, so the melting is just driven by pure conduction.

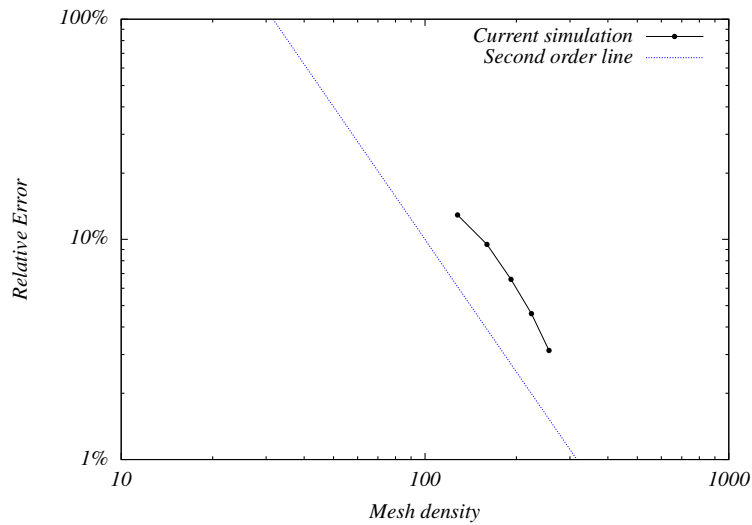


Figure 3.10 – Grid dependence

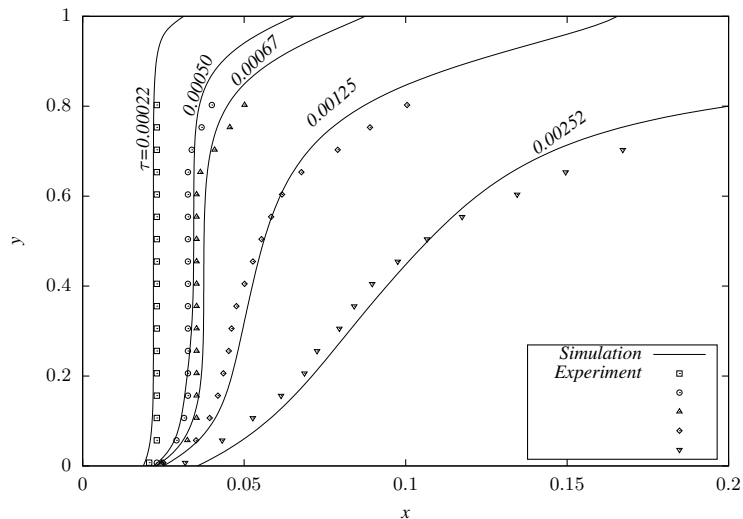


Figure 3.11 – The evolution of melting interface with the dimensionless time: comparison between simulation and experiment. $Ra = 2.48 \times 10^8$, $Pr = 50$, $Ste = 0.072$

The first curve at dimensionless time equal to 0.00022(353.0s) is parallel to the vertical heating wall. On the bottom part of the interface, when $0.1 < y < 0.6$, the simulation results embody the position of the interface. Notwithstanding, the upper portion of the curves retreats slightly more slowly than in the experimental counterparts. This might be due to the fact that the top of the cavity is not perfectly insulated.

Figure 3.12 shows the average Nusselt number of the hot vertical wall.

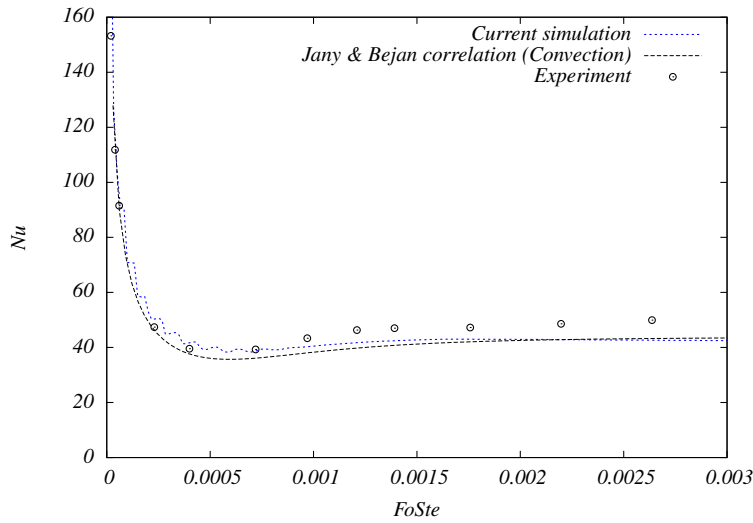


Figure 3.12 – Average Nu number on the left vertical isothermal wall (T_h) during melting of n-octadecane. $Ra = 2.48 \times 10^8$, $Pr = 50$, $Ste = 0.072$

The Nusselt number is defined as the amount of heat transferred:

$$Nu = - \int_0^1 \left(\frac{\partial T^*}{\partial x^*} \right) dy^*$$

The Rayleigh number is $Ra = 2.48 \times 10^8$ and the Prandtl number is $Pr = 50$. The black long-dashed line is from the correlation by Bejan et al [54]. All the three sets of results follow the same pattern. In the beginning, the average Nu starts with a high value, and decreases rapidly with the same order of $\tau^{-1/2}$ as the pure conduction, known as simplified solution of Stefan problem. Later, when the natural convection emerges, the decrease of the Nusselt number becomes moderate, as shown by the curves' gradients on Figure 3.12. Within this elapse of time, the conduction and convection not only exist simultaneously but also exert the same influence on the heat transfer effect. As aforementioned, when convection dominates the melting process, Nu becomes stationary with respect to time. Comparing with Figure 3.11, when $\tau = 0.00022$, the solid-liquid interface has already exhibited the existence of convection, at the same time, Nu begins its transition.

3.5.2 Simulation results

Figure 3.13 shows the temperature contours at different instants. In most published papers, simulations of melting process driven by natural convection are limited, within low Ra with order of magnitude of 10^7 and low Pr number [75, 127, 128]. From the contours, the convection drags the

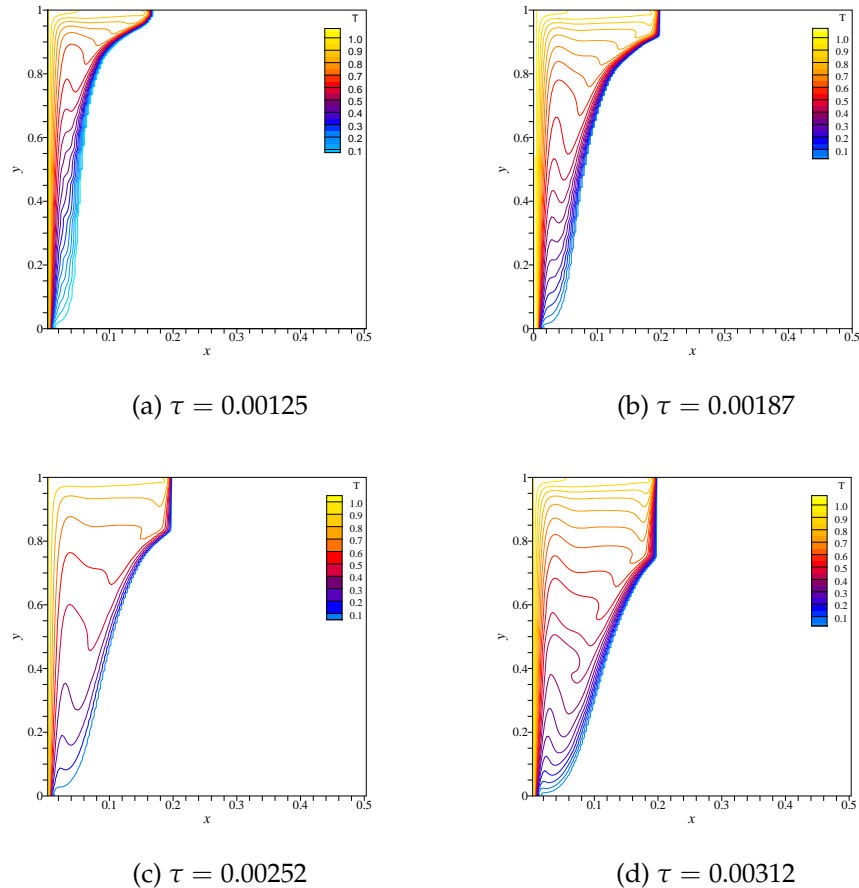


Figure 3.13 – Temperature contours at four different τ . $Ra = 2.48 \times 10^8$, $Pr = 50$, $Ste = 0.072$

heated melted n-octadecane to the top and the liquid phase is stratified. However, this stratification is different from the results of Okada [51], in which the contour of temperature in the middle of the liquid cavity is parallel to the horizontal wall and the Ra is of order 10^6 . In contrast here in 3.13a, the contours are more prone to be vertical. The reason is the higher Ra number in our study and thus a larger degree of convection: as soon as the melted n-octadecane is heated up, the buoyancy force drives it upwards. At the same time, since at the bottom part the flow cavity is quite narrow, the flow rises fast.

From 3.14a, we notice there are two eddies appearing at the height about 0.65 and 0.80. The up rising liquid ultimately reaches the top wall, and turns back. However, when it encounters the newly melted uprising liquid, there is not enough space to let it go down. With the melting developing, the liquid cavity enlarges, and one eddy disappears, see 3.14b and

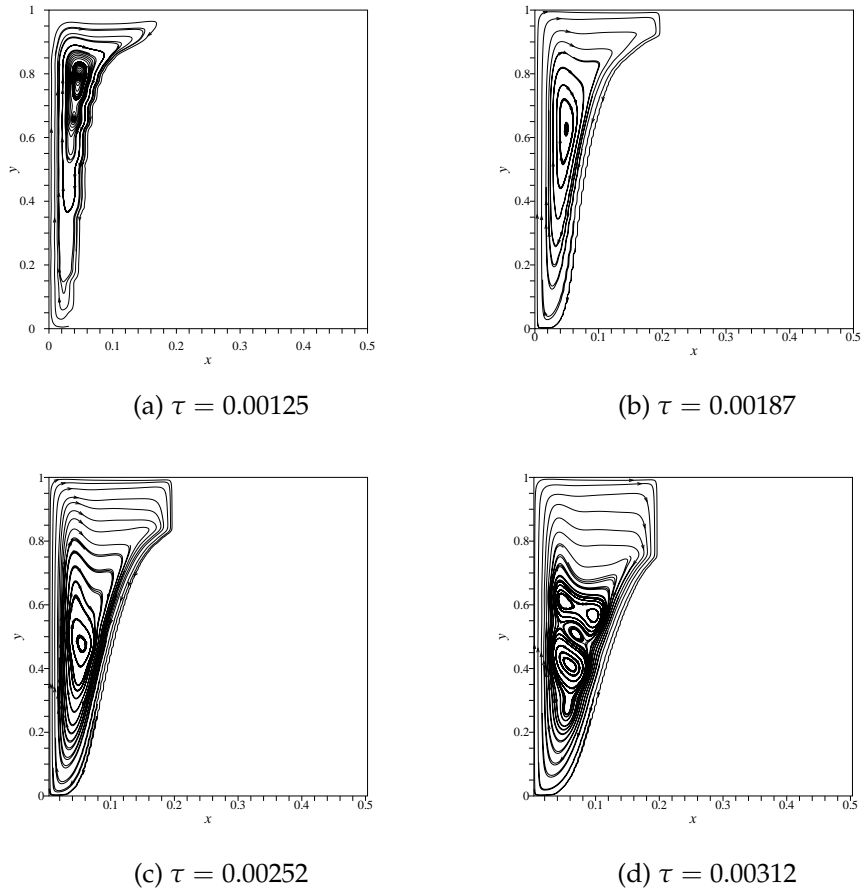


Figure 3.14 – Streamlines at four different τ . $Ra = 2.48 \times 10^8$, $Pr = 50$, $Ste = 0.072$

3.14c. The solid-liquid interface finally reaches the cold wall and shrinks towards the right bottom corner. When the interface becomes small enough, the large amount of downward cold flow from the cold wall detaches from the solid-liquid interface. This amount of detached flow encounters the upward hot flow, which eventually causes several eddies to emerge between $y = 0.35$ and $y = 0.65$ (See 3.14d). We can also note that the isothermal lines at the corresponding positions in 3.13d become distorted due to those eddies.

From this analysis, we can find that the melting process with higher Ra number has distinct characteristics from that with lower Ra number. When the Ra number is lower than 10^7 [51], the natural convection is just a single circulation, the central part of the liquid cavity remains still. In the present simulation, since both the Ra and Pr numbers are high, 2.48×10^8 and 50 respectively, the natural convection manifests a different flow pattern.

3.5.3 Performance of implementation

A Nvidia Tesla C2050 GPU was employed as platform to test the simulation efficiency. Its hardware properties were shown in previous section (Table 3.2). Based on the CUDA `bandwidthTest` utility, the maximum device to device memory bandwidth is 117.93 GB/s.

Figure 3.15 shows the performance of the present implementation under different lattice resolutions. The units of the left y axis are the million lattices updates per second (MLUPS). The right y axis corresponds to the throughput for device to device throughput. The throughputs at different lattice resolutions with respect to the maximum value (117.93 GB/s) range from 44.0% to 52.5%, and the simulation delivers up to 703.31 MLUPS.

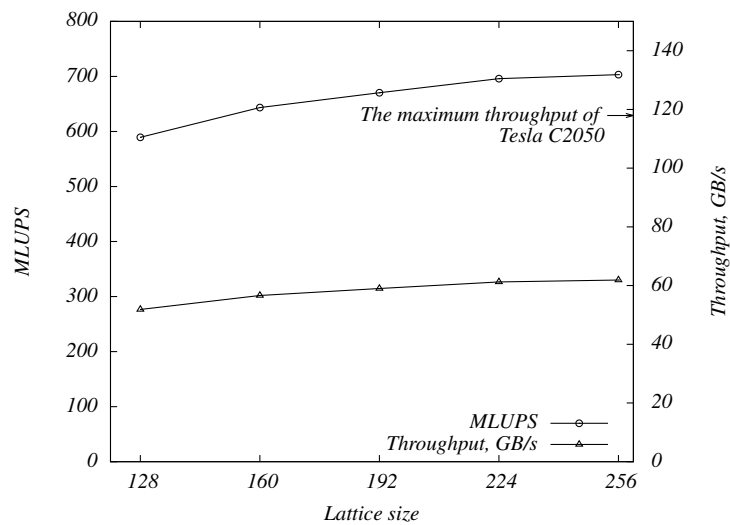


Figure 3.15 – Performance of implementation

3.6 Conclusions and remarks

In this chapter, a highly efficient solver was designed using hybrid LBM to numerically simulate melting process. The LBM with MRT was used to calculate velocity field, and the total enthalpy method was employed to simulate the melting phase change. This solver was optimized in order to perform on NVIDIA GPU based on CUDA architecture (model Tesla C2050).

Experiments carried out in the previous chapter were used to validate the numerical model and its implementation. The present simulation results are in good agreement with our experimental results, as well as the published analytic results. The temperature contours and streamlines were

also presented, which showed that the melting driven by natural convection under high Ra and Pr demonstrated strong convection phenomenon and different characteristics from the previous published results with lower Ra and Pr number (refer to sec. 3.5.2).

The performance tests under different grid resolution showed that the present implementation on the GPU (Tesla C2050) delivered up to 703.31 MLUPS. The device to device data throughput accounted for up to 52.5% of the hardware's maximum throughput. The two dimensional results shows that our solver can provide us quite reliable physical results and considerable calculation efficiency. Since there is not three dimensional simulation results published yet about the melting process, and in order to well profit from our solver's performance, we will expand this solver to simulate the melting in a three dimensional building brick. This composes the content of the next chapter.

3-dimensional simulation results

4.1 Problem proposition

This chapter presents the 3-dimensional simulations of the melting process. This is the successive work of the previous chapter. There are three major motives that persuade us to carry out the 3-dimensional simulation:

Motive 1: We aim to obtain the knowledge of the real melting process (in a 3-dimensional enclosure). There is no published data concerning 3-dimensional melting simulation, only 2-dimensional. Without a high calculation speed solver, the 3-dimensional simulation is a very time-consuming task which also needs a large amount of other computer resources, such as RAM. This might be one of the reasons that there is no published references about the 3-dimensional melting simulation.

Motive 2: At the same time, we expect to provide a batch of 3-dimensional results as references for the other researchers.

Motive 3: Our 2-dimensional simulation was optimized in order to execute on GPU and has been proven high efficient. Therefore, in order to well profit from the GPU calculation power, we'd like to expand our simulation to the 3-dimensional level.

4.2 Preliminary

4.2.1 Hybrid LBM-MRT on the D3Q19 stencil

We use LBM-MRT model with 19 discrete velocities on 3 dimensions, known as D3Q19. This D3Q19 model is the most widely used 3-dimensional model for LBM because it keeps a good balance between isotropy and sim-

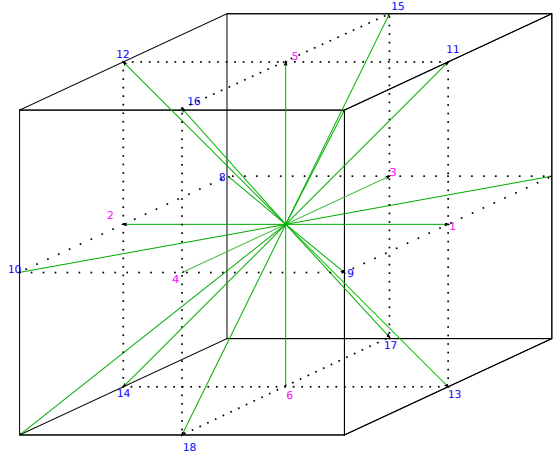


Figure 4.1 – The D3Q19 stencil

plicity. One could refer to Lallemand and Luo's work for more information on the general hybrid model [123].

The 19 discrete velocities are arranged like in Figure 4.1, and the LBM-MRT model is described by Eq. 4.1. The 19 dimensional distributions space $|f_\alpha\rangle$ is mapped to the moment space $|m_\alpha\rangle$ of the same dimension through a linear transformation matrix \mathbf{M} (Eq. 4.2), where \mathbf{M} is shown in d'Humières' paper [122]. This linear transformation makes the collision process move from velocity space to moment space, in which the moments have clear physical properties as follows:

- ⊕ ρ is mass density (zero order moment)
- ⊕ j_x, j_y, j_z are the components of momentum on x, y, z directions respectively
- ⊕ e is the energy (second order moment)
- ⊕ ϵ is the energy square (forth order moment)
- ⊕ q_x, q_y, q_z are the heat flux on x, y, z direction (third order moments)
- ⊕ $p_{xx}, p_{xy}, p_{yz}, p_{zx}$ are the components of the stress tensor
- ⊕ $p_{ww} = p_{yy} - p_{zz}, \pi_{xx}, \pi_{ww}$ (third order moments)
- ⊕ m_x, m_y, m_z are fourth order moments.

$$|f_\alpha(\mathbf{x} + \mathbf{e}\delta t, t + \delta t)\rangle - |f_\alpha(\mathbf{x}, t)\rangle = -\mathbf{M}^{-1} \cdot \mathbf{S} \cdot [|m_\alpha(\mathbf{x}, t)\rangle - |m_\alpha^{eq}(\mathbf{x}, t)\rangle] \quad (4.1)$$

$$|m_\alpha\rangle = \mathbf{M} |f_\alpha\rangle = (\rho, e, \epsilon, j_x, q_x, j_y, q_y, j_z, q_z, 3p_{xx}, 3\pi_{xx}, p_{ww}, \pi_{ww}, p_{xy}, p_{yz}, p_{zx}, m_x, m_y, m_z)^\top \quad (4.2)$$

In Eq. 4.1, the S is a diagonal matrix called collision matrix (Eq. 4.3).

$$S = \text{diag}(s_0, s_1, s_2, s_3, s_4, s_5, s_6, s_7, s_8, s_9, s_{10}, s_{11}, s_{12}, s_{13}, s_{14}, s_{15}, s_{16}, s_{17}, s_{18}) \quad (4.3)$$

Before and after collision, because of the conservation of mass, momentum, and for the simplicity, s_0, s_3, s_5, s_7 are set to 0. The collision factors s_9 and s_1 are controlled by kinematic viscosity ν (Eq. 4.4) and bulk viscosity ζ respectively (Eq. 4.5):

$$\nu = \frac{1}{3} \left(\frac{1}{s_9} - \frac{1}{2} \right) \quad (4.4)$$

$$\zeta = \frac{2}{9} \left(\frac{1}{s_1} - \frac{1}{2} \right) \quad (4.5)$$

The other collision factors, s_2, s_{10}, s_{12} are set to 1.4, s_4, s_6, s_8 to 1.2, and s_{16}, s_{17}, s_{18} to 1.98. s_{13}, s_{14}, s_{15} are equal to s_9 .

Furthermore, in Eq. 4.1, the vector $|m_\alpha^{eq}\rangle$ denotes the equilibrium quantities of the moments. They are calculated by the following set of relations:

$$e^{eq} = -11\rho + 19j^2 + T^* \quad (4.6)$$

$$\epsilon^{eq} = 3\rho \quad (4.7)$$

$$q^{eq} = -\frac{2}{3}j \quad (4.8)$$

$$3p_{xx}^{eq} = 3j_x^2 - j^2 \quad (4.9)$$

$$p_{ww}^{eq} = j_y^2 - j_z^2 \quad (4.10)$$

$$p_{xy}^{eq} = j_x j_y \quad (4.11)$$

$$p_{yz}^{eq} = j_y j_z \quad (4.12)$$

$$p_{zx}^{eq} = j_z j_x \quad (4.13)$$

$$3\pi_{xx}^{eq} = \pi_{ww}^{eq} = 0 \quad (4.14)$$

$$m_x^{eq} = m_y^{eq} = m_z^{eq} = 0 \quad (4.15)$$

The symbol T^* in the equilibrium equation (Eq. 4.6) represents dimensionless temperature derived from energy equation as follows:

$$\frac{\partial T}{\partial t} + \nabla(\mathbf{u} \cdot T) = \alpha \nabla^2 T - S_h \quad (4.16)$$

Where α is the thermal diffusivity, and Boussinesq approximation is applied. The symbol S_h acts as a heat sink and is a quantity related to melting. We will talk about S_h in the next section. So far, the energy equation is then

solved by finite difference as follows (only the gradient on x direction and the Laplace operator are shown):

$$\begin{aligned} \partial_x T &= T(i+1, j, k) - T(i-1, j, k) \\ &- \frac{1}{8} [T(i+1, j+1, k) - T(i-1, j+1, k) + T(i+1, j-1, k) \\ &- T(i-1, j-1, k) + T(i+1, j, k+1) - T(i-1, j, k+1) \\ &+ T(i+1, j, k-1) - T(i-1, j, k-1)] \end{aligned} \quad (4.17)$$

$$\begin{aligned} \nabla^2 T &= 2[T(i+1, j, k) + T(i-1, j, k) + T(i, j+1, k) \\ &+ T(i, j-1, k) + T(i, j, k+1) + T(i, j, k-1)] \\ &- \frac{1}{4} [T(i+1, j+1, k) + T(i-1, j+1, k) + T(i+1, j-1, k) \\ &+ T(i-1, j-1, k) + T(i, j+1, k+1) + T(i, j-1, k+1) \\ &+ T(i, j+1, k-1) + T(i, j-1, k-1) + T(i+1, j, k+1) \\ &+ T(i-1, j, k+1) + T(i+1, j, k-1) + T(i-1, j, k-1)] \\ &- 9T(i, j, k) \end{aligned} \quad (4.18)$$

4.2.2 Modelling for simulating melting

We use the same enthalpy method as that in the previous chapter, which is depicted by Eq. 4.16. The S_h is:

$$S_h = \frac{\partial(L/C_p)}{\partial t} + \nabla \cdot \left(\frac{\mathbf{u} \cdot L}{C_p} \right) \quad (4.19)$$

where C_p is the heat capacity for both liquid and solid, $L = l \cdot \lambda$ is the latent heat content, λ is the latent heat and l is the liquid fraction.

Eq. 4.16 is transformed into the dimensionless form and then discretized by picking the dimensionless values and parameters as described in the previous chapter. Thus the dimensionless form is:

$$\frac{\partial T^*}{\partial t^*} + \nabla^* \cdot (\mathbf{u}^* \cdot T^*) = \frac{\delta t}{\delta^2 x} \frac{1}{\sqrt{Ra}} \nabla^{*2} T^* - \frac{1}{\rho \cdot Ste} \frac{\partial l}{\partial t^*} \quad (4.20)$$

Where the liquid fraction l is defined as follows (T_f is melting temper-

ature of the material):

$$l = \begin{cases} 1 & T^* \geq T_f^* + \frac{1}{\text{Ste}} \\ (T^* - T_f^*) \cdot \text{Ste} & T_f^* < T^* < T_f^* + \frac{1}{\text{Ste}} \\ 0 & T^* \leq T_f^* \end{cases} \quad (4.21)$$

4.3 Implementation

4.3.1 GPU hardware

The GPU employed in the 3-dimensional simulation is not the same model – Tesla C2050 Nvidia GPU – as we used for the 2-dimensional simulation, because the 3-dimensional simulation requires more device memory on the GPU. As a result, we choose to use a Tesla C2075 Nvidia GPU, its global memory capacity is twice bigger than the C2050 model (see [Table 4.1](#)).

Table 4.1 – Specifications of Tesla C2075

CUDA Capability	2.0
Number of SMs	14
Number of CUDA core per SM	32
Constant memory	65536 bytes
Shared memory per block	49152 bytes
Registers available per block	32768
Global memory	<u>6144 MB</u>
Maximum number of threads per SM	1536
Maximum number of threads per block	1024
Maximum dimension of a block	1024 × 1024 × 64
Maximum dimension of a grid	65535 × 65535 × 65535

4.3.2 GPU implementation

4.3.2.1 Algorithm

The algorithm flowchart is shown in [Figure 4.2](#). In this algorithm, the liquid fraction of each lattice is the most critical parameter that controls the flow of the whole simulation process. As a result, as for the calculation domain, there is an excess of logic judgements in order to determine the PCM's phase status. This branching in the GPU simulation process can exert negative impact on the parallel processing performances.

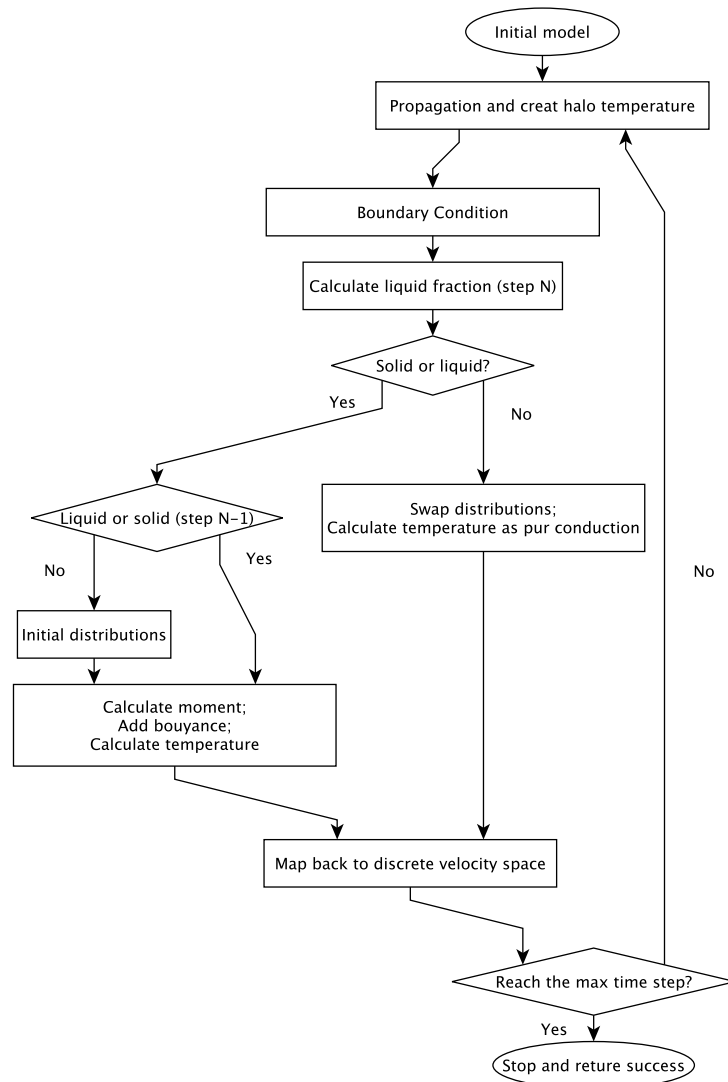


Figure 4.2 – The algorithm for simulation

4.3.2.2 Maximizing the parallelism

The calculation lattices topology should be mapped to GPU's *grids* in such a way that each *thread* takes care of one lattice in the calculation domain. This assures a possible thread-level parallelism [125, 129]. Besides, the unit size of a *warp* has 32 *threads*. In a situation that *threads* in a *warp* encounter a logic code branch or a non aligned lattice calculation domain, several *threads* will be forced inactive. As a result, the code must be well designed to prevent unnecessary code branching, the lattices size should be chosen as the multiple of the size of a *warp* as well. Those suggestions ensure a max threads occupancy.

4.3.2.3 Decreasing the memory accessing latency

The *kernels* can access several types of memory space equipped on GPU. Generally, the bigger the quantity of memory, the slower the reading and writing speed, and vice versa. For example, the global memory is quantitatively abundant but has the lowest accessing speed, whereas the shared memory and register have small memory quantities but very fast speed. Furthermore, *threads* retrieve data from memory by the unit of half-warp, which signifies that the information used to perform simulation should be stored on the memory in a successive and well aligned manner. The more scattered the data, the less efficient the access.

In global memory, for each lattice, 19 velocities plus 1 temperature plus 1 liquid fraction request memory space. Those variables can be easily arranged by the unit of each lattice. However, this could cause considerable useless memory transactions. As a result, in this simulation, those 21 variables are stored by the unit of the size of the x direction of calculation domain.

The 19 discrete velocities and 1 liquid fraction are fetched and stored in the local registers before performing the calculation. The temperature field is solved by 19-points finite differences (Figure 4.3). To obtain each lattice's temperature on time step N , the 19 temperatures' information on time step $N-1$ must be accessed beforehand. This causes plenty of memory accesses and thus dramatically impacts the overall performance. Besides, those 19 temperatures must be well addressed in memory so that they can be accessed easily. In this simulation, the shared memory is chosen to store the temporary temperatures of the previous time step. One thing needing to be mentioned is that the shared memory is only available in its own *block* and blind to the other blocks, so *blocks* must be assigned as single dimension (LX in Figure 4.3). Furthermore, there is no mechanism so far from CUDA C that can prevent the *threads* within a *block* from access synchronization, therefore it is the programmers' responsibility to synchronize the

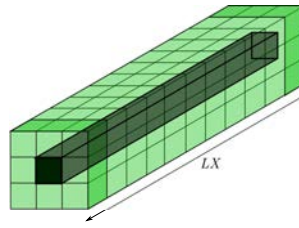


Figure 4.3 – Halo temperature arrangement

threads' accesses.

4.3.2.4 Boundary conditions

The simulation boundary conditions are shown in Figure 4.4. All the simulation parameters are listed in Table 4.2 as dimensionless form. We chose the halfway bounce back scheme to apply the LBM boundary conditions. The temperatures are applied on the western ($T_w^* = +1$) and eastern sides ($T_e^* = -1$), and the other four sides are kept adiabatic.

Because the temperatures are applied in the middle of two lattices, the halo temperatures used to calculate the temperatures of the boundary lattices are created first in shared memory and released after. This would lead to no extra data writing and thus enhance the performance. For the western and eastern wall, the halo temperatures are:

$$T_{-1} = \frac{8T_w - 6T_0 + T_1}{3} \quad (4.22)$$

For the boundary lattices on the adiabatic sides, the halo temperatures are:

$$T_{-1} = \frac{21T_0 + 3T_1 - T_2}{23} \quad (4.23)$$

4.4 Results

The grid dependence of the 3-dimensional numerical model is presented in the first place, then followed by the sections with regard to the simulation results, which cover the features of natural convection flow (Sec. 4.4.2), heat transfer (Sec. 4.4.3 and 4.4.4) as well as the solid-liquid interface evolution (Sec. 4.4.5). The simulations are carried out with Rayleigh number $Ra = 2.48 \times 10^8, 10^6, 10^7, 10^8$ and $Pr = 50$. The last subsection provides the GPU implementation performance of the 3-dimensional simulation (Sec. 4.4.7).

In order to inspect the 3-dimensional simulation results, we analyse the data on four typical cross-sections, three of which are perpendicular to the

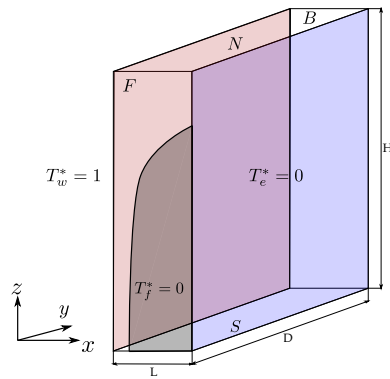


Figure 4.4 – Calculation domain

Table 4.2 – Simulation cases

Ra	Pr	Ste	T_w^*	T_e^*	T_f^*	H	L	D
2.48×10^8	50	0.072	1	0	0	1	0.20	1
10^8								
10^7								
10^6								

y-axis at $y = 0.25, 0.5$ and 0.75 and the fourth one is perpendicular to the x-axis at $x = 0.1$. Four indexes are used to identify them, say, S1 to S4. What's more, on each cross-section, the data on three lines are analysed as well. Those lines are indexed by adding a secondary index to the cross-section's index, such as L-S1-1, L-S1-2 and so on (see Figure 4.5)

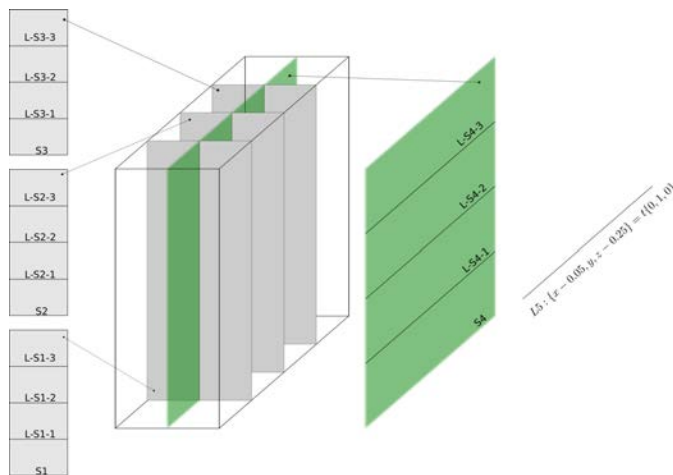


Figure 4.5 – The dispositions of the cross-sections, lines and their indexes

4.4.1 Grid dependence

Table 4.3 shows the Nusselt number values at different mesh resolutions. Their relative errors comparing to the mean value are shown in Figure 4.6.

Table 4.3 – The values of Nusselt number at different mesh resolutions. When $Ra = 10^7, t = 1500s$

The mesh resolution of the z-direction	128	160	192	224	256	320
Nu	18.221	18.138	18.038	18.007	18.010	18.103

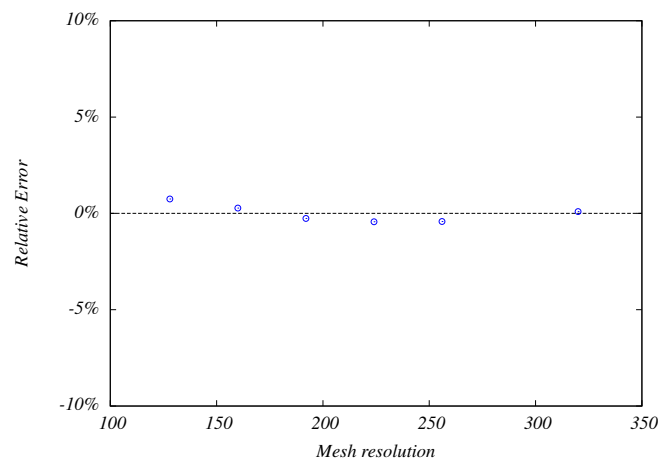


Figure 4.6 – The relative errors of Nusselt number. (when time $t = 1500s$, compared with the mean value and the Rayleigh number $Ra = 10^7$)

4.4.2 Velocity fields

4.4.2.1 Isosurfaces of the velocities' components

Figure 4.7a is the isosurface of u_x (velocity component on x direction) when $Ra = 2.48 \times 10^8$ and $\tau = 0.00312$ (5000s). In the upper part of the cavity, there is the fluid movement from the western wall to the solid-liquid interface. Moreover, we observe that, where the flow is close to the solid-interface, the isosurface of u_x has several depressions. This is caused by the vortices at those positions (refer to the coming sections). Figure 4.7c is the isosurface of u_z , which clearly shows that the convective flow on the hot and cold sides. From the isosurface of u_y , we could note that in the vicinity of the solid-liquid surface, there exists the flow along the y -direction, see Figure 4.7b. Since western and eastern sides are the only two sides on

which the temperatures are applied, this y-component of the flow velocity maybe demonstrate that the melting under this configuration is no longer a 2-dimensional process or maybe is just calculation errors introduced by the hardware restrictions due to the single precision arithmetic on the GPU employed. All the detailed analysis of the velocities will be presented in the following sections.

4.4.2.2 Velocities' profiles on the cross-sections S1 S2 and S3

The Figure 4.8 shows the streamlines on the three cross-sections: S1, S2 and S3, besides, the 2-dimensional simulation results is also presented here for comparison. We can see at least four vortices between $0.30 \leq y \leq 0.65$ in all the three cross-sections of the 3-dimensional results (see Figure 4.8a, Figure 4.8b and Figure 4.8c). Those vortices mainly appear on three levels along z direction, which are $z = 0.35, 0.50$ and 0.60 . We can also notice that the streamlines on the three cross-sections have an extremely similar vortices pattern. The impacts from the front and back walls on the flow cannot reach the cross-sections S1 and S3.

Compared to the 2-dimensional simulation results, the streamlines of the 2-dimensional simulation have a set of very similar vortices patters - both their relative and absolute positions- as the 3-dimensional results, in spite of very slightly differences on the central vortex(see Figure 4.8d).

4.4.2.3 Velocities' characteristics along the lines

Figure 4.9, Figure 4.10 and Figure 4.11 are the velocities' components along the lines in the cross-sections S1, S2 and S3 respectively. They are orthogonal to the yz coordinate surface.

As for the three lines located at the same positions of the three different cross-sections, the velocities' x and z components possess the same distributions and magnitude. The x-components of the velocities are almost zero when far from the solid-liquid interface. Due to the oblique angle between the solid-liquid interface and the x-direction, the natural convection flow has a negative x-component of the velocity in the vicinity of the solid-liquid interface (see Figure 4.9a, 4.10a and 4.11a).

The velocities have quite small y-components compared to the x- and z-components (see Figure 4.9b, 4.10b and 4.11b).

The z-components have the largest magnitudes of the velocities. We can observe visible positive values along the enclosure's western wall and negative values along the eastern wall as well as the solid-liquid interface. In addition, the flow moves slightly faster on the hot side than on the cold side. Moreover, on the hot side, the convective flow in the middle of the enclosure is stronger than the flow in the upper part and the lower

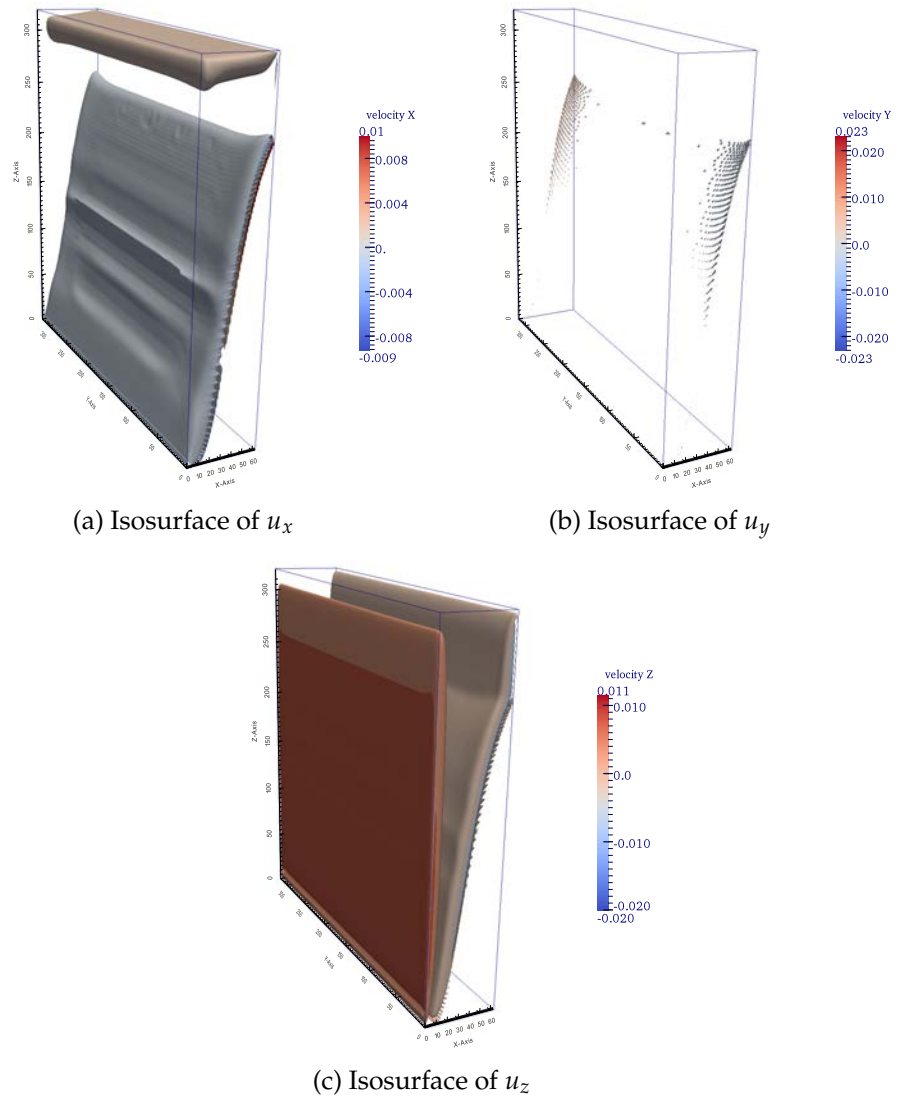
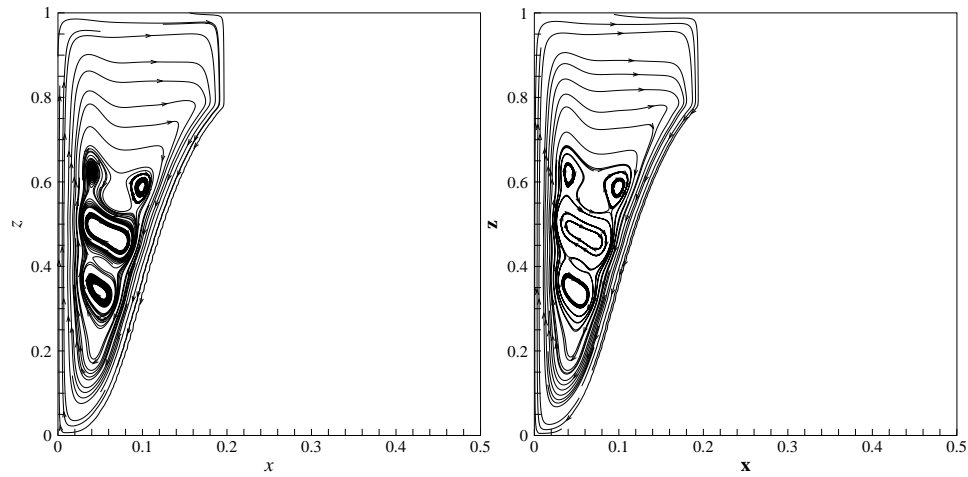
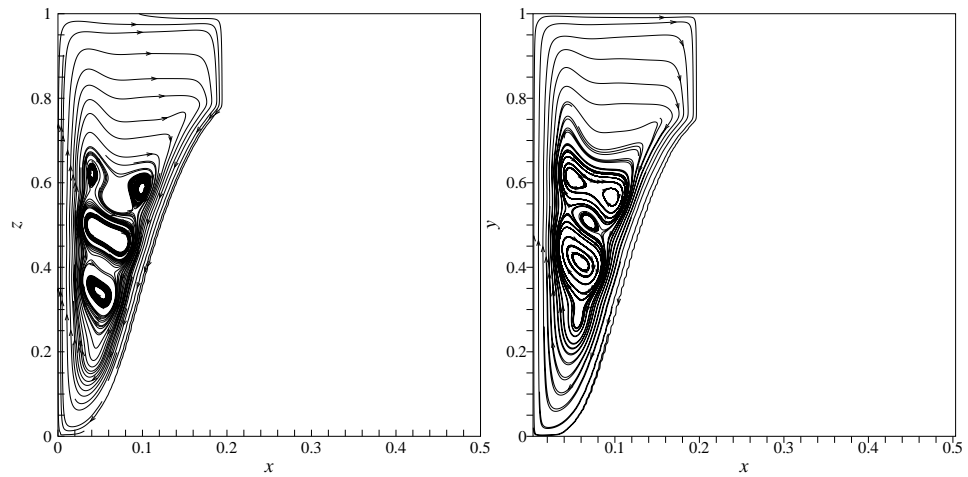


Figure 4.7 – Isosurfaces of the velocity components when $Ra = 2.48 \times 10^8$ and $\tau = 0.00312$ (5000s)



(a) The cross-section S1

(b) The cross-section S2



(c) The cross-section S3

(d) The 2-dimensional simulation results

Figure 4.8 – Streamlines on the cross-sections: S1, S2 and S3. When $Ra = 2.48 \times 10^8$ and $\tau = 0.00312$ (5000s)

part. This is because the flow in the middle is well developed, whereas on the lower and upper part, the flow reaches the boundary (see Figure 4.9c, 4.10c and 4.11c). Transformed to the physical quantities, on the hot side, the z-components have an approximate value of 2.20 mm/s in the middle, 1.71 mm/s in the upper part and 1.94 mm/s in the lower part. On the cold side, the approximate largest value is -2.13 mm/s.

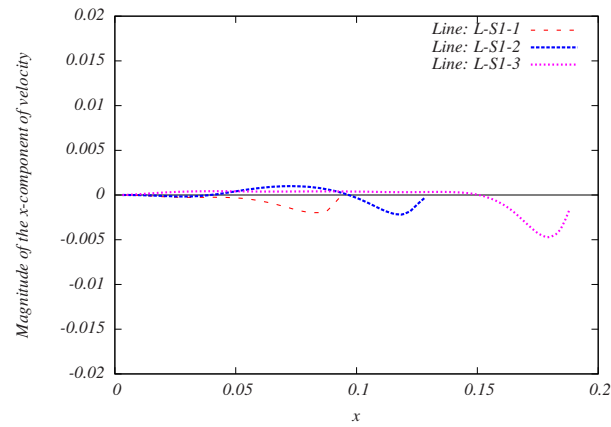
In order to understand the symmetrical characteristics of the 3-dimensional simulation, the velocities' distributions along the three lines which are parallel with the y-axis and in the cross-section S4 are shown in Figure 4.12. Additionally, the velocity distribution along the line $\{x - 0.05, y, z - 0.25\} = t\{0, 1, 0\}$ (L5) is also presented (see Figure 4.13), because the line L-S4-1 goes through the solid phase. Generally speaking, the velocities along the y-axis direction have much smaller quantities than their counterparts along the x-, z-axis directions.

The line L-S4-1 goes through the solid phase, as a result, all the three components of velocity are zero. From the velocity distributions of the lines L-S4-2 and L-S4-3, we can see a very obvious symmetrical velocities' distribution along the y-axis direction on the bottom and upper parts (see Figure 4.12b and Figure 4.12c). Besides, we can also observe that the front and back walls do impose some effects on the flow. The impacts decrease when the y coordinate approaches the center of the enclosure. Approximately when $0.19 \leq y \leq 0.81$, the impacts of the boundary walls are not significant any more, which means the ratio of $\frac{H}{D}$ must be roughly bigger than 1.61 in order to remove the impacts from the boundaries.

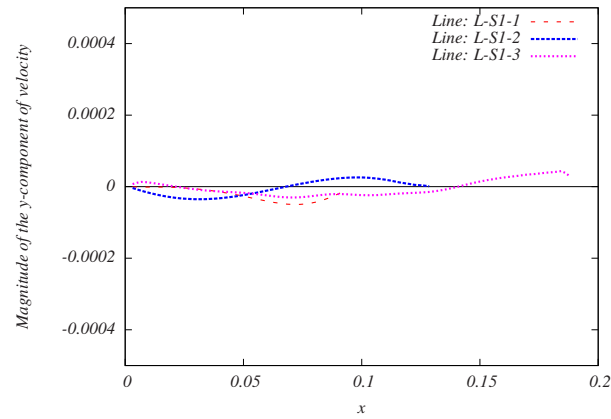
Additionally, if we scale up the figure about the velocity distribution along the line L5 which is quite near the bottom of the flow. From Figure 4.13 we can notice that the velocities' distribution of y-component is inverse symmetrical. This demonstrates that the natural convection in the lower part of the enclosure has somewhat 3-dimensional flow characteristics. In spite of it, the magnitudes of the velocities' y-components are not largely comparable to the x- and z-components. In a way, the flow on the y-direction is not very significant. The 3-dimensional flow characteristics exists but not considerably obvious. As a conclusion, if $\frac{H}{D} \geq 1.61$, the melting process can be roughly considered as a 2-dimensional process.

4.4.3 Temperature distribution

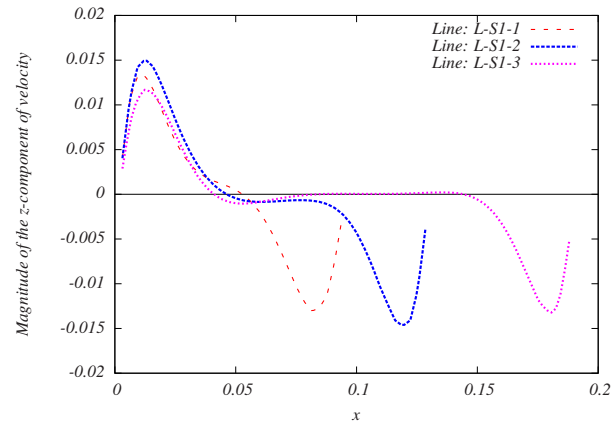
The Figure 4.14 shows the temperature isosurfaces of the 3-dimensional simulation when $Ra = 2.48 \times 10^8$ and $\tau = 0.00312$ (5000s). The temperature stratification is prone to become parallel to the horizontal direction on the top part of the flow due to the natural convection. The natural convection dramatically modifies the solid-liquid interface compared to the melting process driven by the pure conduction. Besides, the adiabatic walls



(a) x-component

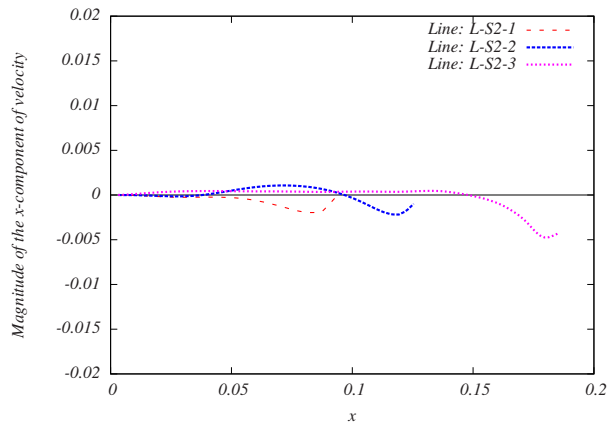


(b) y-component

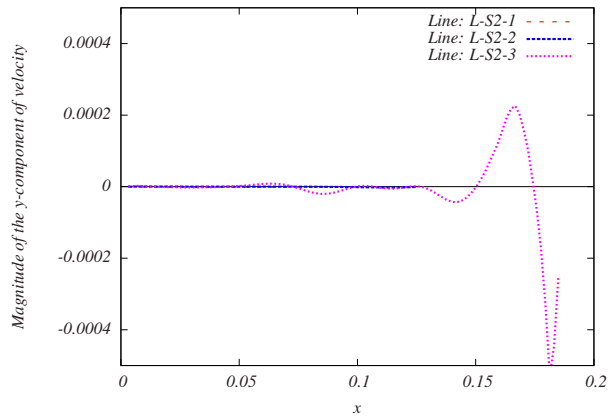


(c) z-component

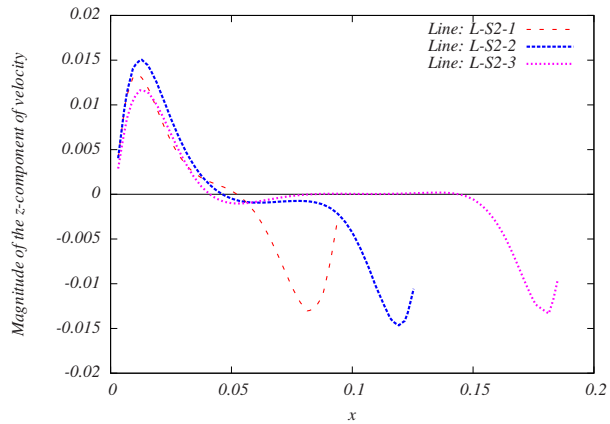
Figure 4.9 – The velocity components on the lines L-S1-1, L-S1-2 and L-S1-3. When $Ra = 2.48 \times 10^8$ and $\tau = 0.00312$ (5000s)



(a) x-component

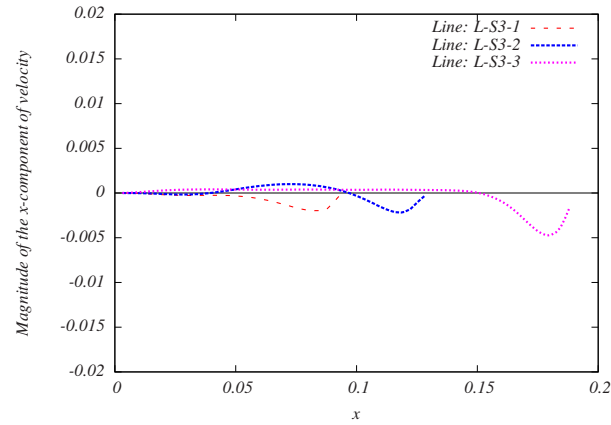


(b) y-component

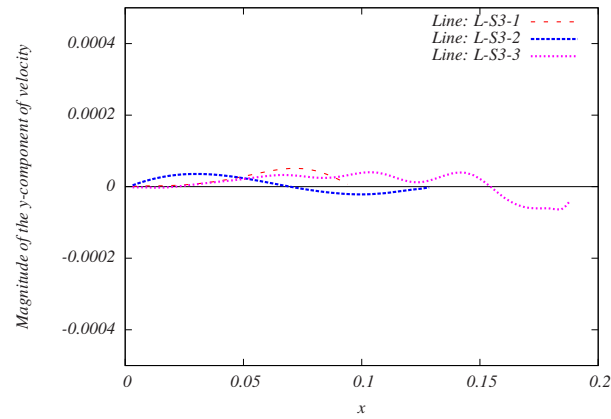


(c) z-component

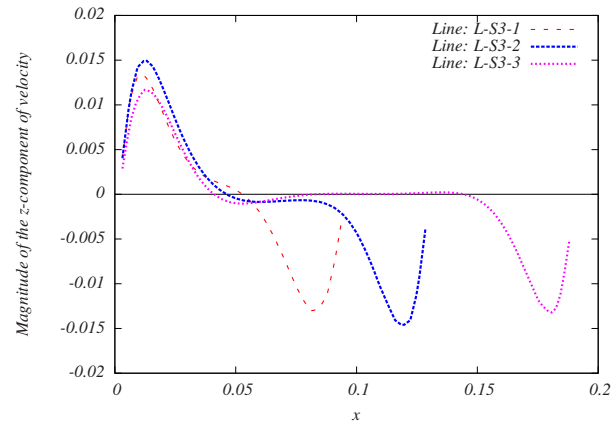
Figure 4.10 – The velocity components on the lines L-S2-1, L-S2-2 and L-S2-3. When $Ra = 2.48 \times 10^8$ and $\tau = 0.00312$ (5000s)



(a) x-component

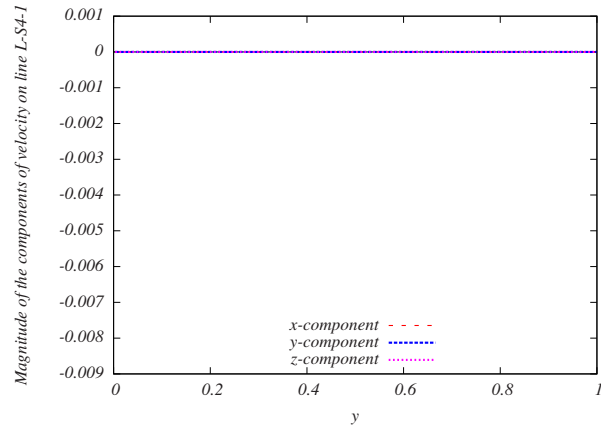


(b) y-component

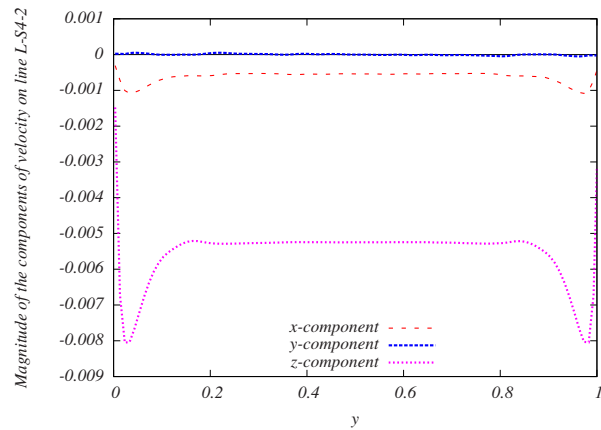


(c) z-component

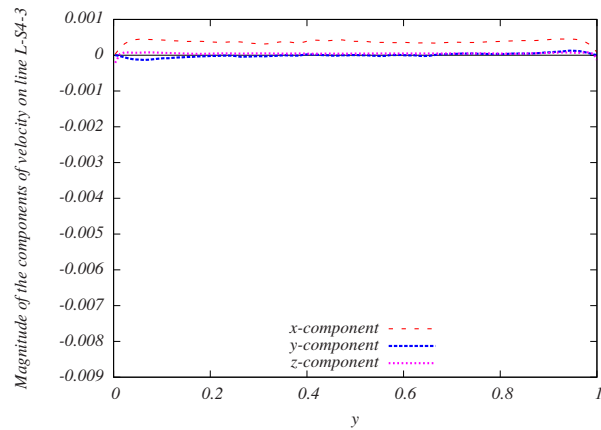
Figure 4.11 – The velocity components on the lines L-S3-1, L-S3-2 and L-S3-3. When $Ra = 2.48 \times 10^8$ and $\tau = 0.00312$ (5000s)



(a) On the line L-S4-1



(b) On the line L-S4-2



(c) On the line L-S4-3

Figure 4.12 – The velocity components on the lines L-S4-1, L-S4-2 and L-S4-3. When $Ra = 2.48 \times 10^8$ and $\tau = 0.00312$ (5000s)

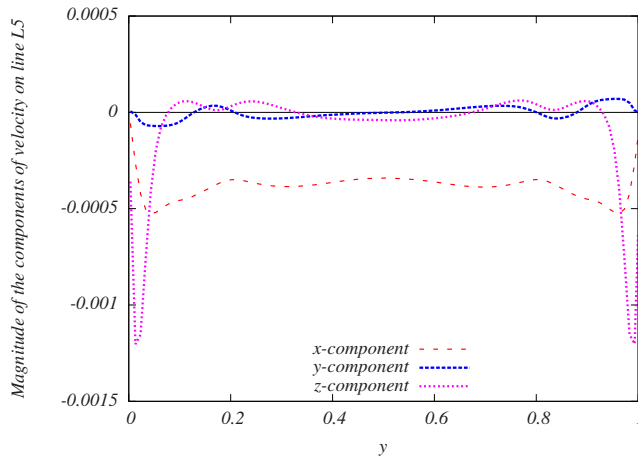


Figure 4.13 – The velocity components on the line L5. When $Ra = 2.48 \times 10^8$ and $\tau = 0.00312$ (5000s)

have some impacts on the shape of the temperature stratification.

The temperature contours on the three cross-sections S1, S2 and S3 are presented in Figure 4.15. As a comparison, the 2-dimensional simulation results is also displayed. Like the the streamlines presented in the previous section, the three sets of contours in the cross-sections S1, S2 and S3 also have almost the same pattern. Compared to the 2-dimensional results, the 3-dimensional temperature contour lines are less distorted in general, especially within the vertex region. Besides, we observe that the 3-dimensional simulation has a slightly bigger temperature gradient on the z-direction than the 2-dimensional simulation.

4.4.4 Heat transfer rate

The heat transfer rate on the high temperature western side is described in the form of average Nusselt number, which is calculated by the following equation (Eq. 4.24):

$$Nu = - \int_0^1 \int_0^1 \frac{\partial T^*}{\partial x^*} dy^* dz^* \quad (4.24)$$

The Figure 4.16 presents the evolution of Nusselt number related to the dimensionless time. The 3-dimensional simulation result, 2-dimensional simulation result, the experiment result and the analytical result are all displayed. We can see that our 2-dimensional and 3-dimensional simulations have quite the same Nusselt number evolutions, although the 2-dimensional simulation is very slightly bigger than the 3-dimensional simulation.

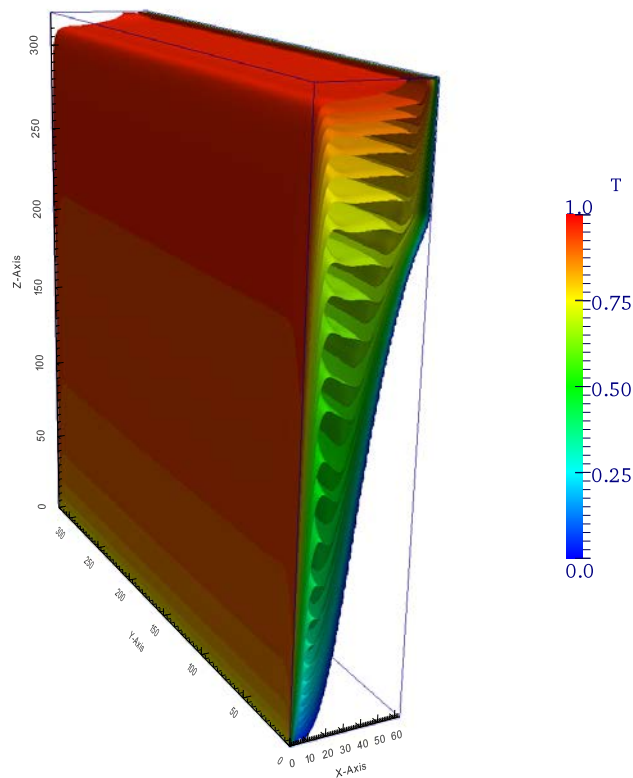


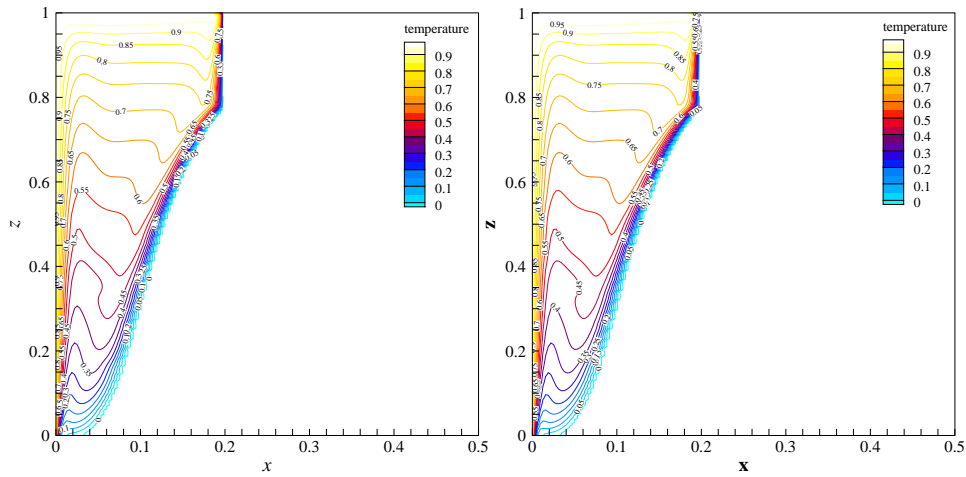
Figure 4.14 – The temperature isosurfaces in the 3-dimensional simulation. $Ra = 2.48 \times 10^8$ and $\tau = 0.00312$ (5000s)

We also observe that during the early period, the simulation results have some oscillations. This is due to the intrinsic characteristic of the enthalpy method and the LBM, the velocities in the lattices which are close to the solid-liquid interface have sharp changes. In such simulation, the grids switch their solid-liquid phases sharply, which can introduce an inconsistency of the velocity of the grids encountering the phase change in the vicinity of the solid-liquid interface.

4.4.5 Solid-liquid interface

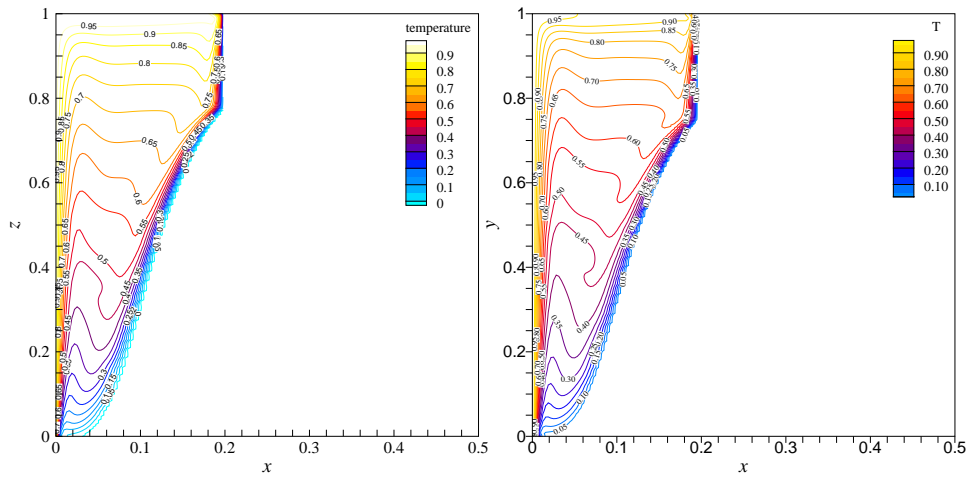
The [Figure 4.17](#) presents the solid-liquid interface position at the moment $\tau = 0.00312$ (5000s) of the 2-dimensional and 3-dimensional simulations. A very nice overlap of the two curves is obtained.

The [Figure 4.18](#) is the sequential images of the melting process. As analysed in previous chapter, the melting undergoes four stages, from [Figure 4.18](#), we can again observe the transition of the four stages. Besides, the natural convection really has great impacts on the melting process inside



(a) The cross-section S1

(b) The cross-section S2



(c) The cross-section S3

(d) The 2-dimensional simulation results

Figure 4.15 – The contours of temperature on the cross-sections: S1, S2 and S3. When $Ra = 2.48 \times 10^8$ and $\tau = 0.00312$ (5000s)

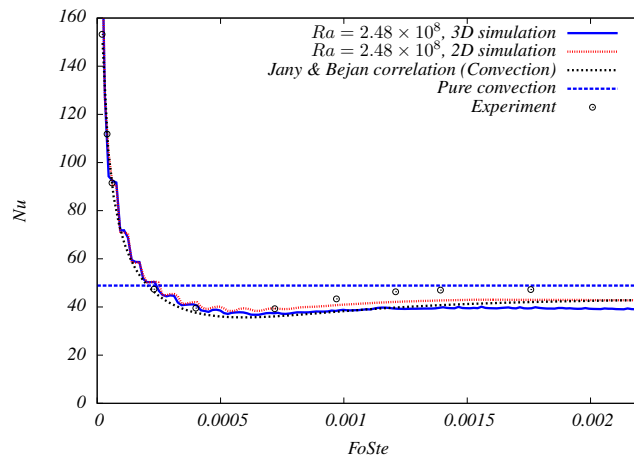


Figure 4.16 – The Nu number temporal evolution. The $Ra = 2.48 \times 10^8$ and $\tau = 0.00312$ (5000s)

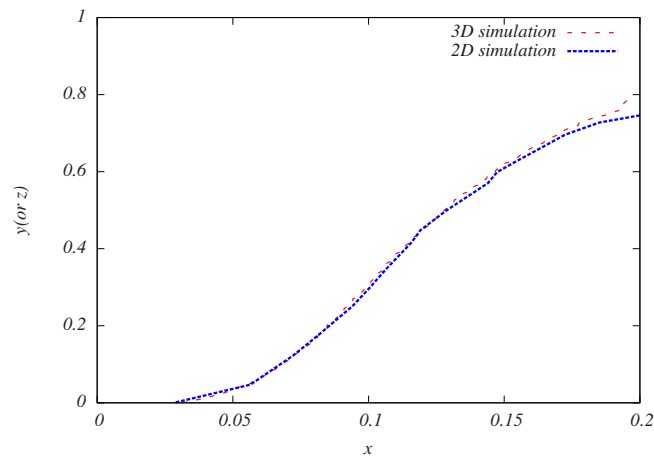


Figure 4.17 – The solid-liquid interface at instant $\tau = 0.00312$ (5000s): 2-dimensional and 3-dimensional simulations. ($Ra = 2.48 \times 10^8$)

the brick.

4.4.6 Melting under different Rayleigh numbers

This section presents the melting process under different Ra numbers. Three extra cases are simulated, which are $Ra = 10^6$, 10^7 and 10^8 . The Figure 4.19 shows all the Nu number evolution curves under different Ra numbers. Additionally, the 2-dimensional simulation result when $Ra = 2.48 \times 10^8$ is also presented. The Figure 4.20, Figure 4.21, Figure 4.22 and Figure 4.16 are curves that present both our simulation results and the analytical results.

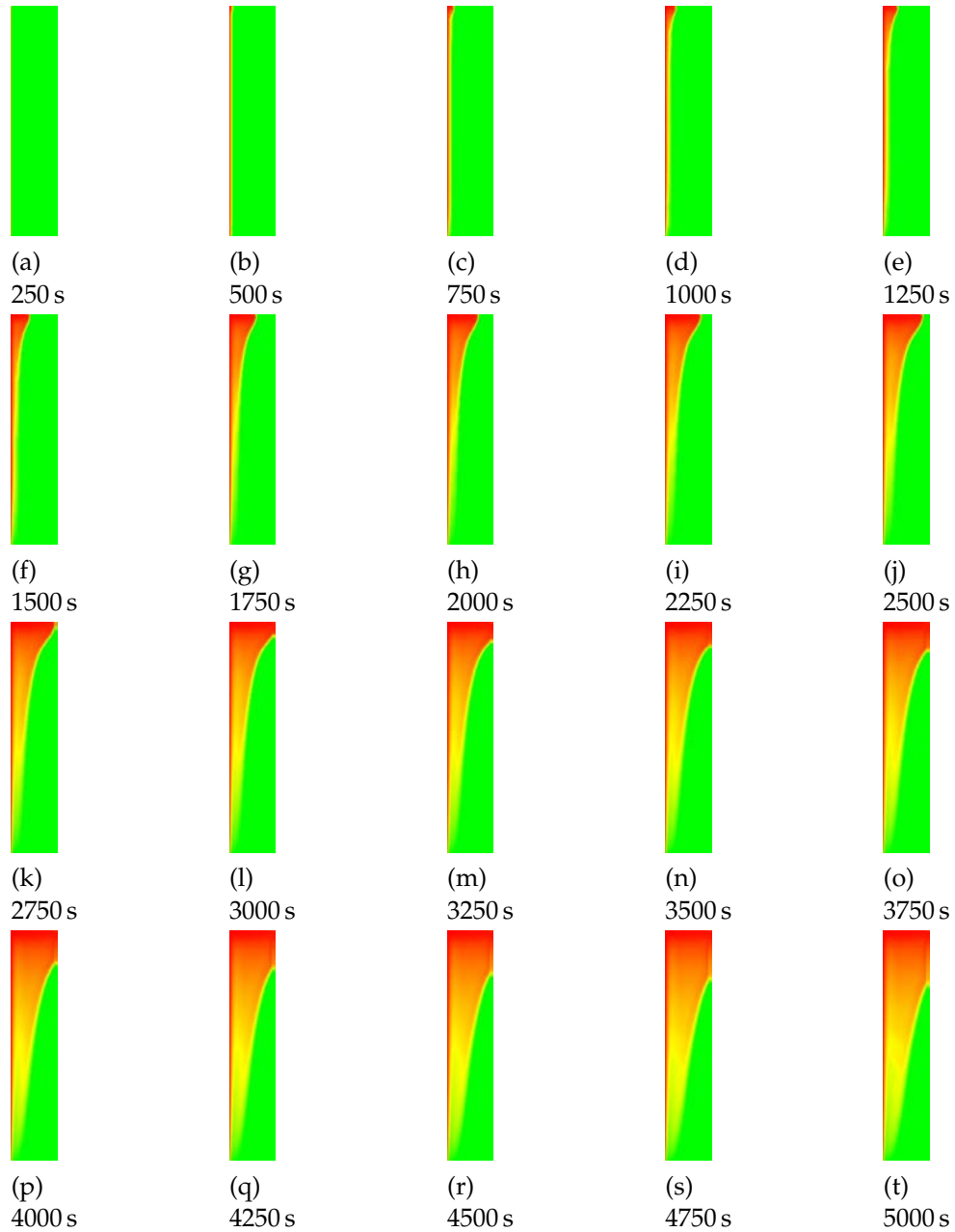


Figure 4.18 – The melting process when $Ra = 2.48 \times 10^8$.

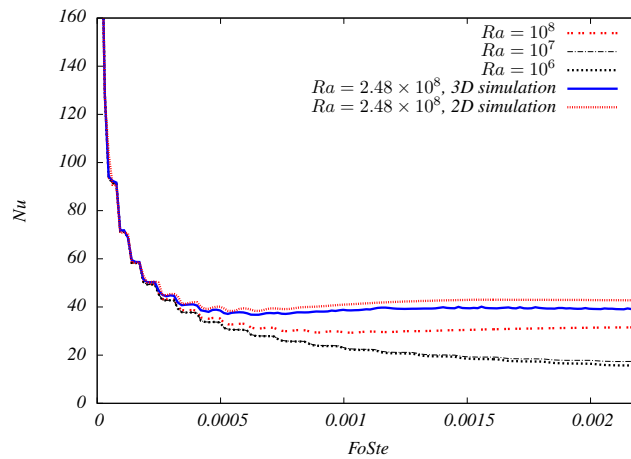


Figure 4.19 – The average Nu number of the heating wall at different Ra numbers

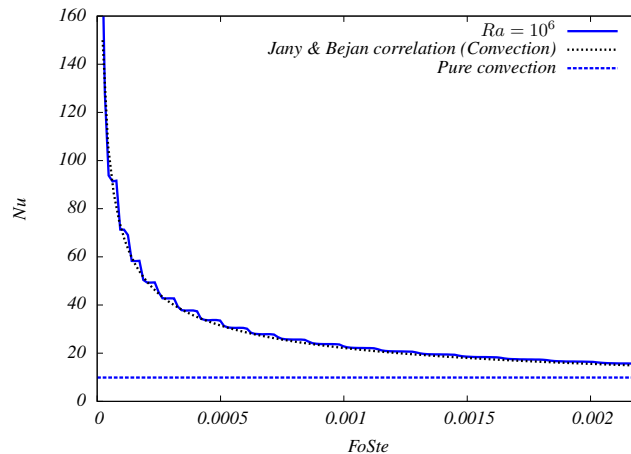


Figure 4.20 – The average Nu number of the heat wall and the analytical results from [54] when $Ra = 10^6$

From Figure 4.19 we can notice that at the initial stage of the melting (more precisely before the $FoSte$ reaches 0.0002), the five curves almost overlap with each other, notably, when $FoSte$ is less than 0.0001, they are identical. This is because at the very beginning, the heat transfer is dominated by the pure conduction, so the Rayleigh number has a negligible impact on the melting process. When $FoSte$ is between 0.0001 and 0.0002, the convection starts to appear but with a small intensity as against the conduction. This short period could be named competitive period. With the melting going on, the convection dominates and thus leads to the five curves divergence and finally reach a stable value.

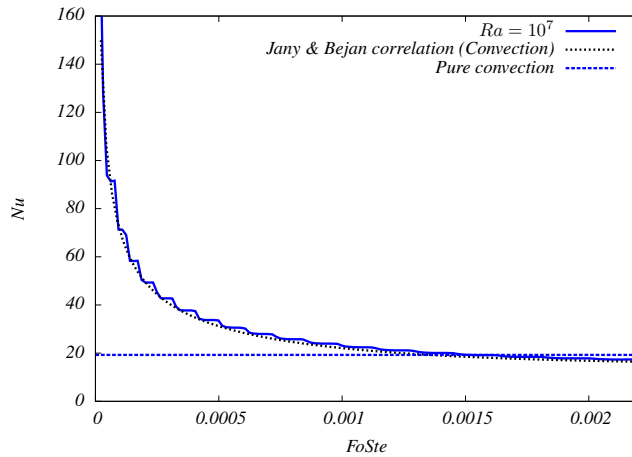


Figure 4.21 – The average Nu number of the heat wall and the analytical results from [54] when $Ra = 10^7$

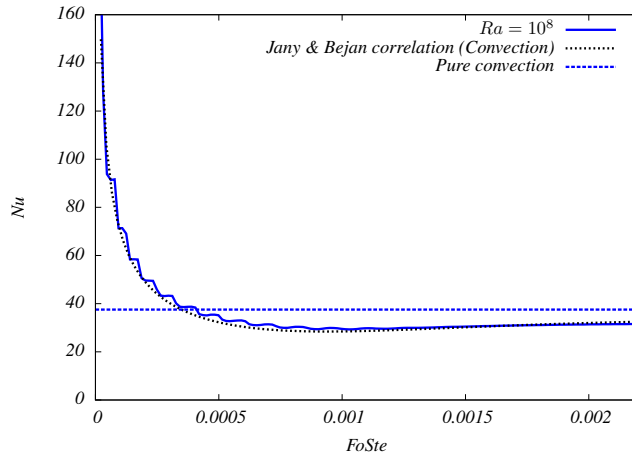


Figure 4.22 – The average Nu number of the heat wall and the analytical results from [54] when $Ra = 10^8$

Figure 4.19 also makes it clear that the bigger the Ra is, the higher the heat transfer rate is. Besides, when $Ra = 10^7$ and 10^6 , the natural convection has almost the same impacts on the melting process.

By comparing the analytical results [54] and our simulation results (see Figure 4.20, Figure 4.21, Figure 4.22 and Figure 4.16), we find that the Nu numbers of the numerical simulations in generally agree fairly well with the analytical results. With the melting going on, the Nu numbers have the same decreasing patterns as the analytical ones. When the melting processes become steady, the simulation results have very small differences comparing to the analytical results. In addition, after the convection be-

comes steady and dominant, when $Ra = 10^7$, the heat transfer rate is very close to the pure convection values, whereas when $Ra > 10^8$, the heat transfer rates are slightly smaller than the pure convection heat transfer rate.

The Figure 4.23, Figure 4.24, Figure 4.25 and Figure 4.18 show the melting processes at 20 successive instants when Ra equals 10^6 , 10^7 , 10^8 and 2.48×10^8 respectively¹. Once more, we could observe that, at the beginning of the melting, the heat transfer form is the pure conduction and that gradually the melted liquid volume enlarges. As soon as there is enough cavity for the melted PCM, the liquid starts to have a vertical movement because of the buoyancy force caused by the temperature gradients. Since the relative high temperature liquid moves to the top, the melting interface retreats faster than the bottom part. As contrast, near the bottom part of the interface, there is no noticeable liquid movement, so the heat transfer is mainly controlled by conduction. Thus, the lower part of the interface is closer to the cold wall than the upper part of the interface. Furthermore, the melting develops faster when $Ra \geq 10^8$ than the cases with lower Ra numbers.

4.4.7 Implementation performance

The simulation performance are illustrated by million lattices updates per second (MLUPS) and device to device memory throughout (GB/s). The maximum memory data throughout of Tesla C2075 GPU is listed in Table 4.4.

As shown in Table 4.5, the average performance shows that the current GPU simulation has 56.46% of the maximum data throughput ability and 402.2 MLUPS. Compared to our previous two dimensional solver, the current simulation has a smaller MLUPS but a bigger data throughout. Above all, both of them have significant high performances.

1. Click [here](#) to access a video of melting of the 3-dimensional simulation ($Ra = 10^8$)

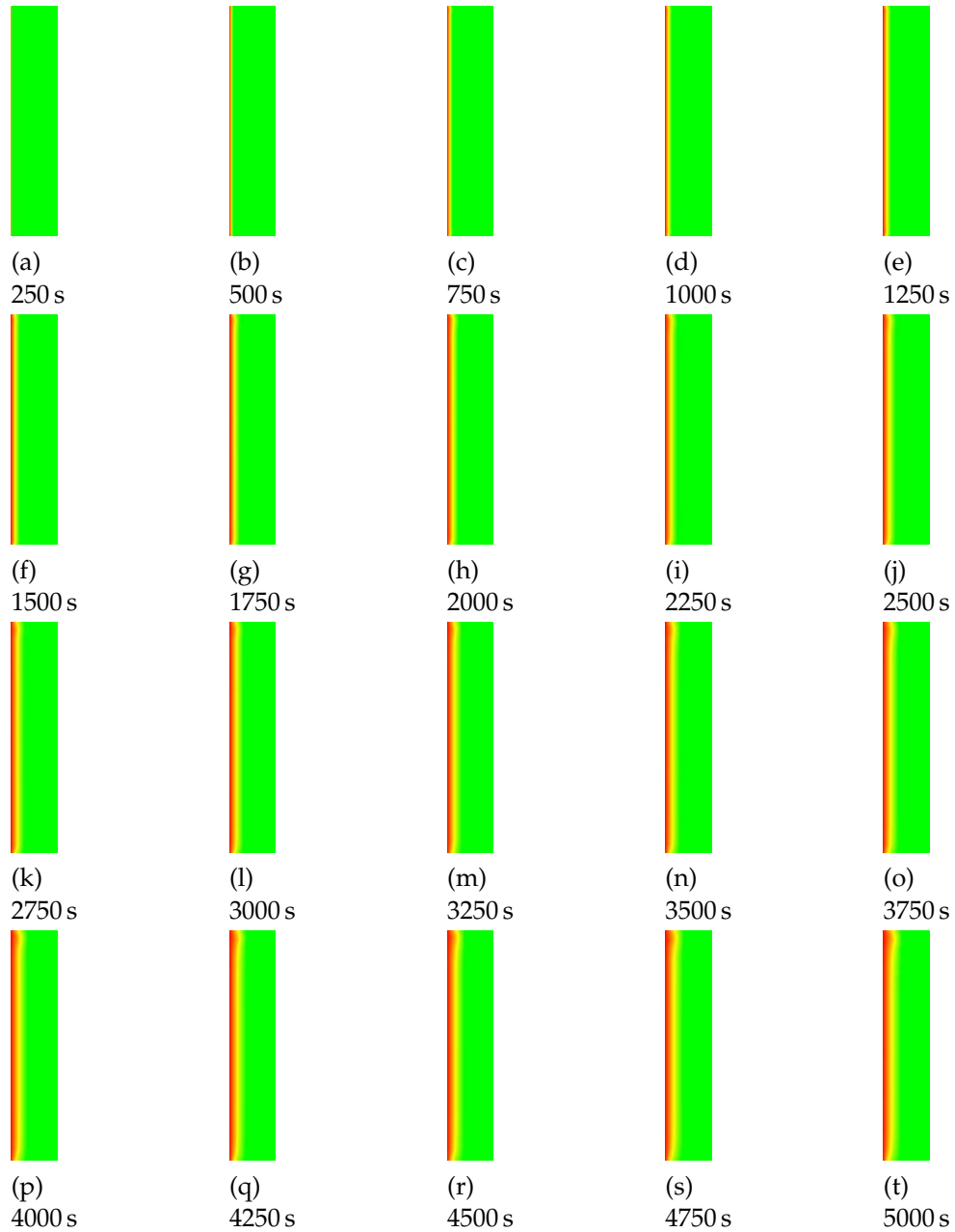


Figure 4.23 – The melting process when $Ra = 10^6$.

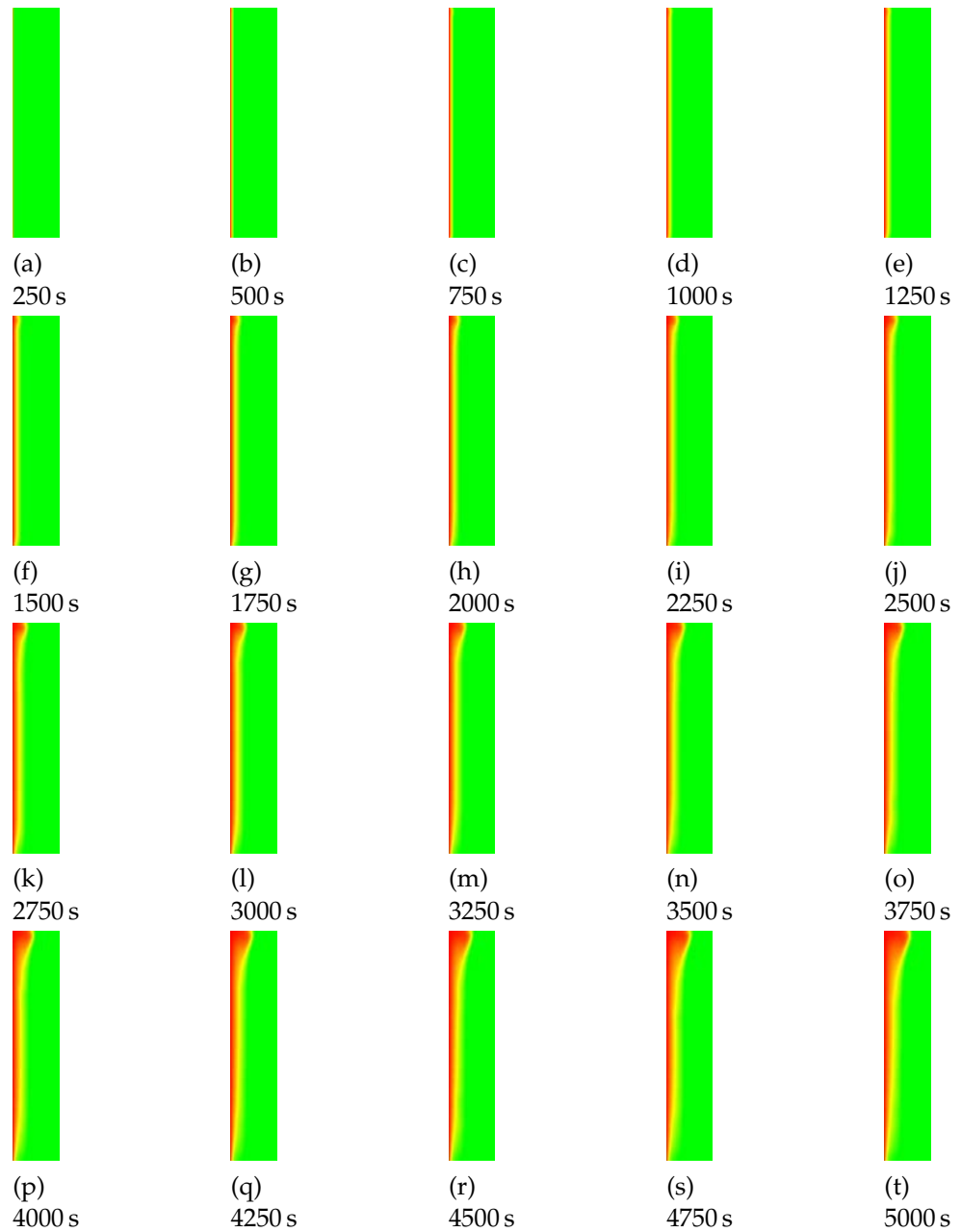


Figure 4.24 – The melting process when $Ra = 10^7$.

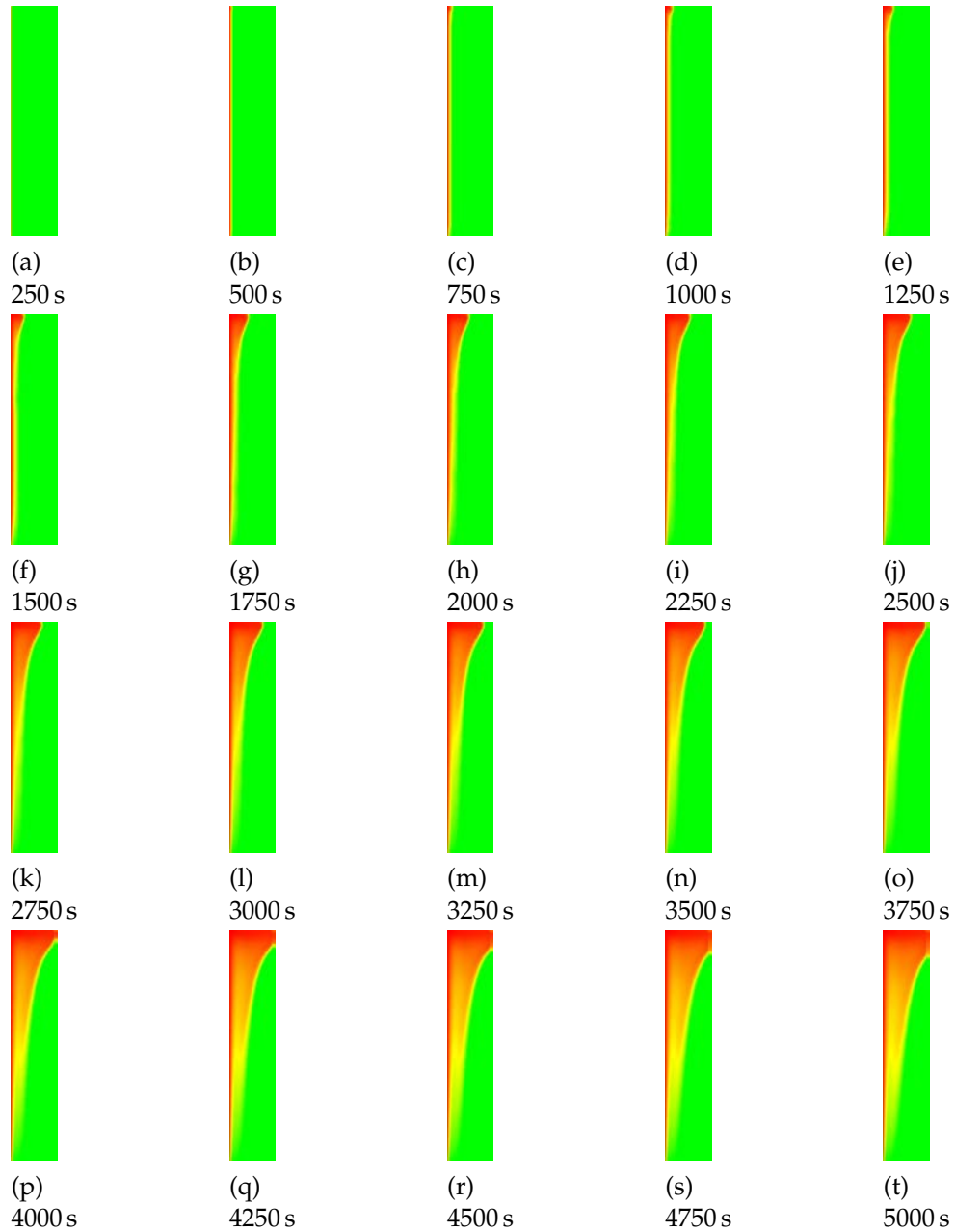


Figure 4.25 – The melting process when $Ra = 10^8$.

Table 4.4 – Band width of Nvidia Tesla C2075 GPU

Band width, GB/s		
Host to device	Device to host	Device to device
5.726	6.237	119.692

Table 4.5 – Performance of simulation

Current simulation performance on Tesla C2075 Nvidia GPU (3D)						
Ra	Mesh resolution on z-direction	MLUPS	Memory throughput, GB/s	Comparing to maximum throughput		
10^6	320	397.0	66.7	56.83 %		
10^7	320	401.4	67.4	56.34 %		
10^8	320	404.9	68.0	67.66 %		
$2.45 \cdot 10^8$	320	405.6	68.1	56.93 %		
Average		402.2	67.6	56.46 %		
Simulation performance on Xeon X5472 CPU (2D) [130]						
-	150	10.68	-	-		
Our previous GPU simulation on Tesla C2050 Nvidia GPU (2D) [131]						
-	128	589.32	51.9	32.98 %		
-	256	703.31	61.89	52.48 %		

4.5 Conclusions

In this chapter, we extend our 2-dimensional solver to simulate the melting process driven by natural convection in the 3-dimensional transparent brick. The brick's western and eastern sides are applied fixed temperatures and the other sides are adiabatic. The D3Q19 LBM-MRT model is used to solve the natural convection. The enthalpy method is chosen to obtain the temperature distribution during the melting progress, and its mathematical equation is solved by finite difference.

We firstly simulated the same condition - $Ra = 2.48 \times 10^8$ - as the one in the 2-dimensional simulation and the experiment. Through comparing to the 2-dimensional simulation results, we found that the streamlines of the 3-dimensional simulation have a set of very similar vortices patterns - both their relative and absolute positions - as the 2-dimensional results, in spite of very slightly differences on the central vortex.

From the velocity distributions along the characteristic lines which are orthogonal to the yz coordinate surface we found that, on the x -direction and at the same height level inside the brick, the velocities' x and z components possess the same distributions and magnitude. The z -components have the largest magnitudes of the velocities, which is obvious due to the natural convection. The natural convection on the hot side is stronger than on the cold side when there is the solid-liquid interface. Moreover, the natural convection in the middle of the brick is stronger than the bottom part and the upper part. On the hot side, the z -components have an approximate value of 2.20 mm/s in the middle, 1.71 mm/s in the upper part and 1.94 mm/s in the lower part. On the cold side, the approximate largest value is -2.13 mm/s.

From the velocity distributions along the characteristic lines which are orthogonal to the xz coordinate surface we observed a symmetrical velocities' distribution along the y -axis direction on the central and upper parts. If we scale up the figure of the velocity distribution along the line which is quite near the bottom of the flow, we found that the natural convection in the lower part of the brick has somewhat 3-dimensional flow characteristics. However, the magnitudes of the velocities' y -components are not largely comparable to the x - and z -components, which means the flow on the y -direction is not very significant. As a conclusion, the 3-dimensional flow characteristics exist but not considerably obvious.

we can also found that the front and back walls impose effects on the flow. The impacts decrease when the y coordinate approaches the center of the enclosure. Approximately, when $0.19 \leq y \leq 0.81$, the impacts of the boundary walls can be neglected.

As for the heat transfer process, we found that the 3-dimensional temperature contour lines are less distorted compared to the 2-dimensional

results, and that the 3-dimensional simulation has a slightly bigger temperature gradient on the z-direction than the 2-dimensional simulation.

Another three simulation cases with different Ra numbers (10^6 , 10^7 , 10^8) are also conducted. The results of the Nusselt number evolution have illustrated clearly the different stages during melting: pure conduction at the initial stage; the competitive stage; and the final convection dominant stage. The results under different Rayleigh number made it clear that the bigger the Ra is, the higher the phase change rate is.

Additionally, at the beginning of the simulations, there occur the oscillations. They are attributed to the intrinsic nature of the combination of the enthalpy method and the LBM. In such simulation, the grids switch their solid-liquid phases sharply, which can introduce an inconsistency of the velocity of the grids encountering the phase change in the vicinity of the solid-liquid interface.

Finally, the performance evaluation shows that the current 3-dimensional simulation on the Nvidia Tesla C2075 GPU has a considerable performance boost (402.2 MLUPS and 67.6 GB/s).

Conclusions and perspectives

In this thesis, the latent heat storage in the form of melting inside a transparent building brick is studied by both experimental and numerical approaches.

From the viewpoint of experimental approach, the role of an experiment plays is to get enough data of the real physical melting process. Those data can afterwards be used to validate the numerical model. However the existing experimental methodologies keep more or less the same. For example, the thermocouples are largely employed to get the temperature information in the melting domain of interest. Those can introduce several imperfections.

1. In general, where there is the density variation caused by temperature change in liquid phase - as this is always the case of melting - natural convection and melting always concur. The scale of this convection is absolutely feeble, it is vulnerable to exterior disturbances, even the latter is quite small. As a consequence, the embedded thermocouples can definitely change the true liquid flow during melting.
2. The thermocouples measure the local temperature. No matter how many thermocouples are installed inside the enclosure, they can just provide us the temperature on those scattered points. A continuous temperature distribution is beyond the reach of thermocouples.

Consequently, in this thesis, a non-intrusive method is employed simultaneously to inspect the melting process, which occurs within one transparent rectangular building brick. The two vertical surfaces of the enclosure are maintained with different but constant temperatures, the upper and front sides are kept available to record the inner process by a camera, and the bottom and back sides are insulated and kept adiabatic.

The experiments are carried out with n-octadecane as PCM and the Ra number has an order of magnitude of 10^8 and Pr is 50. Experimental results

show that:

1. The heat transfer during melting process can be described as three stages. This is because the transition of heat transfer forms. At the very beginning, the pure conduction is the only form, then it is the competitive period of conduction and convection, at the end the convection prevails.
2. During the competitive period of conduction and convection, the relatively high temperature liquid moves upwards. When it reaches the top of the melted cavity, it transfers this amount sensible heat to the solid PCM there. As a result, there is a distinct indentation on the top of solid-liquid interface. However, when this amount of liquid and the newly melted PCM descend, they encounter the ascending convective flow. Therefore, this cause vortices in the vicinity to the lower part of the indentation. The upper part of the melted cavity is characterised by the convection, while the lower part is still by conduction.
3. When the convection finally dominates during melting, the vortex in the upper part disappears. Meanwhile, the contours of the velocity components show the flow might have three dimensional flow pattern.
4. The results also show that heat transfer rate during melting is much higher than that of Neumann solution (pure conduction). The existence of natural convection dramatically influences the melting process.

In addition to the experiments we carried out, a two dimensional numerical simulation is also designed aiming to:

1. provide the mutual validation of the experimental results and the numerical model,
2. provide a general robust and highly efficient solver of the melting process.
3. extend the solver to simulate the melting from a 3-dimensional perspective in order to get more knowledge about the melting. This is based on the previous two aims.

In our numerical model, the thermal lattice Boltzmann method with multiple-relaxation-time (TLBM MRT) is used to calculate the velocity fields and the finite difference to solve the energy equation. As for the melting process, the enthalpy method is employed to provide a uniform equation for the entire calculation domain. The melting solid-liquid interface is approximated on fixed grids.

Furthermore, from the literature review we notice that the published numerical simulations of melting have quite low calculation efficiency, require considerable high computer resources and CPU time.

Therefore, our simulation is specially designed to run on a CUDA enabled GPU in order to boost the simulation potential. In this thesis, two Nvidia GPUs - model Tesla C2050 for the 2-dimensional simulation and Tesla C2075 for the 3-dimensional simulation - are chosen as the calculation platforms and the C language as the programming language. The 2-dimensional simulation results show that:

1. The heat transfer rate from simulation goes well with our experimental results and a slightly higher values than the published analytical results.
2. The transition of the heat transfer forms is similar to our experimental results.
3. Like the experimental results, the same vortex appears in the simulation results. Furthermore, at the beginning stage of melting, another small vortex is also observed. This vortex disappears when convection develops. In addition, in the bottom part of the melted cavity, there are several vortices exist.

The performance tests under different mesh resolutions showed that our two dimensional simulation on GPU have up to 703.31 MLUPS. The device to device memory throughput accounted for up to 52.5% of the hardware's maximum throughput (117.93 GB/s).

After the validation of our numerical simulation model, the solver is extended to simulate 3-dimensional melting. Four cases - characterized by three different Ra numbers - are simulated. The results show that:

1. When $Ra = 2.48 \times 10^8$, along the x-direction and at the same height level inside the brick, the velocities' components possess the same distributions and magnitude. The z-components have the largest magnitudes of the velocities.
2. When $Ra = 2.48 \times 10^8$, the natural convection on the hot side is slightly stronger than on the cold side when there is the solid-liquid interface. Moreover, the natural convection in the middle of the brick is stronger than the bottom part and the upper part. On the hot side, the z-components have an approximate value of 2.20 mm/s in the middle, 1.71 mm/s in the upper part and 1.94 mm/s in the lower part. On the cold side, the approximate largest value is -2.13 mm/s.
3. When $Ra = 2.48 \times 10^8$, as for the flow that is close to the bottom of the brick, the natural convection there has somewhat 3-dimensional flow characteristics. However, the magnitudes of the velocities' y-components are not considerably large, the 3-dimensional flow characteristics exists but not considerably obvious.

4. The front and back walls impose effects on the flow. The impacts decrease when the y coordinate approaches the center of the enclosure. Approximately, when $0.19 \leq y \leq 0.81$, the impacts of the boundary walls can be neglected.
5. When Ra is low - *e.g.* 10^6 and 10^7 -, the convections have quite similar impacts on the heat transfer rate. While when $Ra \geq 10^8$, the convection dramatically increases the heat transfer rate.
6. The 3-dimensional simulation of the melting process has a considerable performance boost, with 402.2 MLUPS and 67.7 GB/s on a Nvidia Tesla C2075 GPU.

Perspectives

About the experiment

The combination of the PIV and the LIF to experimentally study the phase change process introduces a new promising approach to better understand the phase change. Notwithstanding, the high reflection of incident laser light inside the enclosure due to the existence of solid-liquid interface poses many problems. Those thus introduce a relatively high measurement uncertainty. Besides, in this experiment, just n-octadecane is tested while the other types of PCMs are not. If the PCMs are not well transparent, the PIV and the LIF methods would not be applicable. In the future, it is very important to find better tracer particles and fluorescent dyes. At the same time, different types of PCMs should also be considered.

About the numerical simulation

When designing the simulation model, the calculation domain is based on the transparent wall brick. However, in real experiment process, the upper part of the brick was left empty to accommodate the volume expansion of the PCM. In the simulation, this small vacant space is neglected and assumed filled with the PCM. As a result, a more sophisticated model need to be built in the future to embody this small space (with a free surface).

As for the computation efficiency, a performance decrease is noticeable in three dimensional simulation, by contrast with the two dimensional simulation. This is mostly due to the more logic judgements in the code, because the CUDA programming pattern can't achieve ideal high performance if there are many code divergences. Consequently, in the future, a more sophisticated approach should be devised in order to do this logic judgements in the code. Meanwhile, the solver should also be modified to adapt to different or even more complex enclosures, such as cylindrical

enclosure or enclosures with fins *etc.* At last, simulations of different types of PCMs should also be carried out.

Bibliography

- [1] M. S. Dresselhaus and I. L. Thomas, "Alternative energy technologies," *Nature*, vol. 414, no. 6861, pp. 332–337, 2001.
- [2] BP, "Bp statistical review of world energy," tech. rep., 2013.
- [3] F. M. of Ecology and S. Development, "Plan climat de la france," tech. rep., French Ministry of Ecology and Sustainable Development, 2004.
- [4] I. Dincer and M. A. Rosen, *Energy Storage Systems*, pp. 51–82. John Wiley & Sons, Ltd, 2010.
- [5] J. A. Simmons, "Reversible oxidation of metal oxides for thermal energy storage," in *Sharing the Sun: Solar Technology in the Seventies, Volume 8*, vol. 8, pp. 219–225, 1976.
- [6] H. Fröhlich, "Long-range coherence and energy storage in biological systems," *International Journal of Quantum Chemistry*, vol. 2, no. 5, pp. 641–649, 1968.
- [7] W. Buckles and W. Hassenzahl, "Superconducting magnetic energy storage," *Power Engineering Review, IEEE*, vol. 20, no. 5, pp. 16–20, 2000.
- [8] A. M. Khudhair and M. M. Farid, "A review on energy conservation in building applications with thermal storage by latent heat using phase change materials," *Energy Conversion and Management*, vol. 45, no. 2, pp. 263 – 275, 2004.
- [9] A. Abhat, "Low temperature latent heat thermal energy storage: Heat storage materials," *Solar Energy*, vol. 30, no. 4, pp. 313 – 332, 1983.
- [10] A. Sharma, V. Tyagi, C. Chen, and D. Buddhi, "Review on thermal energy storage with phase change materials and applications," *Renewable and Sustainable Energy Reviews*, vol. 13, no. 2, pp. 318 – 345, 2009.
- [11] A. Sari and A. Karaipekli, "Preparation, thermal properties and thermal reliability of palmitic acid/expanded graphite composite as form-stable {PCM} for thermal energy storage," *Solar Energy Materials and Solar Cells*, vol. 93, no. 5, pp. 571 – 576, 2009.
- [12] H. Asan and Y. Sancaktar, "Effects of wall's thermophysical properties on time lag and decrement factor," *Energy and Buildings*, vol. 28, no. 2, pp. 159 – 166, 1998.

- [13] Y. Zhang, K. Lin, Q. Zhang, and H. Di, "Ideal thermophysical properties for free-cooling (or heating) buildings with constant thermal physical property material," *Energy and Buildings*, vol. 38, no. 10, pp. 1164 – 1170, 2006.
- [14] F. Kuznik, D. David, K. Johannes, and J.-J. Roux, "A review on phase change materials integrated in building walls," *Renewable and Sustainable Energy Reviews*, vol. 15, no. 1, pp. 379 – 391, 2011.
- [15] D. Feldman, D. Banu, D. Hawes, and E. Ghanbari, "Obtaining an energy storing building material by direct incorporation of an organic phase change material in gypsum wallboard," *Solar Energy Materials*, vol. 22, no. 2–3, pp. 231 – 242, 1991.
- [16] M. Xiao, B. Feng, and K. Gong, "Preparation and performance of shape stabilized phase change thermal storage materials with high thermal conductivity," *Energy Conversion and Management*, vol. 43, no. 1, pp. 103 – 108, 2002.
- [17] H. Kaasinen, "The absorption of phase change substances into commonly used building materials," *Solar Energy Materials and Solar Cells*, vol. 27, no. 2, pp. 173 – 179, 1992. <ce:title>Special Issue on Heat Storage Materials</ce:title>
- [18] L. F. Cabeza, C. Castellón, M. Nogués, M. Medrano, R. Leppers, and O. Zubillaga, "Use of microencapsulated {PCM} in concrete walls for energy savings," *Energy and Buildings*, vol. 39, no. 2, pp. 113 – 119, 2007.
- [19] P. Schossig, H.-M. Henning, S. Gschwander, and T. Haussmann, "Micro-encapsulated phase-change materials integrated into construction materials," *Solar Energy Materials and Solar Cells*, vol. 89, no. 2–3, pp. 297 – 306, 2005. <ce:title>EuroSun2004</ce:title> <xocs:full-name>EuroSun2004</xocs:full-name>.
- [20] Y. Yamagishi, T. Sugeno, T. Ishige, H. Takeuchi, and A. Pyatenko, "An evaluation of microencapsulated pcm for use in cold energy transportation medium," in *Energy Conversion Engineering Conference, 1996. IECEC 96., Proceedings of the 31st Intersociety*, vol. 3, pp. 2077–2083 vol.3, 1996.
- [21] X. xiang Zhang, Y. feng Fan, X. ming Tao, and K. lun Yick, "Crystallization and prevention of supercooling of microencapsulated n-alkanes," *Journal of Colloid and Interface Science*, vol. 281, no. 2, pp. 299 – 306, 2005.
- [22] H. Inaba and P. Tu, "Evaluation of thermophysical characteristics on shape-stabilized paraffin as a solid-liquid phase change material," *Heat and Mass Transfer*, vol. 32, no. 4, pp. 307–312, 1997.
- [23] M. Xiao, B. Feng, and K. Gong, "Thermal performance of a high conductive shape-stabilized thermal storage material," *Solar Energy Materials and Solar Cells*, vol. 69, no. 3, pp. 293 – 296, 2001.
- [24] A. Sari, "Form-stable paraffin/high density polyethylene composites as solid-liquid phase change material for thermal energy storage: preparation and thermal properties," *Energy Conversion and Management*, vol. 45, no. 13–14, pp. 2033 – 2042, 2004.
- [25] G. Zhou, Y. Zhang, X. Wang, K. Lin, and W. Xiao, "An assessment of mixed type pcm-gypsum and shape-stabilized {PCM} plates in a building for passive solar heating," *Solar Energy*, vol. 81, no. 11, pp. 1351 – 1360, 2007.

- [26] Y. Zhang, J. Ding, X. Wang, R. Yang, and K. Lin, "Influence of additives on thermal conductivity of shape-stabilized phase change material," *Solar Energy Materials and Solar Cells*, vol. 90, no. 11, pp. 1692 – 1702, 2006.
- [27] M. Ahmad, A. Bontemps, H. Sallée, and D. Quenard, "Experimental investigation and computer simulation of thermal behaviour of wallboards containing a phase change material," *Energy and Buildings*, vol. 38, no. 4, pp. 357 – 366, 2006.
- [28] A. Pasupathy, L. Athanasius, R. Velraj, and R. Seeniraj, "Experimental investigation and numerical simulation analysis on the thermal performance of a building roof incorporating phase change material (pcm) for thermal management," *Applied Thermal Engineering*, vol. 28, no. 5–6, pp. 556 – 565, 2008.
- [29] A. Carbonari, M. D. Grassi, C. D. Perna, and P. Principi, "Numerical and experimental analyses of {PCM} containing sandwich panels for prefabricated walls," *Energy and Buildings*, vol. 38, no. 5, pp. 472 – 483, 2006.
- [30] K. Darkwa and J.-S. Kim, "Dynamics of energy storage in phase change dry-wall systems," *International Journal of Energy Research*, vol. 29, no. 4, pp. 335–343, 2005.
- [31] H. Weinlader, A. Beck, and J. Fricke, "Pcm-facade-panel for daylighting and room heating," *Solar Energy*, vol. 78, no. 2, pp. 177 – 186, 2005. <ce:title>ISES Solar World Congress 2003</ce:title>.
- [32] C. Voelker, O. Kornadt, and M. Ostry, "Temperature reduction due to the application of phase change materials," *Energy and Buildings*, vol. 40, no. 5, pp. 937 – 944, 2008.
- [33] M. Amir, M. Lacroix, and N. Galanis, "Comportement thermique de dalles chauffantes électriques pour le stockage quotidien," *International Journal of Thermal Sciences*, vol. 38, no. 2, pp. 121 – 131, 1999.
- [34] M. M. Farid and X. D. Chen, "Domestic electrical space heating with heat storage," *Proceedings of the Institution of Mechanical Engineers, Part A: Journal of Power and Energy*, vol. 213, no. 2, pp. 83–92, 1999.
- [35] K. Lin, Y. Zhang, X. Xu, H. Di, R. Yang, and P. Qin, "Experimental study of under-floor electric heating system with shape-stabilized {PCM} plates," *Energy and Buildings*, vol. 37, no. 3, pp. 215 – 220, 2005.
- [36] M. Koschenz and B. Lehmann, "Development of a thermally activated ceiling panel with {PCM} for application in lightweight and retrofitted buildings," *Energy and Buildings*, vol. 36, no. 6, pp. 567 – 578, 2004.
- [37] M. Jaworski, P. Łapka, and P. Furmański, "Numerical modelling and experimental studies of thermal behaviour of building integrated thermal energy storage unit in a form of a ceiling panel," *Applied Energy*, vol. 113, no. 0, pp. 548 – 557, 2014.
- [38] A. Ghoneim, S. Klein, and J. Duffie, "Analysis of collector-storage building walls using phase-change materials," *Solar Energy*, vol. 47, no. 3, pp. 237 – 242, 1991.
- [39] A. de Gracia, L. Navarro, A. Castell, Álvaro Ruiz-Pardo, S. Álvarez, and L. F. Cabeza, "Experimental study of a ventilated facade with {PCM} during winter period," *Energy and Buildings*, vol. 58, no. 0, pp. 324 – 332, 2013.

- [40] S. Chandra, R. Kumar, S. Kaushik, and S. Kaul, "Thermal performance of a non-air-conditioned building with {PCCM} thermal storage wall," *Energy Conversion and Management*, vol. 25, no. 1, pp. 15 – 20, 1985.
- [41] K. Peippo, P. Kauranen, and P. Lund, "A multicomponent {PCM} wall optimized for passive solar heating," *Energy and Buildings*, vol. 17, no. 4, pp. 259 – 270, 1991.
- [42] A. Athienitis, C. Liu, D. Hawes, D. Banu, and D. Feldman, "Investigation of the thermal performance of a passive solar test-room with wall latent heat storage," *Building and Environment*, vol. 32, no. 5, pp. 405 – 410, 1997.
- [43] A. Oliver, "Thermal characterization of gypsum boards with {PCM} included: Thermal energy storage in buildings through latent heat," *Energy and Buildings*, vol. 48, no. 0, pp. 1 – 7, 2012.
- [44] F. Goia, M. Perino, and V. Serra, "Improving thermal comfort conditions by means of {PCM} glazing systems," *Energy and Buildings*, vol. 60, no. 0, pp. 442 – 452, 2013.
- [45] A. Esam M, "Using phase change materials in window shutter to reduce the solar heat gain," *Energy and Buildings*, vol. 47, no. 0, pp. 421–429, 2012.
- [46] H.-M. Chou, C.-R. Chen, and V.-L. Nguyen, "A new design of metal-sheet cool roof using {PCM}," *Energy and Buildings*, vol. 57, no. 0, pp. 42 – 50, 2013.
- [47] J. Kosny, K. Biswas, W. Miller, and S. Kriner, "Field thermal performance of naturally ventilated solar roof with {PCM} heat sink," *Solar Energy*, vol. 86, no. 9, pp. 2504 – 2514, 2012.
- [48] L. Cabeza, H. Mehling, S. Hiebler, and F. Ziegler, "Heat transfer enhancement in water when used as {PCM} in thermal energy storage," *Applied Thermal Engineering*, vol. 22, no. 10, pp. 1141 – 1151, 2002.
- [49] R. Velraj, R. Seeniraj, B. Hafner, C. Faber, and K. Schwarzer, "{HEAT} {TRANSFER} {ENHANCEMENT} {IN} a {LATENT} {HEAT} {STORAGE} {SYSTEM}," *Solar Energy*, vol. 65, no. 3, pp. 171 – 180, 1999.
- [50] A. Elgafy and K. Lafdi, "Effect of carbon nanofiber additives on thermal behavior of phase change materials," *Carbon*, vol. 43, no. 15, pp. 3067 – 3074, 2005.
- [51] M. Okada, "Analysis of heat transfer during melting from a vertical wall," *International Journal of Heat and Mass Transfer*, vol. 27, no. 11, pp. 2057 – 2066, 1984.
- [52] C. Bénard, D. Gobin, and F. Martinez, "Melting in rectangular enclosures: Experiments and numerical simulations," *Journal of Heat Transfer*, vol. 107, no. 4, pp. 794–803, 1985.
- [53] C.-J. Ho and R. Viskanta, "Inward solid-liquid phase-change heat transfer in a rectangular cavity with conducting vertical walls," *International Journal of Heat and Mass Transfer*, vol. 27, no. 7, pp. 1055 – 1065, 1984.
- [54] P. Jany and A. Bejan, "Scaling theory of melting with natural convection in an enclosure," *International Journal of Heat and Mass Transfer*, vol. 31, no. 6, pp. 1221–1235, 1988.

- [55] C. Bénard, D. Gobin, and A. Zanolì, "Moving boundary problem: heat conduction in the solid phase of a phase-change material during melting driven by natural convection in the liquid," *International Journal of Heat and Mass Transfer*, vol. 29, no. 11, pp. 1669 – 1681, 1986.
- [56] F. Agyenim, P. Eames, and M. Smyth, "Experimental study on the melting and solidification behaviour of a medium temperature phase change storage material (erythritol) system augmented with fins to power a libh2o absorption cooling system," *Renewable Energy*, vol. 36, no. 1, pp. 108–117, 2011. ISI Document Delivery No.: 662WM Times Cited: 0 Cited Reference Count: 28 Agyenim, Francis Eames, Philip Smyth, Mervyn Pergamon-elsevier science ltd Oxford.
- [57] H. Shmueli, G. Ziskind, and R. Letan, "Melting in a vertical cylindrical tube: Numerical investigation and comparison with experiments," *International Journal of Heat and Mass Transfer*, vol. 53, no. 19-20, pp. 4082–4091, 2010. Times Cited: 0.
- [58] S. Kalaiselvam, M. Veerappan, A. Arul Aaron, and S. Iniyan, "Experimental and analytical investigation of solidification and melting characteristics of pcms inside cylindrical encapsulation," *International Journal of Thermal Sciences*, vol. 47, no. 7, pp. 858–874, 2008.
- [59] U. Stritih, "An experimental study of enhanced heat transfer in rectangular {PCM} thermal storage," *International Journal of Heat and Mass Transfer*, vol. 47, no. 12–13, pp. 2841 – 2847, 2004.
- [60] V. Alexiades and A. D. Solomon, *Mathematical modeling of melting and freezing processes*. Taylor & Francis, 1993.
- [61] N. Hannoun, V. Alexiades, and T. Z. Mai, "Resolving the controversy over tin and gallium melting in a rectangular cavity heated from the side," *Numerical Heat Transfer, Part B: Fundamentals*, vol. 44, no. 3, pp. 253–276, 2003.
- [62] R. Nochetto, M. Paolini, and C. Verdi, "An adaptive finite element method for two-phase stefan problems in two space dimensions. ii: Implementation and numerical experiments," *SIAM Journal on Scientific and Statistical Computing*, vol. 12, no. 5, pp. 1207–1244, 1991. ISSN (print): 0196-5204 ISSN (online): 2168-3417 Printed version in Bibliothèque Lyon 1.
- [63] N. Provatas, N. Goldenfeld, and J. Dantzig, "Efficient computation of dendritic microstructures using adaptive mesh refinement," *Phys. Rev. Lett.*, vol. 80, pp. 3308–3311, Apr 1998.
- [64] N. Provatas, N. Goldenfeld, and J. Dantzig, "Adaptive mesh refinement computation of solidification microstructures using dynamic data structures," *Journal of Computational Physics*, vol. 148, no. 1, pp. 265 – 290, 1999.
- [65] M. Ainsworth and J. Oden, "A posteriori error estimation in finite element analysis," *Computer Methods in Applied Mechanics and Engineering*, vol. 142, no. 1–2, pp. 1 – 88, 1997.
- [66] J. Mackenzie and M. Robertson, "The numerical solution of one-dimensional phase change problems using an adaptive moving mesh method," *Journal of Computational Physics*, vol. 161, no. 2, pp. 537 – 557, 2000.

- [67] J. Mackenzie and M. Robertson, "A moving mesh method for the solution of the one-dimensional phase-field equations," *Journal of Computational Physics*, vol. 181, no. 2, pp. 526 – 544, 2002.
- [68] Z. Tan, K. Lim, and B. Khoo, "An adaptive mesh redistribution method for the incompressible mixture flows using phase-field model," *Journal of Computational Physics*, vol. 225, no. 1, pp. 1137 – 1158, 2007.
- [69] O. Bertrand, B. Binet, H. Combeau, S. Couturier, Y. Delannoy, D. Gobin, M. Lacroix, P. L. Quéré, M. Médale, J. Mencinger, H. Sadat, and G. Vieira, "Melting driven by natural convection a comparison exercise: first results," *International Journal of Thermal Sciences*, vol. 38, no. 1, pp. 5 – 26, 1999.
- [70] V. R. Voller, M. Cross, and N. C. Markatos, "An enthalpy method for convection/diffusion phase change," *International Journal for Numerical Methods in Engineering*, vol. 24, no. 1, pp. 271–284, 1987.
- [71] A. D. Brent, V. R. Voller, and K. J. Reid, "Enthalpy-porosity technique for modeling convection-diffusion phase change: Application to the melting of a pure metal," *Numerical Heat Transfer*, vol. 13, no. 3, pp. 297 – 318, 1988.
- [72] M. Costa, A. Oliva, C. D. F. Segarra, and R. Alba, "Numerical simulation of solid-liquid phase change phenomena," *Computer Methods in Applied Mechanics and Engineering*, vol. 91, no. 1-3, pp. 1123–1134, 1991.
- [73] M. Costa, A. Oliva, C. D. P. Segarra, and R. Alba, "Numerical-simulation of solid liquid-phase change phenomena," *Computer Methods in Applied Mechanics and Engineering*, vol. 91, no. 1-3, pp. 1123–1134, 1991. Times Cited: 11
2nd world congress on computational mechanics Aug 27-31, 1990 Stuttgart, germany Inst comp applicat.
- [74] V. Voller and M. Cross, "Accurate solutions of moving boundary problems using the enthalpy method," *International Journal of Heat and Mass Transfer*, vol. 24, no. 3, pp. 545 – 556, 1981.
- [75] V. Voller and C. Prakash, "A fixed grid numerical modelling methodology for convection-diffusion mushy region phase-change problems," *International Journal of Heat and Mass Transfer*, vol. 30, no. 8, pp. 1709 – 1719, 1987.
- [76] V. R. Voller, "Fast implicit finite-difference method for the analysis of phase change problems," *Numerical Heat Transfer, Part B: Fundamentals*, vol. 17, no. 2, pp. 155–169, 1990.
- [77] M. Costa, D. Buddhi, and A. Oliva, "Numerical simulation of a latent heat thermal energy storage system with enhanced heat conduction," *Energy Conversion and Management*, vol. 39, no. 3–4, pp. 319 – 330, 1998.
- [78] P. Lamberg, R. Lehtiniemi, and A.-M. Henell, "Numerical and experimental investigation of melting and freezing processes in phase change material storage," *International Journal of Thermal Sciences*, vol. 43, no. 3, pp. 277 – 287, 2004.
- [79] M. S. Bendell and B. Gebhart, "Heat transfer and ice-melting in ambient water near its density extremum," *International Journal of Heat and Mass Transfer*, vol. 19, no. 10, pp. 1081 – 1087, 1976.
- [80] F. Corvaro and M. Paroncini, "A numerical and experimental analysis on the natural convective heat transfer of a small heating strip located on the

- floor of a square cavity," *Applied Thermal Engineering*, vol. 28, no. 1, pp. 25 – 35, 2008.
- [81] H. Ge, H. Li, S. Mei, and J. Liu, "Low melting point liquid metal as a new class of phase change material: An emerging frontier in energy area," *Renewable and Sustainable Energy Reviews*, vol. 21, no. 0, pp. 331 – 346, 2013.
- [82] L.-W. Fan, Y.-Q. Xiao, Y. Zeng, X. Fang, X. Wang, X. Xu, Z.-T. Yu, R.-H. Hong, Y.-C. Hu, and K.-F. Cen, "Effects of melting temperature and the presence of internal fins on the performance of a phase change material (pcm)-based heat sink," *International Journal of Thermal Sciences*, vol. 70, no. 0, pp. 114 – 126, 2013.
- [83] R. Viswanath and Y. Jaluria, "A comparison of different solution methodologies for melting and solidification problems in enclosures," *Numerical Heat Transfer, Part B: Fundamentals*, vol. 24, no. 1, pp. 77–105, 1993.
- [84] J. Mencinger, "Numerical simulation of melting in two-dimensional cavity using adaptive grid," *Journal of Computational Physics*, vol. 198, no. 1, pp. 243 – 264, 2004.
- [85] M. S. Gandhi, M. J. Sathe, J. B. Joshi, and P. K. Vijayan, "Two phase natural convection: Cfd simulations and piv measurement," *Chemical Engineering Science*, vol. 66, no. 14, pp. 3152–3171, 2011.
- [86] S. Someya, Y. Li, K. Ishii, and K. Okamoto, "Combined two-dimensional velocity and temperature measurements of natural convection using a high-speed camera and temperature-sensitive particles," *Experiments in Fluids*, vol. 50, no. 1, pp. 65–73, 2011. Times Cited: 0.
- [87] M. T. Stickland, T. J. Scanlon, and J. MacKenzie, "An experimental investigation of natural convection with solidification in a differentially heated cavity," *International Journal of Heat and Mass Transfer*, vol. 50, no. 1-2, pp. 36–44, 2007.
- [88] C. D. Seybert and J. W. Evans, "Piv measurements of velocity of water in the presence of ice and comparison with calculated values," *International Journal of Heat and Mass Transfer*, vol. 48, no. 1, pp. 67–73, 2005. ISI Document Delivery No.: 878RM Times Cited: 4 Cited Reference Count: 15 Pergamon-elsevier science ltd Oxford.
- [89] M. C. J. Coolen, R. N. Kieft, C. C. M. Rindt, and A. A. van Steenhoven, "Application of 2-d lif temperature measurements in water using a nd : Yag laser," *Experiments in Fluids*, vol. 27, no. 5, pp. 420–426, 1999.
- [90] U. Stopper, M. Aigner, H. Ax, W. Meier, R. Sadanandan, M. StÄhr, and A. Bonaldo, "Piv, 2d-lif and 1d-raman measurements of flow field, composition and temperature in premixed gas turbine flames," *Experimental Thermal and Fluid Science*, vol. 34, no. 3, pp. 396–403, 2010.
- [91] M. Raffel, C. Willert, S. Wereley, and J. Kompenhans, "Introduction," in *Particle Image Velocimetry*, Experimental Fluid Mechanics, pp. 1–13, Springer Berlin Heidelberg, 2007.
- [92] M. Raffel, C. Willert, S. Wereley, and J. Kompenhans, "Physical and technical background," in *Particle Image Velocimetry*, Experimental Fluid Mechanics, pp. 15–77, Springer Berlin Heidelberg, 2007.

- [93] M. Raffel, C. Willert, S. Wereley, and J. Kompenhans, "Piv recording techniques," in *Particle Image Velocimetry*, Experimental Fluid Mechanics, pp. 97–121, Springer Berlin Heidelberg, 2007.
- [94] A. Leipertz, A. Braeuer, J. Kiefer, A. Dreizler, and C. Heeger, *Laser-Induced Fluorescence*. Wiley-VCH Verlag GmbH & Co. KGaA, 2010.
- [95] J. Sakakibara and R. J. Adrian, "Whole field measurement of temperature in water using two-color laser induced fluorescence," *Experiments in Fluids*, vol. 26, no. 1-2, pp. 7–15, 1999.
- [96] J. Sakakibara and R. Adrian, "Measurement of temperature field of a rayleigh-bénard convection using two-color laser-induced fluorescence," *Experiments in Fluids*, vol. 37, no. 3, pp. 331–340, 2004.
- [97] J. Crimaldi, "Planar laser induced fluorescence in aqueous flows," *Experiments in Fluids*, vol. 44, no. 6, pp. 851–863, 2008.
- [98] J. P. Crimaldi and J. R. Koseff, "High-resolution measurements of the spatial and temporal scalar structure of a turbulent plume," *Experiments in Fluids*, vol. 31, no. 1, pp. 90–102, 2001.
- [99] F. P. Incropera, A. S. Lavine, and D. P. DeWitt, *Fundamentals of heat and mass transfer*. John Wiley & Sons Incorporated, 2011.
- [100] S. Hasnain, "Review on sustainable thermal energy storage technologies, part i: heat storage materials and techniques," *Energy Conversion and Management*, vol. 39, no. 11, pp. 1127 – 1138, 1998.
- [101] M. Gumus, "Reducing cold-start emission from internal combustion engines by means of thermal energy storage system," *Applied Thermal Engineering*, vol. 29, no. 4, pp. 652 – 660, 2009.
- [102] *Applications and benefits of catalytic converter thermal management*, 1996.
- [103] A. Ghoneim, "Comparison of theoretical models of phase-change and sensible heat storage for air and water-based solar heating systems," *Solar energy*, vol. 42, no. 3, pp. 209–220, 1989.
- [104] P. Lallemand and L.-S. Luo, "Theory of the lattice boltzmann method: Dispersion, dissipation, isotropy, galilean invariance, and stability," *Phys. Rev. E*, vol. 61, pp. 6546–6562, Jun 2000.
- [105] D. Chatterjee and S. Chakraborty, "An enthalpy-based lattice boltzmann model for diffusion dominated solid–liquid phase transformation," *Physics Letters A*, vol. 341, no. 1–4, pp. 320 – 330, 2005.
- [106] E. Semma, M. El Ganaoui, R. Bennacer, and A. A. Mohamad, "Investigation of flows in solidification by using the lattice boltzmann method," *International Journal of Thermal Sciences*, vol. 47, no. 3, pp. 201–208, 2008. Times Cited: 13.
- [107] W. Miller, "The lattice boltzmann method: a new tool for numerical simulation of the interaction of growth kinetics and melt flow," *Journal of Crystal Growth*, vol. 230, no. 1–2, pp. 263 – 269, 2001. <ce:title>Proceedings of the Third International Workshop om Modeling in Cr ystal Growth</ce:title>.
- [108] W. Miller, I. Rasin, and S. Succi, "Lattice boltzmann phase-field modelling of binary-alloy solidification," *Physica A: Statistical Mechanics and its Applications*, vol. 362, no. 1, pp. 78 – 83, 2006. <ce:title>Discrete Simulation

- of Fluid Dynamics</ce:title> <ce:subtitle>Proceedings of the 13th International Conference on Discrete Simulation of Fluid Dynamics</ce:subtitle>
<xocs:full-name>13th International Conference on Discrete Simulation of Fluid Dynamics</xocs:full-name>.
- [109] H. Safari, M. H. Rahimian, and M. Krafczyk, "Extended lattice boltzmann method for numerical simulation of thermal phase change in two-phase fluid flow," *Phys. Rev. E*, vol. 88, p. 013304, Jul 2013.
- [110] Z. Fan, F. Qiu, A. Kaufman, and S. Yoakum-Stover, "Gpu cluster for high performance computing," in *Proceedings of the 2004 ACM/IEEE Conference on Supercomputing*, SC '04, (Washington, DC, USA), pp. 47–, IEEE Computer Society, 2004.
- [111] F. Kuznik, C. Obrecht, G. Rusaouen, and J.-J. Roux, "Lbm based flow simulation using gpu computing processor," *Computers & Mathematics with Applications*, vol. 59, no. 7, pp. 2380 – 2392, 2010. <ce:title>Mesoscopic Methods in Engineering and Science</ce:title> <xocs:full-name>International Conferences on Mesoscopic Methods in Engineering and Science</xocs:full-name>.
- [112] C. Obrecht, F. Kuznik, B. Tourancheau, and J.-J. Roux, "Scalable lattice boltzmann solvers for {CUDA} {GPU} clusters," *Parallel Computing*, vol. 39, no. 6–7, pp. 259 – 270, 2013.
- [113] A. Banari, C. Janßen, S. T. Grilli, and M. Krafczyk, "Efficient {GPGPU} implementation of a lattice boltzmann model for multiphase flows with high density ratios," *Computers & Fluids*, vol. 93, no. 0, pp. 1 – 17, 2014.
- [114] C. Cuda, "Programming guide," *NVIDIA Corporation*, July, 2013.
- [115] X. He and L.-S. Luo, "A priori derivation of the lattice boltzmann equation," *Phys. Rev. E*, vol. 55, pp. R6333–R6336, Jun 1997.
- [116] X. Y. He and L. S. Luo, "Theory of the lattice boltzmann method: From the boltzmann equation to the lattice boltzmann equation," *Physical Review E*, vol. 56, no. 6, pp. 6811–6817, 1997. Times Cited: 430.
- [117] J. Hardy, Y. Pomeau, and O. de Pazzis, "Time evolution of a two-dimensional classical lattice system," *Phys. Rev. Lett.*, vol. 31, pp. 276–279, Jul 1973.
- [118] J. Hardy, Y. Pomeau, and O. de Pazzis, "Time evolution of a two-dimensional model system. i. invariant states and time correlation functions," *Journal of Mathematical Physics*, vol. 14, no. 12, pp. 1746–1759, 1973.
- [119] U. Frisch, B. Hasslacher, and Y. Pomeau, "Lattice-gas automata for the navier-stokes equation," *Physical Review Letters*, vol. 56, pp. 1505–1508, Apr. 1986.
- [120] S. Wolfram, "Cellular automaton fluids 1: Basic theory," *Journal of Statistical Physics*, vol. 45, no. 3-4, pp. 471–526, 1986.
- [121] Y. Chen, H. Ohashi, and M. Akiyama, "Prandtl number of lattice bhatnagar–gross–krook fluid," *Physics of Fluids (1994–present)*, vol. 7, no. 9, pp. 2280–2282, 1995.
- [122] D. d’Humières, "Multiple–relaxation–time lattice boltzmann models in three dimensions," *Philosophical Transactions of the Royal Society of London*.

- Series A:Mathematical, Physical and Engineering Sciences*, vol. 360, no. 1792, pp. 437–451, 2002.
- [123] P. Lallemand and L.-S. Luo, “Theory of the lattice boltzmann method: Acoustic and thermal properties in two and three dimensions,” *Phys. Rev. E*, vol. 68, p. 036706, Sep 2003.
- [124] B. Crouse, M. Krafczyk, S. Kühner, E. Rank, and C. van Treeck, “Indoor air flow analysis based on lattice boltzmann methods,” *Energy and Buildings*, vol. 34, no. 9, pp. 941 – 949, 2002. A View of Energy and Bilding Performance Simulation at the start of the third millennium.
- [125] J. Tolke and M. Krafczyk, “Teraflop computing on a desktop pc with gpus for 3d cfd,” *International Journal of Computational Fluid Dynamics*, vol. 22, pp. 443–456, Aug. 2008.
- [126] C. Obrecht, F. Kuznik, B. Tourancheau, and J.-J. Roux, “The thelma project: A thermal lattice boltzmann solver for the gpu,” *Computers & Fluids*, vol. 54, no. 0, pp. 118–126, 2012.
- [127] M. Mbaye and E. Bilgen, “Phase change process by natural convection–diffusion in rectangular enclosures,” *Heat and Mass Transfer*, vol. 37, no. 1, pp. 35–42, 2001.
- [128] J. S. Lim and A. Bejan, “The prandtl number effect on melting dominated by natural convection,” *Journal of Heat Transfer*, vol. 114, pp. 784–787, Aug. 1992.
- [129] C. Cuda, “Programming guide,” *NVIDIA Corporation*, July, 2012.
- [130] J. Miranda Fuentes, *Développement d’un modèle de Boltzmann sur gaz réseau pour l’étude du changement de phase en présence de convection naturelle et de rayonnement*. PhD thesis, INSA de Lyon, 2013.
- [131] W. Gong, K. Frédéric, and K. Johannes, “Numerical simulation of melting with natural convection based on mrt-lbm and performed with cuda enabled gpu,” *Communications in Computational Physics*, vol. Submitted, p. Submitted, 2013.

Appendices

Appendix **A**

Article submitted to
*Communications in Computational
Physics*

FOLIO ADMINISTRATIF

THESE SOUTENUE DEVANT L'INSTITUT NATIONAL DES SCIENCES APPLIQUEES DE LYON

NOM : GONG

DATE de SOUTENANCE : le 25 Juin 2014

(avec précision du nom de jeune fille, le cas échéant)

Prénoms : Wei

TITRE : Heat storage of PCM inside a transparent building brick: experimental study and LBM simulation on GPU

NATURE : Doctorat

Numéro d'ordre : AAAAISALXXXX

Ecole doctorale : Mécanique, Energétique, Génie civil, Acoustique

Spécialité : Energétique

RESUME :

A présent, les bâtiments résidentiels et commerciaux sont en phase de devenir le secteur le plus consommateur d'énergie dans de nombreux pays, comme par exemple en France. Diverses recherches ont été menées de manière à réduire la consommation énergétiques des bâtiments et augmenter leur confort thermique. Parmi tous les différentes approches, la technologie du stockage de chaleur latent se distingue par une très bonne capacité à stocker la chaleur afin de réduire les écarts entre la disponibilité et la demande d'énergie. Dans le cadre de l'un de nos projets, nous avons l'intention d'intégrer au design des murs des bâtiments un type de brique transparente remplie de matériaux à changement de phase (MCP). Les MCP à l'intérieur de la brique sont soumis à des changements de phase liquide-solide. Cette thèse s'attaque à la problématique du processus de fusion au sein de la brique. Au cours de cette thèse, une méthode expérimentale non-intrusive a été développée afin d'améliorer les techniques expérimentales existantes. La vélocimétrie des images des particules (VIP) et la fluorescence induite par laser (FIL) ont été couplées pour étudier la convection naturelle et la distribution de la température. Puisqu'aucun thermocouple n'a été inséré au sein de la brique, le processus de la fusion a été considéré sans perturbation. Les résultats montrent que cette conception expérimentale a un avenir prometteur, même si elle reste à améliorer. Par la suite, nous présentons deux simulations numériques. Ces simulations se fondent sur la méthode de Boltzmann sur réseau à temps de relaxation multiple (LBM MRT), employée pour résoudre le champ de vitesse, et sur la méthode de différences finies, pour obtenir la distribution de la température. La méthode d'enthalpie a quant à elle été utilisée pour simuler le changement de phase. Les simulations en deux dimensions et trois dimensions ont toutes deux été réalisées avec succès. Point important, ces simulations numériques ont été développées en langage C pour tourner spécifiquement sur un processeur graphique (GPU), afin d'augmenter l'efficacité de la simulation en profitant de la capacité de calcul d'un GPU. Les résultats des simulations concordent bien avec les résultats de nos expériences et avec les résultats analytiques publiés.

MOTS-CLES :

changement de phase, fusion, convection naturelle, détermination de l'interface des phases, méthode enthalpique, matériaux à changement de phase (MCP), stockage de chaleur latent, méthode Boltzmann sur réseau, calculs avec haute performance, processeur graphique (GPU), économie d'énergie dans les bâtiments.

Laboratoire (s) de recherche :

Le Centre d'Energétique et de Thermique de Lyon (CETHIL)

Directeur de thèse:

Kévy Johannes ; Frédéric Kuznik

Président de jury :

Composition du jury :

Gilles FRAISSE, Professeur des universités, Université de Savoie (Rapporteur)

Hassane NAJI, Professeur des universités, Université d'Artois (Rapporteur)

Kévy JOHANNES, Maître de Conférences, Université Lyon 1 (UCBL)

Frédéric KUZNIK, Maître de Conférences, HDR, INSA de Lyon

Joseph VIRGONE, Professeur des universités, INSA de Lyon

Pascal Henry BIWOLE, Maître de Conférences, Université de Nice